Colloidal Analysis of Particles Extracted from Microalloyed Steels

Dissertation
zur Erlangung des Grades
des Doktors der Ingenieurwissenschaften
der Naturwissenschaftlich-Technischen
Fakultät
der Universität des Saarlandes

Andreas Hegetschweiler
INM – Leibniz-Institut für Neue Materialien gGmbH
Universität des Saarlandes

Saarbrücken, August 2018

Tag des Kolloquiums: 26. November 2018

Dekan: Prof. Dr. Guido Kickelbick

Berichterstatter: Prof. Dr. Tobias Kraus

Prof. Dr. Christian Motz

Vorsitz: Prof. Dr. Gerhard Wenz

Akad. Mitarbeiter: Dr. Frank Aubertin

Acknowledgement

First and foremost, I would like to thank Prof. Tobias Kraus for giving me the opportunity to work in his group and write this thesis. He was an extraordinary mentor, who supervised and guided me during this study and always had time for short questions. I am very thankful for his patience during numerous abstract iterations, the fruitful discussions, and the faith in me and my research.

I also would like to thank Prof. Christian Motz for become my scientific advisor and second referee.

I am grateful to the responsible persons of the AG der Dillinger Hüttenwerke for founding this thesis and the employees that contributed to the success of this project. I would like to thank Volker Schwinn, Head of Development and Design, for the confidence he has placed in me to work on this topic and in particular Dr. Thorsten Staudt for his constructive cooperation and support during the thesis.

Without the support of my prestigious colleagues of the structure formation group, I would never have been able to finish this work:

Dr. Ioannis Kanelidis, Johannes H. M. Maurer, Beate Reiser, Indra Backes, Juraj Drzic, Anika Kleemann, Andrea Pyttlik, Dr. Peng Zhang, Dr. Alberto Escudero, Dr. Thibaut Thai, Jonas Hubertus, and Dr. Daniel Brodoceanou. I always had a great time at work and beyond (“Kneipentour”), I enjoyed the inspiring discussions in and outside of the lab, and our funny group excursions. Special thanks goes to Dr. Lola González-García for her helpfulness, support, and advices, Dr. David Doblas-Jiménez for sharing his Python and Latex skills with me, Sebastian “Beck-Norris” Beck and Robert Strahl for any technical support, especially regarding the assembly of the analytical ultracentrifuge, and Thomas “Supraman” Kister with his unbelievable wide-ranging practical competences, who finds an easy solution to every problem.

I would like to express my sincere gratefulness to my office colleagues Dr. Lena Barnefske, Dr. Marc Schöneich, Dr. Viktoriia Barreau, Dr. Vikrant Naik, and Robert Strahl. It was always a nice and friendly atmosphere in the office and we always had good conversations during short breaks. I would like to thank in particular Dr. Aljosha Jochem, who always motivated and supported me during the thesis and suffered with me during numerous crossfit workouts, and Dr. Dominik Gerstner, who always had supporting advices related to the thesis but also life in general.

I appreciate the support of my experimental work by many of my colleagues: Anika Krieger, Sarah Schmidt, Kathrin Alt, and the students Ronja Anton, Christopher Scherrer, and in particular Anna Zimmermann. I would have not succeeded without these motivated and helpful colleagues. Thank you for your great effort.

Thanks goes to Jessica Gola, Lena Eisenhut, Frederik Scherff, and Dominik Britz. It was a great team of PhD students at the "Dillinger Hütte" and I enjoyed the official and unoffical meetings.

Particular appreciations go to the external collaborators and colleagues for their support in this research: Dr. Olga Borovinskaya from TOFWERK AG, Dr. Johannes Walter from University in Erlangen-Nürnberg, who supported our assembly and commissioning of the analytical ultracentrifuge, and Jörg Schmauch from Saarland University.

I would like to show my gratitude to all the colleagues at INM for their support during my time as a PhD student, in particular Dr. Marcus Koch, Andrea Jung, Dr. Yuliya Silina, Herbert Beerman, Joachim Blau, Werner Schneider, Christina Muth, Alexander May, and Robert Drumm.

I owe my deepest gratitude to my beloved family for their unlimited and selfless support and finally, I thank Aline with all my heart for her understanding for long lab days, her loving support, her infinite patience, and constant encouragement during the thesis.

Statement on contributions

Chapter 2:

- Dissolution experiments with reference particles were performed by Kathrin Alt and me.
- Chemical analysis by inductively coupled plasma optical emission spectroscopy (ICP-OES) was performed by Andrea Jung.

Chapter 3:

- Synthesis of silica nanoparticles was partially carried out by Dr. Aljosha Jochem, Anika Schwarz, and me.
- Particle characterization by field-flow fractionation was performed by Anna Zimmermann, Michael Kloß, and me.

Chapter 4:

- Particle characterization by field-flow fractionation was performed by Anna Zimmermann, Dr. Aljosha Jochem, and me.
- Particle characterization with STEM in combination with automatic image analysis was performed by Thomas Roth at AG der Dillinger Hüttenwerke in Dillingen, Germany.
- Carbon extraction replicas were prepared by Jürgen Vogt at AG der Dillinger Hüttenwerke in Dillingen, Germany.
- Manual image analysis of TEM micrographs was partially performed by Christopher Scherrer and me.
- Particle characterization with single particle inductively coupled plasma mass spectrometry (SP-ICP-MS) was performed by Dr. Olga Borovinskaya at TOFWERK AG in Thun, Switzerland.

Publication report

- Chapter 2 was partially submitted for publication as:

  “An improved method for the matrix dissolution extraction of nanoparticles from steel” by Andreas Hegetschweiler, Thorsten Staudt, and Tobias Kraus.

  The manuscript was submitted to the *Journal of Materials Science*.

- A manuscript including the results from section 4.1 is in preparation with the title: “Colloidal analysis of multimodally distributed particles extracted from microalloyed steel”.

- Section 4.2 was submitted for publication as: “Single particle mass spectrometry of titanium and niobium carbonitride precipitates in steels” by Andreas Hegetschweiler, Olga Borovinskaya, Thorsten Staudt, and Tobias Kraus.

  The manuscript was submitted to *Analytical Chemistry*.

Abstract

Microalloyed steels contain small amounts of Nb, Ti, and V, which precipitate as carbides, nitrides, or carbonitrides at different stages of thermomechanical processing. Particle sizes and compositions vary depending on when they form; their size and position set their effect on the microstructure and hence mechanical properties. Alloy design, process control, and the production of steels with curtailed properties require an understanding of the correlations between processing conditions, particle formation, and mechanical properties. The relations can be derived from the analysis of statistically relevant data on the distributions of precipitate size and composition.

This thesis provides a method to obtain such data through particle extraction by dissolution of the iron matrix in combination with colloidal analysis. The method is an alternative to commonly used electron microscopy of extraction replicas or thin films. Extraction protocols were systematically varied to obtain unagglomerated particles suitable for subsequent colloidal analysis with minimal particle losses. Colloidal analysis methods were evaluated by analysis of multimodal model particle systems for their suitability to analyze the broad size distributions of the precipitates. Analytical ultracentrifugation, field-flow fractionation, and single particle mass spectrometry were tested on particles extracted from steel and the results were compared to data from conventional metallography.

Zusammenfassung

Mikrolegierte Stähle enthalten kleine Mengen Nb, Ti und V, die während verschiedener Stufen des thermomechanisch gesteuerten Walzprozesses als Karbide, Nitride oder Karbonitride ausgeschieden werden. Partikelgrößen und -zusammensetzungen variieren je nach Entstehungszeitpunkt; deren Größe und Position bestimmen das Gefüge und somit die mechanischen Eigenschaften. Legierungsdesign, optimale Prozesskontrolle und die Herstellung von Stählen mit definierten Eigenschaften erfordern ein Verständnis der Zusammenhänge zwischen Prozessbedingungen, Partikelbildung und mechanischen Eigenschaften, die sich aus der Analyse statistisch relevanter Daten über die Verteilung der Ausscheidungsgröße und -zusammensetzung ableiten lassen.

In dieser Arbeit wird die Partikelextraktion durch Auflösung der Eisenmatrix in Kombination mit kolloidaler Analyse als Alternative zur Elektronenmikroskopie von Extraktionsreplika oder dünner Schichten erprobt. Extraktionsprotokolle wurden systematisch variiert, um unagglomerierte Partikel mit minimierten Verlusten zu erhalten, die für eine kolloidale Analyse geeignet sind. Verschiedene Analysemethoden wurden auf ihre Eignung für die Analyse der breiten Größenverteilung der Ausscheidungen untersucht. Analytische Ultrazentrifugation, Feld-Fluss-Fraktionierung und Einzelpartikel-Massenspektrometrie wurden mit multimodalen Modelpartikelsystemen und extrahierten Partikeln getestet und die Ergebnisse mit Daten der konventionellen Metallographie verglichen.

Contents

Chapter 1

Particles in microalloyed steels

Microalloyed (MA) steel is a category of high-strength low-alloy (HSLA) steels. Such steels were developed to provide better mechanical properties and atmospheric corrosion resistance compared to regular mild steel while retaining good weldability.[1] HSLA steels enable weight saving applications with thinner plates than conventional carbon steels, and compared to high alloyed steels, their application may be more economical due to low amounts of expensive alloy elements.[2] HSLA steels reach yield strengths σ_y of 350 to 800 MPa, while regular mild steels have yield strengths of 150 to 200 MPa and ductile-brittle transition temperatures above that of HSLA steels.[2, 3] These properties are exploited in pipeline and offshore constructions for the oil and gas industry, ship construction, and automobile and heavy goods chassis componets.[1–3] The term *HSLA* is defined by specific mechanical criteria rather than a defined composition.[1] Such steels typically contain between 0.05 and 0.25 wt.% C, up to 2 wt.% Mn, and Cr, Ni, Mo, Cu, Zr, or N. Microalloyed steels additionally contain small amounts of Nb, Ti, and/or V with quantaties of maximum 0.1 wt.% compared to other HSLA steel categories.[1] These elements precipitate as carbides, nitrides, and/or carbonitrides during the thermomechanical controlled rolling process (TMCP) and strongly influence the microstructures of the steels and hence, their mechanical properties.[3, 4]

The precipitates are formed at different stages of the TMCP and influence the microstructure and thus the mechanical strength in multiple ways. The next section describes the various strengthening mechanisms that are important for MA steels.

1.1 Strengthening mechanisms

The improved mechanical properties of the microalloyed steels can be ascribed to grain refinement by austenite conditioning and precipitation hardening. Solid solution strengthening by Mn, Si, or the microalloying elements in solution also contributes to the strength.[3] All three mechanisms are based on the same principle for improving the yield strength: the inhibition of dislocation movement in the metal crystal, which is described in more detail in the following.

1.1.1 Grain refinement

Grain refinement is one of the most effective strengthening mechanisms for metals. Grain boundaries are imperfections of the crystal lattice where the orientation of the crystal changes. They are impassable obstacles to dislocations. The slip plane of the dislocation is interrupted at the grain boundary and the dislocation cannot move further. Dislocations pile up at the grain boundary and their elastic strain fields form a common strain field. This strain field affects the neighbouring grains, where it activates dislocation sources that cause plastic deformation of the crystal. The maximal possible pile-up length in the grain depends strongly on the grain size and decreases for small grains. The resulting elastic strain field decreases accordingly with shorter pile-up length. Thus, in small grains, the force generated for dislocation activation in the neighbour grains is decreased and an additional force is required to activate the dislocation sources. As a result, the yield strength increases with decreasing grain size. The relationship between grain size and yield strength σ_y of a metal was found by Hall [5] and Petch [6]:

$$\sigma_y = \sigma_0 + \frac{k_y}{\sqrt{d_{grain}}} \tag{1.1}$$

with the mean grain size d_{grain}, the material constants σ_0 as the starting stress for dislocation movement, and k_y as the strengthening coefficient.

All strengthening mechanisms but grain refinement increase yield strength, but decrease toughness. Grain refinement is the only strengthening mechanism that increases both yield strength and toughness and additionally decreases ductile-brittle transition temperature.[7]

1.1.2 Precipitation hardening

Precipitation hardening is caused by small second phase precipitates in the crystal lattice that form during cooling from a homogeneous phase. The precipitates are obstacles for dislocations and increase yield strength. Two mechanisms dominate the interaction between precipitates and dislocations: particle bypassing by Orowan looping [8] and particle shearing. The first mechanism occurs for "hard" particles forming a coherent phase boundary with the matrix, where the resistance force of the particles against deformation is higher than the applied force, and for particles that form a semi-coherent or incoherent phase boundary. The dislocation has to bow around the precipitates to pass them and a dislocation loop is left around the precipitates (Figure 1.1 a). The second, "Fine-Kelly", mechanism occurs for "soft" particles, where the resistance force of the particles is smaller than the applied force, and it is possible for the dislocations to move through the particles by shearing them (Figure 1.1 b). This mechanism requires particles that form a coherent interphase with the surrounding matrix. Different effects like interfacial strengthening or antiphase strengthening influence the shearing of the particles and contribute to the increase in yield strength.[9] Fine-Kelly mechanism does not occur in microalloyed steel and shall not be discussed in more detail.[9]

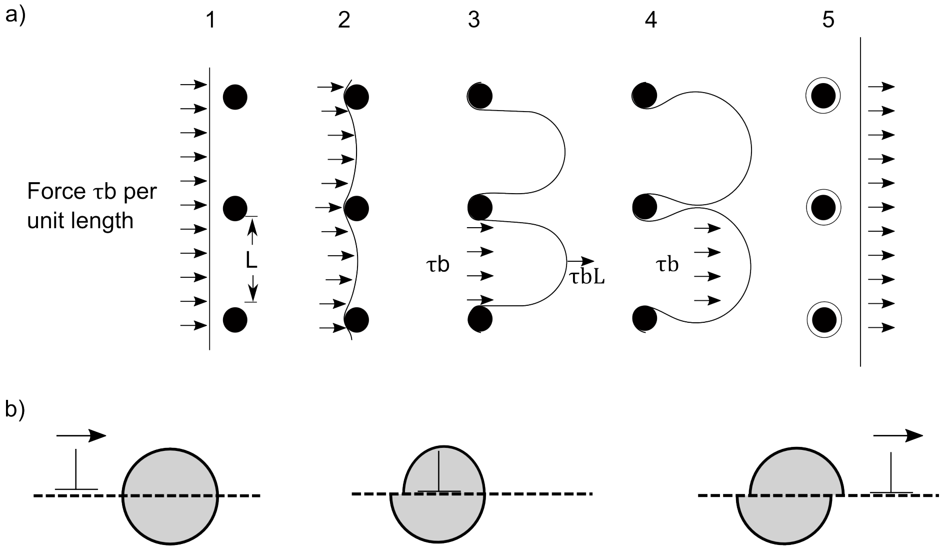

Figure 1.1: Mechanisms for overcoming obstacles (second phase precipitates) by dislocations. a) Orowan looping: the dislocation bends around the particle, leaving behind dislocation rings. b) Shearing of particles (Fine-Kelly mechanism). Illustration based on [9].

Ashby modified the Orowan model by taking into account the inter-particle spacing and the effects of statistically distributed particles. Equation (1.2) describes the increase in yield shear stress $\Delta\tau_y$ according to the

Ashby-Orowan model [9]

$$\Delta\tau_y = \frac{0.84 \cdot Gb}{\pi L} \cdot \ln(\frac{x}{2b}) \tag{1.2}$$

with the shear moduls G, Burgers vector b, the particle spacing L, and the particle diameter x. Equation (1.2) can be expressed in terms of increase in tensile stress $\Delta\sigma_y$ using the Taylor factor for polycrystalline materials:

$$\Delta\sigma_y = \frac{0.538 \cdot Gb \cdot \phi^{0.5}}{x} \cdot \ln(\frac{x}{2b}) \tag{1.3}$$

with the volume fraction of the particles ϕ.

Experimental relations between the yield strength of microalloyed steels, particle size, and particle volume fraction show very good agreement with the Ashby-Orowan equation (equation (1.3)).[9] Figure 1.2 shows the relationships between particle size, volume fraction, and increase in yield strength with respect to an unalloyed steel. The yield strength increases with decreasing particle size and increasing particle volume fraction.

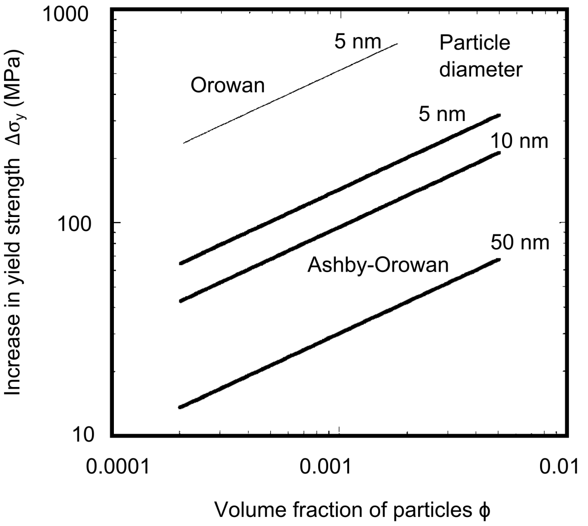

Figure 1.2: Increase in yield strength depending on the precipitate volume fraction for different precipitate sizes according to the Ashby-Orowan model. Illustration modified from [9].

Figure 1.2 clearly illustrates the root dependency of the yield strength on the particle volume fraction by the linear slope of 0.5 in logarithmic scale. The influence of the particle size on the yield strength in equation (1.3) is dominated by the reciprocal of the particle size over the logarithmic term. Thus, small particles (with sizes below 10 nm) can contribute storngly to yield strength increase and are favorable for yield strength improvement. Precipitation hardening causes major yield strength improvement in microalloyed steel; reducing the particle size and increasing the particle volume fraction are important goals of microalloyed steel process optimization.[9] In contrast to grain refinement, the increase in yield strength by precipitation hardening is associated with a decrease in toughness.

1.1.3 Solid solution strengthening

Solid solution strengthening is based on the local distortion of the crystal lattice by foreign atoms. They can either occupy original lattice sites and replace the host atoms in substitutional solid solution or occupy the interstitial lattice sites in an interstitial solid solution (e.g. C in Fe). In both cases, the crystal lattice is locally distorted and the movement of dislocations is hindered. Additionally, the foreign atoms induce a local change in the shear modulus, which impedes dislocation sliding. Finally, the foreign atoms lead to a decrease in the stacking fault energy resulting in a larger spreading of the dislocations (“Suzuki effect”) at the foreign atoms.[10]

In MA steels, the three strengthening mechanisms are related to the addition of the three microalloying elements Nb, Ti, and V, which are described in more detail in the following section.

1.2 Microalloying elements

The addition of the microalloy elements Nb, Ti, and/or V improves strength and thoughness of microalloyed steels compared to regular plain carbon steels.[1, 3] All three elements are transition metals: Titanium belongs to the fourth side group (IVa) and vanadium and niobium belong to the fifth side group (Va) of the Periodic Table of the Elements. Titanium is chemically very active and forms compounds with O, S, C, and N. Due to the strong affinity to O, Ti can only be used in fully killed Al-steels (completely deoxidized by the addition of Al).[1] The elements of the group Va show less affinity to O and S and mainly form carbides and nitrides.[1, 11] The carbides and nitrides of Ti, Nb, and V appear in steel in different phases. The most common phase has a B1 NaCl (Fm3m) face-centred cubic (fcc) structure. The carbides and nitrides are formed according

$$[\mathrm{M}] + [\mathrm{X}] \longleftrightarrow (\mathrm{MX}), \tag{1.4}$$

where [M] stands for the concentration of the metal (Nb, Ti, or V), [X] stands for the concentration of the interstitial atoms (C or N) and (MX) stands for the concentration of the constituent phase.[4] The phases are isomorphous for all three metals and have similar lattice parameters. They are mutually soluble and besides the pure MX phase, complex carbonitrides with the chemical formula $Ti_vNb_wV_xC_yN_z$ can form as a homogenous phase.[3, 9, 11, 12] The phases are stable over a wide concentration range and are often referred to as MX_z, where z stands for the mole ratio of X and M. It is a direct indicator for the number of vacancies inside the carbonitride.[11] Vanadium constitutes an exception: VC does not exist in the stoichiometric composition and it is only stable in a range of $VC_{0.73}$ -$VC_{0.89}$. Therefore, it is often referred to as V_4C_3.[13]

The microalloy elements can also form carbide and nitride phases with a hexagonal close-packed (hcp) crystal lattice.[13] In Nb alloyed steels, long austenitization times $\geq 150\,\mathrm{h}$ and high Nb ($\geq 0.1\,\mathrm{wt.\%}$) and N ($\geq 0.012\,\mathrm{wt.\%}$) contents enforce the formation of hexagonal phases such as Nb_2CN.[11]

The affinity of the different microalloy elements for carbon and nitrogen varies considerably, resulting in a different solubility of the different carbides and nitrides in the iron matrix. The solubility of the metal carbide or nitride in the iron matrix is described by the solubility product:

$$k_\mathrm{s} = \frac{a_{[\mathrm{M}]} \cdot a_{[\mathrm{X}]}}{a_{[\mathrm{MX}]}} \tag{1.5}$$

with the equilibrium constant k_s, the activity $a_{[\mathrm{M}]}$ of the dissolved microalloy element, the activity $a_{[\mathrm{X}]}$ of the dissolved interstitial element, and the activity $a_{[\mathrm{MX}]}$ of the constituent phase. In chemistry, k_s is usually defined as reciprocale of the solubility product in equation (1.5), but the introduced form is widely used among metallurgist.[4]

The lower the solubility product, the less soluble is the metal in the iron matrix and the stronger is the driving force for precipitation formation. In general, the metal nitrides are less soluble than the metal carbides and the solubility in the austenite is much higher than in the ferrite. Figure 1.3 shows the solubility of the different metal carbides and nitrides in the iron matrix in dependence of the temperature.

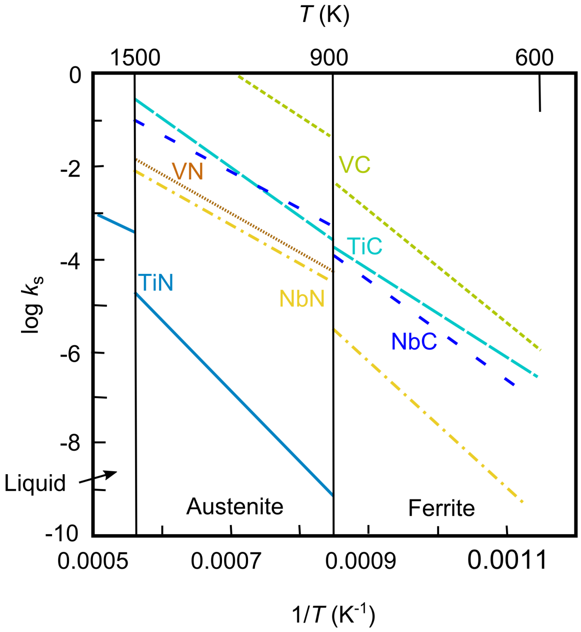

Figure 1.3: Solubility products of the different microalloy carbides and nitrides in iron. Modified from [4].

Figure 1.3 indicates that TiN has by far the lowest solubility of all constituents and partially precipitates already in the liquid phase; it is followed by NbN > VN > NbC > TiC. VC shows the highest solubility. VN and NbN are rarely formed in commercial microalloyed steel due to the low nitrogen content and the high affinity of Ti for N; Nb and V normally precipitate as carbides or carbonitrides.

Knowledge of the solubility products of the various metal carbonitrides is important for the steel processing. It allows to determine the soaking temperature and soaking time necessary to dissolve the carbides and nitrides in the steel slab during the first processing step. This is particularly necessary with regard to precipitation hardening. Soaking times selected too short result in incomplete dissolution of the particles, impeding a later precipitation hardening. Soaking times selected too long lead to grain coarsening and reduce the gain in yield strength achieved by grain refinement.

Furthermore, the solubility products allow the prediction of the precipitates formed during processing in dependence of the alloy content. The mechanisms which contribute to the improvement of the mechanical properties can thus be controlled by adapting the alloy design. Another possibility to influence the precipiation behavior are the parameter during the thermomechanical controlled rolling process. By adjusting, for example, the temperature profile or the degree of deformation during TMCP, the precipitation size and composition can be controlled. This strongly influences the microstructure and hence the mechanical properties of the steel.[11, 12]

1.3 Thermomechanical controlled rolling process

Thermomechanical controlled rolling is a metallurgical process designed to improve the mechanical properties of materials by controlling the hot-deformation process. It combines mechanical deformation such as rolling with thermal processes like heat treatment or water quenching into a single process and it is closely linked to the manufacturing of microalloyed steels. The TMCP consists of three major steps [14]:

1. Reheating
2. Rolling (rough and finish rolling)
3. Accelerated cooling

In the processing of microalloyed steel, the main objective of the TMCP is strengthening by ferrite grain refinement and precipitation hardening. Without TMCP, the smallest grain sizes that can be achieved are in the range of 5 to 10 µm.[3] With TMCP, further grain size reduction down to 1 to 3 µm is possible, resulting in an increase in yield strength up to 350 MPa.[3, 12, 14] Figure 1.4 gives an overview of the different process stages.

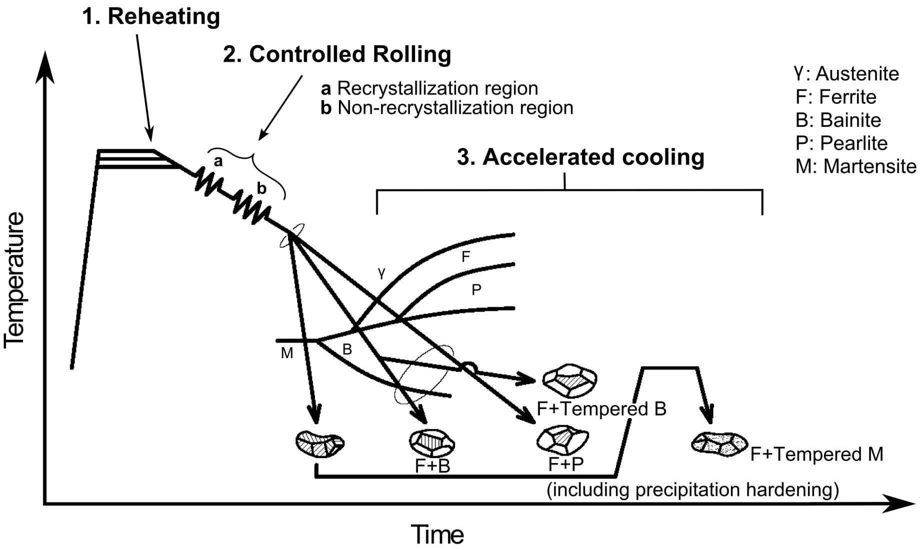

Figure 1.4: Overview of the thermomechanical controlled rolling process: 1) the sample is reheated. 2) controlled rolling. 3) accelerated cooling. Illustration adopted from [14].

Reheating is performed to dissolve most of the microalloying elements that precipitated after casting of the steel slab and make them available for controlled precipitation during later processing steps. The steel slab is heated to approximately 1000 to 1250 °C. At these temperatures, TiN and to a lesser extent NbCN precipitates are still partially stable and do not completely dissolve. The precipitates, with diameters on the order of 300 nm, are located at the austenite grain boundaries, where they prevent grain boundary moving by Zener-pinning and thus impede grain coarsening by Ostwald ripening.[3, 12, 14, 15]

After reheating, the steel slab is cooled down to temperatures of around 900 °C and subjected to several rolling steps that cause well-defined deformations. The steel plate is strongly deformed and a large number of dislocations form. Rough rolling is performed at temperatures above recrystallization temperature and a defect free steel plate is obtained. The steel plate cools down to temperatures below recrystallization temperature, but in the austenite region, and finish rolling is performed. Microalloy elements, mainly Nb, retard the recrystallization by strain induced precipitation (SIP) or, to a lower extent, solute drag.[12, 15] The diameters of the precipitates formed in this step are around 50 nm.[14] After rolling, the grains are elongated ("pancaked") and highly deformed, containing a large number of dislocations. Due to recrystallization retardation, the deformed microstructure is stable until the $\gamma-\alpha$ transition temperature. The large number of lattice defects leads to a markedly increased number of ferrite grain nuclei and a fine grained ferrite microstructure is formed.[12, 14]

The accelerated cooling step forms small precipitates with sizes $< 10\,\text{nm}$ during or after the $\gamma - \alpha$ transition; they increase the mechanical strength by precipitation hardening.[14, 15] Especially V-containing steels take profit of this step. The high solubility of V in the austenite phase down to low temperatures results in a large amount of V, which is available for precipitates of fine VC precipitates.

The precipitation of the microalloy carbonitrides is complex and depends on the alloy design and temperature profile. Pure carbides and nitrides as well as complex precipitates with varying compositions of $\mathrm{Ti}_v\mathrm{Nb}_w\mathrm{V}_x\mathrm{C}_y\mathrm{N}_z$ and homogeneous or heterogenous phases can form.

Cooling conditions influence the microstructure, too. The cooling rate leads to different non-equilibrium phases such as bainite or martensite that strongly influence the yield strength and ductility of the steel.

Many parameter such as alloy design, rolling temperature or deformation degree play a crucial roll for the final microstructure and thus for the mechanical properties. To improve the product and the production process, the precipitate state has to be linked to the different stages of the production process and to the resulting microstructure and mechanical properties. Size and composition analysis of the precipitates therefore are an important aspect of product and process optimization.

1.4 Metallographic particle characterization

Figure 1.5 illustrates the sizes of the sample sections and particle size ranges that can be examined by common metallographic particle characterization methods. The accessible particle diameter correlates with the size of the sample section studied: The larger the sample section, the lower the resolution of the analysis method, and the larger the smallest particle diameter that can be analyzed. Light microscopy (LM) and spark emission spectrometry cover relatively large sample sections; they are mainly used for the analysis of inclusions with sizes in the µm range. Scanning electron microscopy

(SEM) resolves particles with sizes of approximately 20 nm[1], but the contrast of smaller particles in the iron matrix is low and the number of particles that can be unambigously analyzed is limited.[17] Atomic force microscopy (AFM) enables the analysis of particles down to sizes of a few nanometers. (Scanning) transmission electron microscopy ((S)TEM) or atom probe tomography (APT) provide atomic resolution.

Common particle characterization in steel industry is performed by analyzing carbon extraction replicas, metallographic sample sections, or electron transparent foils. These specimens provide particles in a two dimensional cross section. Another approach is the analysis of particles extracted from the steel sample by dissolution of the iron matrix.

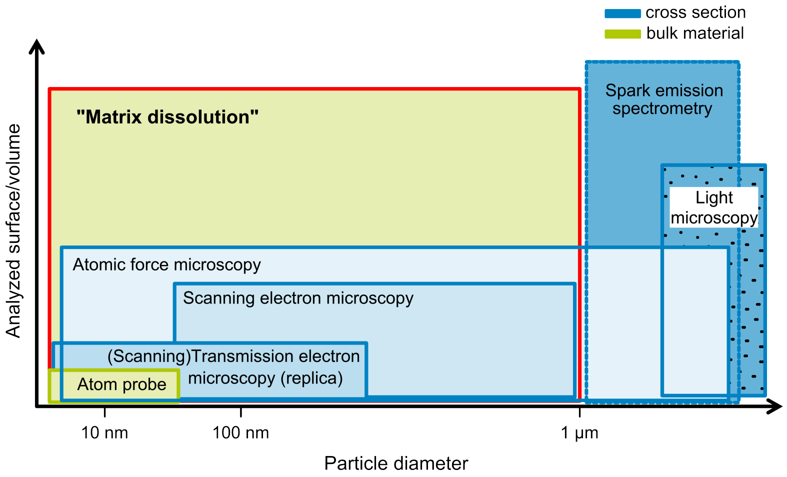

Figure 1.5: Analysis methods for particle characterization in steels. Methods that analyze sample cross sections are blue, methods that analyze the sample volume are green.

The smallest precipitates in microalloyed steel with sizes of only a few nanometer require (S)TEM on electron transparent foils or carbon extraction replicas or particle extraction by matrix dissolution followed by analysis with (S)TEM or other methods like X-ray diffraction (XRD).[18] Electron microscopy (EM) allows a detailed analysis of the particles in terms of size, shape, and morphology and concurrent chemical analysis of the particles. A

---

[1] The resolution limit in modern field emission gun SEMs is approximately 1 nm (Gold nanoparticles on carbon substrate at an accelaration voltage of 30 kV).[16] However, the resolution depends on acceleration voltage, particle and substrate material. For microalloy carbonitride particles, the resolution is decreased, especially if particles are analyzed in the bulk steel sample.

	Geometric characterization	Chemical characterization
SEM	secondary electron (SE), backscattered electrons (BSE)	energy dispersive X-ray analysis (EDX) , wavelength dispersive X-ray analysis (WDX)
TEM	bright field (BF), dark field (DF), energy electron loss spectroscopy (EELS), energy filtered TEM (EFTEM),	EDX, WDX, EFTEM, EELS, selected area diffraction (SAD)
STEM	bright field, annular dark field (ADF), high angle annular dark field (HAADF)	EDX, WDX

Table 1.1: Imaging modes and chemical characterization methods available in electron microscopy.

brief summary of the different imaging modes and chemical characterization methods available in EM is given in Table 1.1. Atom probe tomography analyzes a very small sample section of only a few small precipitates in the size range $< 20\,\text{nm}$ with full 3-D atomic information on the precipitates.[19]

1.4.1 Extraction replica and TEM foils

TEM analysis of carbon extraction replicas or thin foils is the most common approach in steel industry to characterize particles in microalloyed steels. TEM foils are produced by target preparation with focused ion beam (FIB) or by thinning metallic specimens using electrochemical polishing. The thickness of these foils is on the order of 150 nm. The main advantage of electron transparent foils is that it provides spatial information on the particles. Local relationships among individual precipitates (e.g. precipitates are formed in a row) or between precipitates and ferrite matrix (e.g. precipitates are formed at the grain boundary) can be examined. TEM foils also enable the study of the crystallographic orientation relationship between precipitates and ferrite matrix.[20] A drawback is the interaction between the electron beam and the magnetic field of the iron matrix that severely complicates analysis.[17, 21, 22] Furthermore, TEM shows only a 2D projection of the particles. In this projection, individual, spatially separated particles can be imaged as one large particle due to the overlapping of the two projections. During sample preparation, particles may be sectioned distorting the projected diameter [23, 24] and other artefacts during sample preparation might be introduced.[22]

Carbon extraction replicas were established by Smith and Nutting as a modification of the conventional replica technique.[25] Carbon extraction replicas are beneficial for the detailed study of the morphology and chemical constitution of secondary phase particles in multiphase alloys, e.g. microalloyed steels. The replicas are produced from metallic specimen surfaces. A metallic cross section is produced by metallographic specimen preparation comprising grinding and polishing. The cross section is then etched such that the structure is readily visible in the light microscope. A carbon film with a thickness of approximately 3 to 20 nm is evaporated on the sample surface. Then, the film is stripped off the surface by electropolishing or chemical etching. The floating film is washed in acid and water, collected on mounting grids, and dried.[23, 25–29] Figure 1.6 illustrates the preparation of a carbon extraction replica.

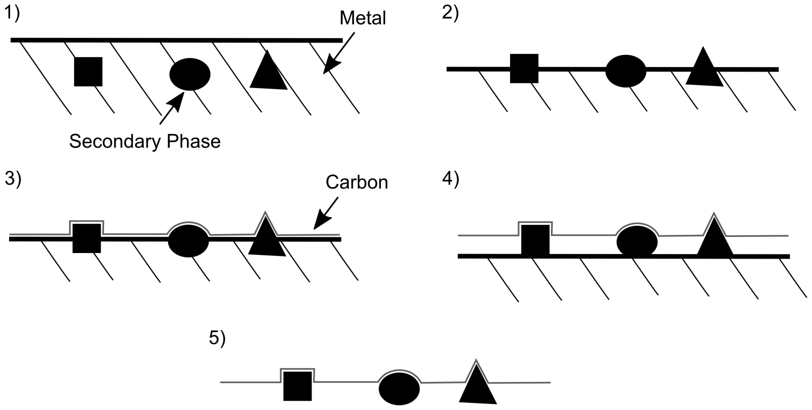

Figure 1.6: Different steps to produce a carbon extraction replica: 1) Metal sample with secondary phase precipitates. 2) Etching of surface to reveal the precipitates. 3) Coating of surface and precipitates with carbon layer. 4) Removing of the carbon layer containing the precipitates by further etching. 5) Final carbon extraction replica. Illustration modified from [26].

The main advantage of extraction replicas is that there are no interferences of the metal matrix.[25, 26] The amorphous carbon matrix enhances the contrast of the crystalline precipitates and the chemical characterization is improved due to the absence of iron. The thickness of electron transparent foils is often unequal and only a small area is transparent to electrons. The carbon film used in carbon extraction replicas is uniformly thin and electron transparent. The useful area is therefore considerably higher than that of TEM films. The risk of overlapping particles is also reduced.[23, 24] A disadvantege of the extraction replica is the extraction efficiency. It is rarely 100 %, might be size dependent, and varies from replica to replica. This impedes in particular the determination of the volume fraction of the particles.[23, 24, 28] Etching may attack (small) particles and (partially) dissolve them.[27, 30] The carbon film will not allow a chemical characterization of the carbon content of the precipitates. This problem can be solved by using other extraction materials like AlO_x.[21, 31]

Most studies in the last decades on microalloy precipitates are based on transmission electron microscopy of carbon extraction replicas.[17, 21, 32–43] All studies examined the particle size distribution and/or particle composition depending on different parameters such as alloy composition or process parameter during TMCP. In many studies, the structure-property relationship was examined.

A general drawback of electron microscopy is the small sample volume which is analyzed. It is in the size range of $10\,\mu\mathrm{m}^3$ [18] that may not be representative.[22] It is difficult to obtain statistical meaningful data in the TEM due to a relatively small number of particles that can be analyzed. Performing manual image analysis of TEM micrographs is time consuming; most studies report on below 10^3 particles.[34, 42, 44] This can be sufficient for monomodal, narrowly distributed particles [45, 46], but leads to significant deviations in broad multimodal distributions. In order to obtain statistically meaningful results, at least 10^4 particles should be analyzed in such particle systems.[47, 48] Furthermore, the contrast of small particles is distinctly reduced compared to larger particles, which increases the chance of not detecting small particles. This can lead to erroneous results due to undercounting of small particles.[49] Finally, the analysis time for a detailed chemical analysis is very time-consuming and only a few particles can be characterized within a reasonable period of time. For example, Tirumalasetty et al. [36] determined the average Ti/Nb ratio in TiNb carbonitrides in microalloyed steel by analyzing only 7 particles.

1.4.2 Matrix dissolution technique

An alternative approach for particle analysis is the matrix dissolution technique. Here, the particles are extracted from the iron matrix by chemical [50–59] or electrolytic [60–65] dissolution of the iron matrix, while the particles remain intact. This technique has been applied since the first half of the last century; it was initially developed to analyze non-metallic inclusions and precipitates in steel and metals.[50, 52–55] The matrix dissolution technique has also been applied on microalloyed steels to analyze niobium, titanium, and vanadium carbonitrde particles.[58, 63–65] It extracts particles from a volume that can be individually adjusted but typically varies between 0.1 to

$1\,\mathrm{cm}^3$ and thus averages over a much bigger sample area or volume.

Chemical dissolution dissolves the sample by oxidizing the Fe atoms. Oxidants can be acids [51, 59], halogens [52], or other compounds that have a higher oxidation potential than Fe. The process requires no attention, is easy to perform in any chemistry lab with standard laboratory equipment, and one can dissolve multiple samples at a time. The disadvantage of chemical dissolution is the poor control over the reaction and the existing potentials. The dissolution reaction is therefore difficult to control and there is a risk of attacking the particles to be extracted. A further drawback is the formation of SiO_x networks [58] that can engulf the extracted particles and impede their detailed analysis.

An alternative is electrolytic dissolution. The sample is connected as an anode in the electrical circuit and immersed in an electrolyte. A platinum sheet is used as cathode and the sample is dissolved by applying a DC current. The electrolyte is often based on an organic solvent [58, 65, 66], but aqueous electrolytes are possible, too.[64] The electrolytic dissolution provides better control of the applied potential and thus enables gentler extraction. Reduction of SiO_x formation has been reported.[58] However, particle extraction is slower than for chemical extraction [58, 66] and requires a potentiostat.

After extraction, the residue is separated from the dissolved constituents and washed, for example, with filters. This is a very time efficient method to separate the residue from the supernatant. The minimum size of the particles which can be isolated, however, is limited by the filter pores, commonly $> 200\,\mathrm{nm}$ [55, 57], which results in a loss of smaller particles. Centrifugation exploits the density of the particles and forms a residue.[58, 64] After centrifugation, the supernatant is removed and replaced with fresh water. Several centrifugation cycles are necessary to completely remove the dissolved components. This method allows to extract even the smallest nanoparticles.[58]

The matrix dissolution method was originally developed for the identification and quantification of the soluble elements in the supernatant and the composition of the insoluble residue. To this end, the supernatant and the digested residue were analyzed using the corresponding wet chemical detection reactions or spectral analytical methods or mass spectrometry.[55, 57, 63, 67] Another characterization method, which has been used in the early days, is XRD analysis of the dried extraction residue. It gives information about the insoluble phases (particles) and their crystallite size. This yields statistically relevant average data of many particles, while the information on the particle distribution in the steel is lost.[55]

In more recent studies, particles were analyzed using Rietveld refined XRD [67, 68] and electron microscopy [58, 61, 63, 66] to provide information about the phase, the quantitative composition, and the crystallite size of particles extracted from microalloyed steel.[67, 68] To analyze the extracted particles in (S)TEM, a small drop ($\sim 2.5\,\mu\text{L}$) of the particle suspension is dried on a substrate suitable for sample characterization in (S)TEM, usually a copper grid coated with an amorphous carbon film or SiN membranes.

(S)TEM is a powerful characterization method providing information on the geometry and chemical composition. But only a limited number of particles can be analyzed (see section 1.4.1). Compared to the analysis of TEM foils or carbon extraction replicas, however, (S)TEM analysis of the extracted particles has the advantage that the number of particles per area is strongly increased and no interfering effects from the iron matrix appear.

In this thesis, alternative methods will be explored to characterize the particles. The particle extraction method provides (nano)particles that are suspended in a liquid. At this stage, in the field of colloidal chemistry, there are well established methods, which analyze these systems regarding their size distribution and chemical composition. These methods rapidly analyze large numbers of particles and provide statistically meaningful data. Only few attempts were made to analyze the particles this way [69, 70] and no scientific literature can be found with regard to this approach.

1.5 Structure of the thesis

An ideal particle characterization method would rapidly analyze the size distribution and chemical composition of $> 10^4$ particles. The goal of this thesis was to develop better methods for the particle extraction from microalloyed steels followed by particle analysis using colloidal characterization methods that fulfils above demands.

In chapter 2, a standard extraction protocol and derived modified extraction protocols are investigated and their effect on particle etching, particle stability, and on the formation of SiO_x networks is examined. An optimized extraction protocol is provided that reduces particle losses and provides unagglomerated particles without SiO_x network formation.

In chapter 3, colloidal characterization methods, which are suitable for the size analysis of broad, multimodally distributed particle systems, are explored. Multimodally distributed model particle systems with well-known size distributions are analyzed with different colloidal methods and their suitability for the analysis of such particle systems is evaluated.

In chapter 4, particles extracted from microalloyed steels are analyzed using colloidal methods. In the first part (section 4.1), the methods found to successfully analyze model particle mixtures (chapter 3) are applied to extracted particles and the results are compared to electron microscopy. In the second part (section 4.2), extracted particles are analyzed by single particle inductively coupled plasma mass spectroscopy that enables the concurrent analysis of particle size and composition. The results are compared to electron microscopy.

Chapter 2

Particle extraction[1]

This chapter reports on an extraction protocol that isolates Nb and Ti carbonitride particles from microalloyed steel and provides a stable suspension of unagglomerated particles that can be analyzed by colloidal methods and electron microscopy. I studied different extraction protocols to examine which protocol provides the best extraction result. Three problems were overcome during particle extraction: particle loss due to etching of particles, SiO_x network formation, and agglomeration of the particles.

2.1 Extraction procedure

A microalloyed steel (Grade X100) provided by the AG der Dillinger Hüttenwerke was chosen to study different particle extraction protocols. The steel sample analyzed contained Nb, Ti, and V, and other alloy elements, such as Cr, Mn, and Si, which possibly interact with the extraction reagents or influence the extraction process, respectively. Cu, Ni, and Mo were not alloyed. The composition of the sample is given in Table 2.1. The sample is suitable to study the extraction of Nb, Ti, and NbTi-carbonitrides, which are important for grain refinement and precipitation hardening and affect the steel microstructure during all stages of the TMCP. The production process of the steel was aimed to obtain only these microalloy carbonitride precipitates. Precipitates containing V were not expected in the present sample due to the cooling conditions and alloy design. Thus, I will focus here on the extraction of Nb and Ti-containing carbonitrides.

A common matrix dissolution protocol to study insoluble contents in iron-

---

[1] Parts of this chapter were submitted for publication in a manuscript entitled “An improved method for the matrix dissolution extraction of nanoparticles from steel” by Andreas Hegetschweiler, Thorsten Staudt, and Tobias Kraus.

Element	C	Si	Mn	N	Cr	V	**Nb**	**Ti**	CEV*
wt%	0.07	0.35	1.9	0.003	0.2	0.04	**0.05**	**0.02**	0.44

*CEV = Carbon Equivalent Value [3]

Table 2.1: Elemental composition of the examined steel. Cu, Ni, and Mo were not alloyed.

based metals is the ASTM standard E 194-10[2] [71]: 1 g of steel chippings (priorly washed with isopropyl alcohol and acetone) was dissolved in 20 mL hydrochloric acid (HCl) with a concentration of 6 mol/L. The samples were completely dissolved at room temperature. After the samples have been fully dissolved, the solution was heated to boil, 30 mL of ultrapure water (UPW) were added, and the mixture was heated to boil again.

The protocol was then systematically varied. One gram of sample was added to 50 mL of each of 6 mol/L HCl, 2 mol/L sulfuric acid (H_2SO_4), 0.5 mol/L H_2SO_4, and 0.5 mol/L H_2SO_4 and 0.1 vol.% Disperbyk-2012 (Byk additives, Germany). One additional sample was dissolved with 200 mL of 0.5 mol/L H_2SO_4. All etching solutions were heated to 70 °C in an oil bath and stirred at 200 rpm. In contrast to the ASTM standard, the samples were left to cool after dissolution was complete.

In the next step, the samples were sonicated in an ultrasonic bath. Then, the particle suspension was split in two 25 mL aliquots and centrifuged in an ultracentrifuge (XL-I 70 K, Beckman-Coulter) at 113 000 rcf and 20 °C for 120 min (180 min for the sample with dispersant) to remove the dissolved iron. After the first run, the supernatant was removed (20 mL) for elemental analysis by optical emission spectroscopy with inductively coupled plasma (ICP-OES). Seven more centrifugation cycles were necessary to remove most of the iron salt from the particle suspension and reach an iron concentration of $< 5 \times 10^{-3}$ mmol.

The extracted particles were subsequently analyzed in TEM and by elemental analysis. For TEM, a droplet of 2.5 µL was dried on a copper grid coated with carbon. For elemental analysis, 5 mL of an acid mixture composed of 25 mL HCl (37%), 8 mL nitric acid (HNO_3) (65%), and 17 mL UPW were added to the extracted particles (≈ 5 mL). The solution was subsequently transferred into a teflon microwave container and 1 mL of hydrofluoric acid (HF) (50%) was added. The sample was then dissolved by microwave digestion (0 to 800 W ramp in 60 min, constant 800 W for 90 min) in a pressure vessel ($p_{\max} = 60$ bar), filled up to 50 mL with UPW, and analyzed

---

[2] In the standard procedure, 5 g of steel are dissolved in 100 mL HCl with a concentration of 6 mol/L and 150 mL water are added after boiling.

[3] $\mathrm{CEV} = \mathrm{C} + \mathrm{Mn}/6 + (\mathrm{Cu} + \mathrm{Ni})/15 + (\mathrm{Cr}+\mathrm{Mo}+\mathrm{V})/5$

by ICP-OES.

The time for steel sample dissolution depended on the extraction protocol. The ASTM standard protocol dissolved 1 g of steel in 3 days at room temperature. Increasing the temperature to 70 °C, increasing the etchant volume, and increasing the acid concentration decreased the steel dissolution time: a sample of 1 g was dissolved after 100 min in 6 mol/L HCl, after 180 min in 2 mol/L H_2SO_4, and after 460 min in 0.5 mol/L H_2SO_4. A further increase of etchant volume to 200 mL at a constant acid solution concentration did not markedly influence the dissolution time: 1 g of steel sample was dissolved in 420 min in 200 mL 0.5 mol/L H_2SO_4.

2.2 Particle etching

Etching of particles during extraction process occurs, but has rarely been considered in literature. Brunckovà et al. [59] reported on the choice of extraction times for Nb and Ti carbonitride particles and found that the extraction yield of Nb and Ti decreased for longer times due to etching of particles. They could not distinguish between nanoparticle loss and etching of nanoparticles since they used a filter with a pore size of 0.25 mm to separate the extraction residue from the solution.

Niobium and titanium carbides, nitrides, and carbonitrides bulk materials are nearly insoluble in H_2SO_4 or HCl at room temperature, but are dissolved in HNO_3 and HF. Temperature is important for the dissolution of the particles, too, since boiling in concentrated sulfuric acid readily dissolves NbC.[72–75] The data on the chemical stability of Nb and Ti carbides and nitrides is determined for bulk material or powders with particle sizes of approximately 50 µm. But the chemical behavior of nanoparticles often differs from bulk materials and the influence of the extraction protocol on the particle etching requires a deeper study.

2.2.1 Particles extracted from steel

I studied the dissolution of NbCN and TiCN nanoparticles during particle extraction by chemical analysis of the supernatant after the first centrifugation run by means of ICP-OES. The amount of dissolved Nb and Ti was determined assuming that all alloyed Nb and Ti in the steel had precipitated as carbonitrides. It makes sense to assume this, because the temperature ramp during the TMCP for the analyzed steel was chosen such that, thermodynamically all Nb and Ti is supposed to be fully precipitated. This was proven by additional experiments ("vide infra" for details).

The centrifugation time was chosen such that all particles with an equivalent sphere diameter of at least 7 nm are supposed to be completely sedimented. Additionally, due to the high salt concentration and the resulting high ionic strength after iron matrix dissolution, the particles are mainly in an agglomerated state and thus, particles with diameters smaller than < 7 nm will sediment as well. All Nb and Ti in the supernatant arises from dissolution of the particles and all Ti and Nb found in the supernatant is supposed to originate from etched particles.

I found dissolved Ti and Nb in the supernatant of all extraction protocols, with quantities that strongly depended on the extraction protocol. Figure 2.1 a shows the amount of titanium found in the supernatant after the first centrifugation run referred to the total amount of alloyed titanium and the extraction yield, defined as the amount of titanium in the extraction residue referred to the total amount of alloyed titanium.

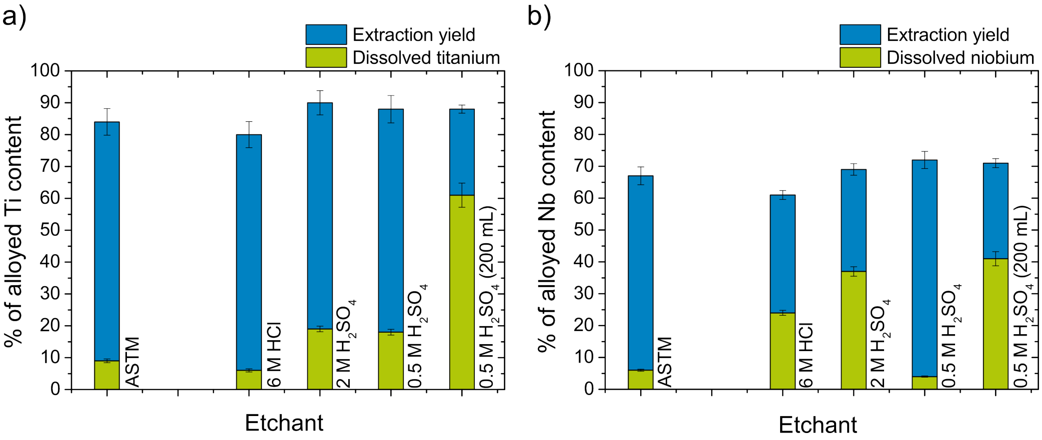

Figure 2.1: Dissolved a) titanium and b) niobium in the supernatant (green) after the first centrifugation run and extraction yield (blue) of both elements after the 8th centrifugation for different extraction procedures.

The supernatant contained approximately 9 wt.% of dissolved Ti for the sample that was dissolved according to the ASTM standard procedure and the Ti extraction yield was 75 wt.%. Increasing temperature and acid volume (6 mol/L HCl) did not much affect the titanium content in the supernatant or the extraction residue. Replacing HCl by H_2SO_4 markedly increased the particle etching, whereby particle etching was more pronounced for higher acid concentrations. Increasing the acid volume further increased the amount of dissolved Ti.

For niobium (Figure 2.1 b), the ASTM protocol led to 6 wt.% dissolved Nb at an extraction yield of 66 wt.%. Increasing the volume and the temperature strongly increased the amount in solution. Replacing 6 mol/L HCl solution with 2 mol/L H_2SO_4 led to even higher particle etching. Lower acid concentration (0.5 mol/L H_2SO_4) caused significantly less particle etching. Increasing the acid volume further from 50 mL to 200 mL led to a markedly increased particle etching.

Acid volume, acid concentration, acid type, and temperature used in the extraction protocol influenced the amount of Nb and Ti found in the supernatant and the residue, respectively:

- A higher acid volume increased particle etching for both Nb as well as Ti carbonitride precipitates. Small etchant volumes are thus favourable for particle extraction with regard to loss of particles by particle etching.
- The acid concentration markedly influenced the amount of Nb found in the supernatant and the residue, respectively. Lower acid concentrations lead to lower losses and higher extraction yields. In contrary, Ti carbonitrides did not show a dependency on the acid concentration.
- The acid type affected the amount of dissolved Nb and Ti. The amount of dissolved Nb was slightly larger for the high concentrated sulfuric acid than for the hydrochloric acid. The amount of dissolved Ti found in the supernatant was higher for both sulfuric acid etchants than for the hydrochloric acid, however, the differences in the amounts found in the supernatant are larger then the differences in the amounts found in the residue. This indicates that the acid type does affect particle etching only to a lower extent. Other measurements, e.g. comparison between tempered and regular steel (see below), support this finding.
- The temperature showed to influence particle etching regardless of the chemical composition. In perspective to particle etching, a low extraction temperature is therefore favourable.

The different amounts of Nb and Ti in the supernatant and residue cannot be explained by Ti and Nb dissolved in the steel matrix and strongly suggest that the carbonitride particles are attacked at different rates.

I performed further experiments to verify particle etching by the different etchants and to check whether all alloyed Ti and Nb were fully precipitated. The sample analyzed in the last section was tempered and I examined the sample for differences in the Ti and Nb content in the supernatant after matrix dissolution compared to the regular sample. Additionally, I synthesized NbCN and TiCN reference particles and studied their time dependent dissolution behavior in different etchants.

Tempered vs. regular steel

Additional tempering of the X100 steel sample is used to guarantee that all Ti and Nb is precipitated as carbonitrides. The sample was tempered at 600 °C for 3 h. The tempered and regular sample were dissolved using 4 mol/L HCl at 60 °C for the first 3 h and 40 °C for the next 13 h. When dissolution was complete, 75 mL of UPW was added to the particle suspensions and the suspensions were centrifuged. In order to additionally investigate the influence of the centrifugation time on the content of Nb and Ti in the supernatant, the sample was divided and the aliquots were centrifuged for different times at 113 000 rcf.

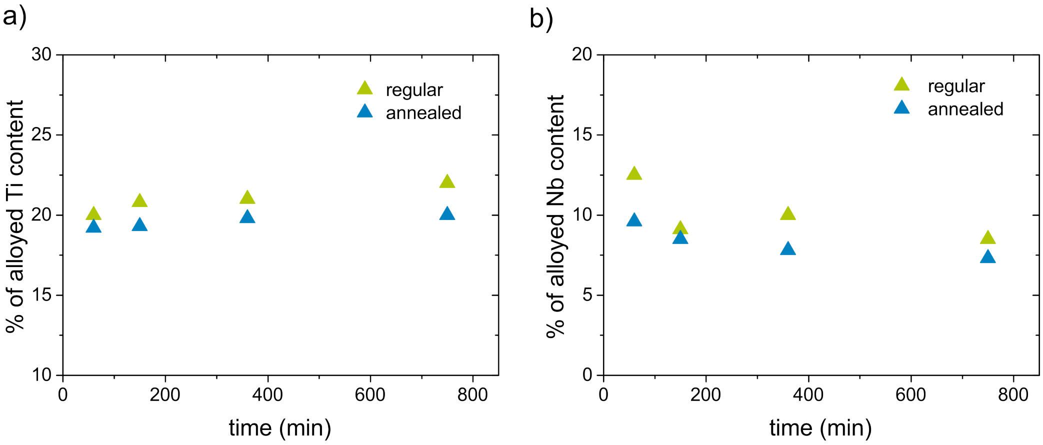

Figure 2.2: Time dependent dissolution of the extracted a) titanium and b) niobium carbonitride particles for a tempered (blue) and regular steel (green).

Figure 2.2 shows the quantities of dissolved Ti and Nb in the supernatant after 1.5, 3, 6 and 18 h. The amount of Nb was higher for short centrifugation times. This suggest that small particles are in the supernatant and sediment only after an extended time. The amount of Ti found in the supernatant did not depend on the centrifugation time and was approximately constant for all times. It increased by 1 wt.%, indicating ongoing etching of the particles during centrifugation.

The amounts of dissolved Nb and Ti found in the supernatant for the tempered and regular steel differed only slightly (max. 1 wt.% for Ti and 3 wt.% for Nb). Almost all microalloy elements had already precipitated in the regular steel; the Nb and Ti found in the supernatant comes from dissolved particles.

2.2.2 Reference particles

Reference particles were used to study the unwanted etching of TiCN and NbCN particles without the influence of the iron matrix. Pure NbCN and TiCN particles without any oxide impurities were sythesized according to Giordano et al. [76]. Figure 2.3 a and b show the XRD diffractrogram and a TEM micrograph for TiCN and Figure 2.3 c and d show the XRD diffractogram and a TEM micrograph for the NbCN, respectively.

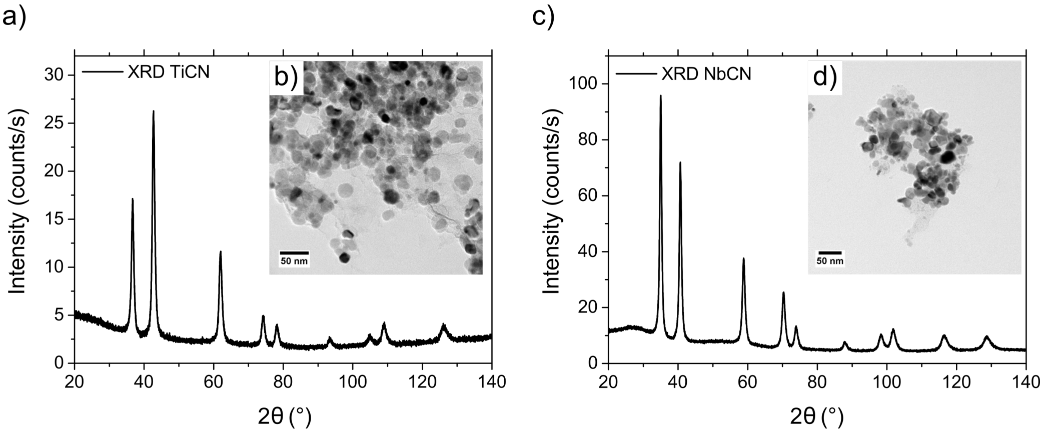

Figure 2.3: Reference particles synthesized according to Giordano et al. [76] a) XRD diffractogram and b) corresponding TEM micrograph of TiCN reference particles. c) XRD diffractorgram and d) corresponding TEM micrograph of NbCN particles.

Reference particles at the amount to TiCN and NbCN particles contained in 1 g of the X100 steel were analyzed. An amount of 0.23 mg TiCN or 0.55 mg NbCN reference particles was treated in analogy to ASTM E 194-10 and placed in a glass beaker with 20 mL HCl at 6 mol/L. Samples of 0.5 mL were taken after 1 h, 2 h, 4 h, 8 h, and 24 h, placed in a centrifugal filter (10 kDa, Pall), and centrifuged (Centrifuge 5418, Eppendorf, Germany) at 16 873 rcf for 10 min. The particle-free liquid was then analyzed for dissolved elements using ICP-OES. After 24 h, the particle dispersion was heated to boil as per ASTM protocol, 30 mL of UPW were added, and the mixture was again heated to boil. A final sample was taken and treated as above. The same amounts of reference particles were also subjected to the modified dissolution protocols. Particles were added to the acid mixture in question and sonicated for 1 min. The dispersions were placed in an oil bath and heated under reflux while stirring at 200 rpm. Samples of 0.5 mL were taken after 1 h, 2 h, 4 h, 8 h, and 24 h, centrifuged, and analyzed as above.

The results clearly indicated particle etching for all protocols. Figure 2.4 shows the release of dissolved Ti and Nb from Ti or Nb carbonitride reference particles as the ratio of Ti or Nb found in the supernatant to the total amount of Ti or Nb contained in the added particles.

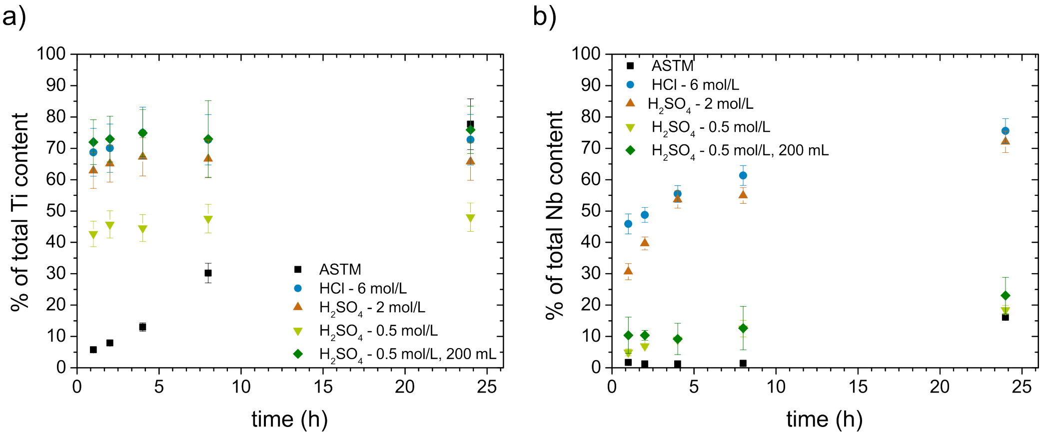

Figure 2.4: Dissolution of a) titanium and b) niobium reference particles in different etching solutions.

The etching of TiCN particles in the ASTM protocol was steady but particularly severe during the boiling step after 24 h, where up to 77 wt.% of the particles were dissolved. Modified protocols with dissolution at an increased temperature of 70 °C led similar trends: strong etching in the first hour, then saturation at Ti levels at or below those found for ASTM. Increasing the acid volume increased Ti loss.

The etching of NbCN particles strongly depended on the etching solution. The loss of Nb during the ASTM protocol was minor before boiling and reached 16 wt.% after its completion. All other etchants caused greater losses and some of them were prohibitive: 6 mol/L HCl dissolved 76 wt.% after a rapid initial phase and a slow but steady etching; the trend was similar for 2 mol/L H_2SO_4 at a somewhat lower loss level that reached 72 wt.%. More useful was 0.5 mol/L H_2SO_4 with 18 wt.% loss. The volume of etchant had little effect on the total particle loss.

2.2.3 Particle loss mechanisms

The results clearly indicate unwanted etching of particles in all extraction protocols. Even optimized protocols caused losses of at least 6 wt.% of Nb and 9 wt.% of Ti that need to be considered in the interpretation of the results.

There are several reasons to exclude the alternative explanation that Ti or Nb were dissolved from solid solution in the steel. First, the steel samples used here were treated with a temperature ramp during TMCP that is likely to cause complete or almost complete precipitation of Ti and Nb as carbonitrides within the errors of the available thermodynamic data, so that the amount of Nb and Ti remaining as solid solution must be small. In addition, we found that the amount of dissolved Ti and Nb for the same steel strongly depended on the acid type and etchant volume, even though all iron was dissolved in all cases: HCl led to lower concentrations than H_2SO_4, and larger etchant volumes strongly increased the concentration for both elements. The amount of dissolved Nb additionally depended on temperature and acid concentration that are very unlikely to affect the removal from solid solution. Dissolution of a tempered steel, where possible microalloy elements remaining in solid solution are enforced to precipitate, supported these findings.

Experiments with reference particles support this interpretation, too. Higher acid concentrations, higher temperatures, and higher etchant volumes led to increased particle etching. Interestingly, the experiments indicate that Ti and Nb concentrations in the supernatant rapidly increased in the first hours of the experiments and then reached saturation. Note that the reference particles experience a “worst case scenario” were all the acid only attacks the reference particles during the entire experiment, while acid is consumed in iron dissolution in the real extraction and the losses from particles in steels are expected (and found) to be somewhat smaller.

The processes during extraction are complex and there are several mechanisms that will require further studies until their role is fully understood. For example, the amount of Ti in the supernatant after 6 mol/L HCl extraction at 70 °C was surprisingly low. It was never possible to recover all Ti and Nb from the combined supernatant and residue, probably due to particle losses during the centrifugation process through adsorption on the walls of the centrifuge tubes. The smallest particles in steel have sizes of only a few nanometers and may well remain in the supernatant, where they are found by elementary analysis and indicate more extensive etching that actually took place.

SiO_x network formation may reduce particle dissolution by engulfing the particles, separating them from the acid, and protecting them from dissolution. On the other hand, even very small particles trapped in the SiO_x network sediment rather rapidly (a process that is exploited in commercial water purification with iron hydroxide networks, for example [77]), which may remove them from the supernatant and explain the good extraction yields of the ASTM protocol despite of its considerable etching. Finally, one would not expect that the particles are uniformly etched independent on their size; smaller particles may be etched faster than large particles. If very small particles with sizes ($< 10\,\mathrm{nm}$) are rapidly etched, the measured PSD of the extracted particles may be shifted towards larger sizes.

2.3 Silica network

Microalloyed steel typically contain 0.2 to 0.4 wt.% silicon, which stabilizes the ferrite phase and increases strength by solid solution strengthening. During extraction, Si tends to form a SiO_x network. This network encloses the particles and makes it difficult or impossible to analyze them.[58]

2.3.1 Silica network formation for different extraction protocols

In order to investigate the influence of the extraction protocols on SiO_x network formation, I measured the Si content in the supernatant after the first centrifugation run and in the residue. The silicon distribution strongly depended on the extraction protocol (Figure 2.5).

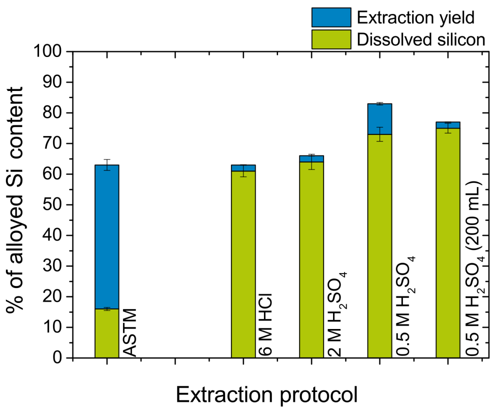

Figure 2.5: Silicon content in the supernatant (green) and in the extraction yield (blue) for different extraction procedures referred to the total content of alloyed silicon.

While the ASTM dissolution protocol resulted in a silicon content of 15 wt.% in the supernatant and 47 wt.% in the residue, extraction at higher temperature generally led to much more silicon in the supernatant and less in the residue. For dissolution with 6 mol/L HCl the quantity of Si in the supernatant was 61 wt.% and in the residue 2 wt.%. Dissolution with H_2SO_4 resulted in similar amounts for both supernatant and extraction residue.

Figure 2.6 shows TEM micrographs and EDX spectra of the particles extracted with different protocols. ASTM extraction caused severe SiO_x network formation and particle analysis was impossible (Figure 2.6 a). Extraction with 6 mol/L HCl (Figure 2.6 c) and 2 mol/L H_2SO_4 (Figure 2.6 e) at 70 °C showed drastically decreased SiO_x formation and large particles were clearly visible. Smaller particles were still trapped in the SiO_x network. Extraction with 0.5 mol/L H_2SO_4 indicated an increased SiO_x network compared to higher concentrated acids, but still improved compared to ASTM (Figure 2.6 g).

EDX analysis of the extracted particles (Figure 2.6 b, d, f, and h) confirmed that the Si content in the residues decreased for the modified protocols and the particles extracted exclusively contained Nb and Ti carbides, nitrides, and carbonitrides. There may be traces of V present, but the K_β-line of Ti is close to the K_α-line of V, the K_β-line of V is close to the K_α-line of Cr, and the overall peak is small. The TEM sample holder contains Cr, which is commonly found in traces, and thus no unambiguous statement is possible. Copper is likely from the TEM grid and the traces of Fe in the residue are

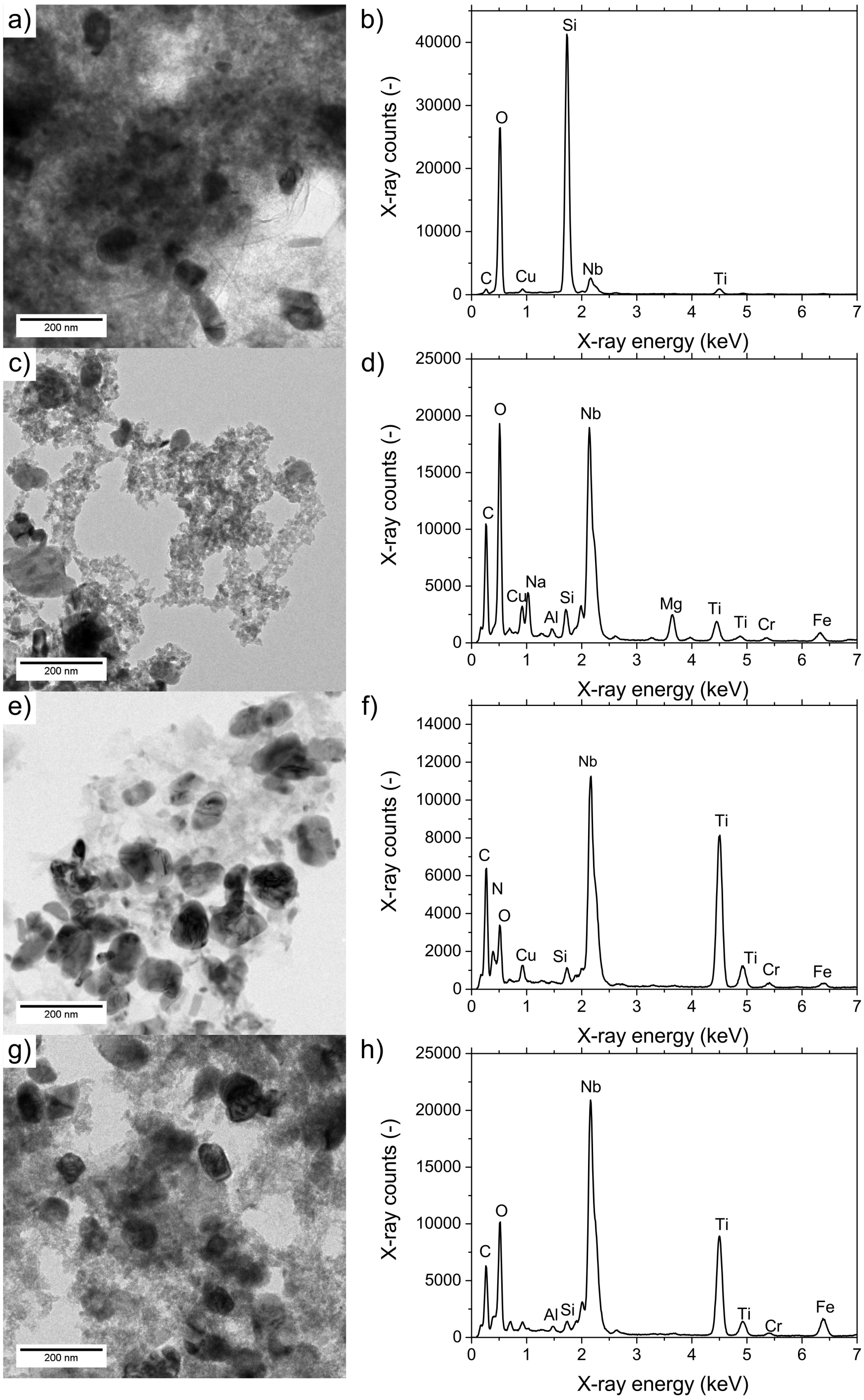

Figure 2.6: TEM micrographs of the extracted particles after extraction with the different protocols and the according EDX spectra: a) ASTM standard. b) EDX spectrum of a). c) 6 mol/L HCl. d) EDX spectrum of c). e) 2 mol/L H_2SO_4. f) EDX spectrum of e). g) 0.5 mol/L H_2SO_4. h) EDX spectrum of g).

probably due to incomplete removal of the dissolved matrix. Carbon was ubiquitous and may originate from the particles or the amorphous carbon coating of the TEM grids.

The quantification of the Si content (Figure 2.5) in the supernatant (where it can be removed) and in the residue (where it forms networks) coincides well with the TEM micrographs in Figure 2.6. SiO_x formation is probably affected by the extraction time. Extraction according to ASTM required 3 days for complete steel sample dissolution, providing sufficient time for denser network formation. The modified extraction protocols were much faster and the amount of Si was much higher in the supernatant and lower in the residue, respectively. Among the modified extraction protocols, particle extraction with 0.5 mol/L H_2SO_4 lasted the longest and revealed the most SiO_x network.

Besides the extraction time, the etchant volume and thus the concentration of Si in the etchant during extraction is important. The SiO_x network formation is lower for lower Si concentrations.

Not all silicon contained in the dissolved steels was found in the combined supernatant and residue; to a large degree probably due to adsorption of SiO_x at the walls of glass containers. Teflon reduces this loss, but is not recommended because niobium and titanium carbonitride particles readily adsorb on Teflon.

2.3.2 Removal and prevention of silica networks

A particle suspension free of silica network can be obtained by a post-treatment of the extracted particles and dissolving the silica network with chemical etchants. Another possiblity is to actively prevent SiO_x precipitation using additives.

Chemical dissolution of silica

Silica network exacerbates particle analysis or makes it even impossible. Lu et al.[58] therefore suggested to dissolve the formed SiO_x by treating the extraction residue with HF.

I investigated the effect of HF on SiO_x content and particle etching. A steel sample was dissolved in 2 mol/L HCl, centrifuged and the remaining volume (9.5 mL) was treated with 0.5 mL HF 1 wt.%. After 30 min, the sample was centrifuged 5 times in order to remove HF and dissolved silica. TEM showed successful removal of the silica network (see Figure 2.7 a).

In order to study the influence of HF on the precipitates, I dissolved a steel sample with 4 mol/L HCl in a similar experiment. After dissolution, I diluted the sample by adding 75 mL of UPW and removed the dissolved iron by centrifugation. After 12 centrifugation cycles, the supernatant was removed (15 mL) and 0.5 mL HF 1 wt.% was added to the remaining particle suspension (10 mL). After 135 min, the suspension was filled up with UPW to 25 mL and centrifuged for 12.5 h. After centrifugation, the supernatant was analyzed by means of ICP-OES to study the amount of dissolved Nb and Ti. 45 wt.% of Nb and 1 wt.% of Ti of the total alloyed content were found in the supernatant. Dissolution experiments of reference particles in HF 0.1 wt.% confirmed severe etching of NbCN particles. In contrast to the particles extracted from steel, the synthesized reference particles indicated also severe particle attack of TiCN based particles as shown in Figure 2.7 b and c.

Another possibility to dissolve SiO_x is sodium hydroxide. At high pH (pH $>$ 10.5), SiO_2 is more soluble by orders of magnitude.[78] Experiments showed promising preliminary results at sufficient high pH values of 11 or higher. Titanium and niobium carbonitride reference particles were tested for their stability in different concentrated sodium hydroxide solutions (Figure 2.7 b and c).

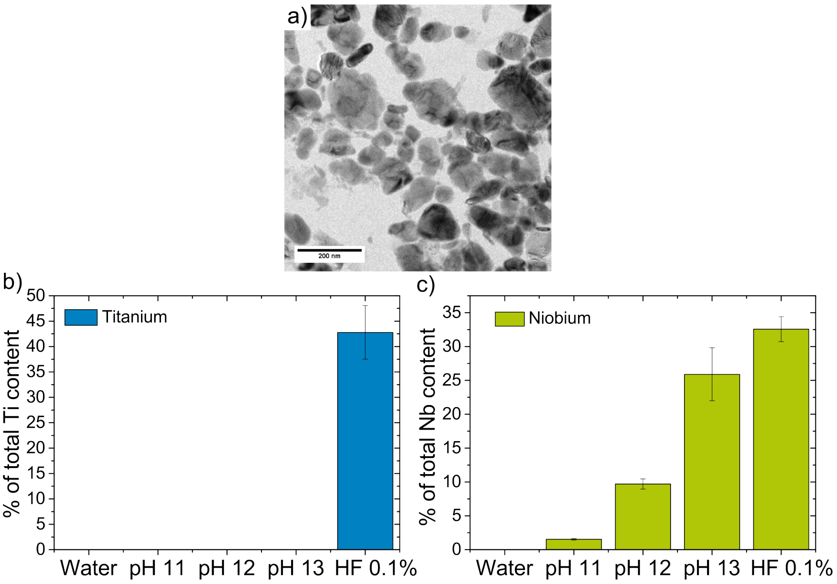

Figure 2.7: Removing of SiO_x network by post-treatment with chemical etchants: a) TEM micrograph of extracted particles after HF treatment. The silica network was removed. Amount of total b) titanium and c) niobium in the supernatant of reference particles treated with HF and different concentrated NaOH solutions.

Niobium was heavily attacked and almost 50 wt.% of the alloyed Nb was dissolved after HF treatment. The measurements on the reference particles confirmed this finding. But, TiCN reference particles showed a severe attack, too, contrary to HF treatment of the extracted particles, where almost no Ti was found in the supernatant. While reference particles were mainly small, TiCN particles in steel tend to be large in size and often have a NbCN shell. This reduces the attack of Ti containing particles.

TiCN particles showed good resistance against NaOH at all tested pH values, while NbCN particles were readily attacked with increasing pH value. Sodium hydroxide treatment of the residue can only be performed when the dissolved iron is almost completely removed. Traces of iron immediately form $Fe(OH)_3$ that precipitates and impedes the analysis of the targeted particles.

Silica precipitation inhibition

The solubility of SiO_x in water depends on the phase of the formed SiO_x, pH, temperature, and the presence of cations. The solubility of amorphous silica in water at 25 °C is between 100 to 200 ppm at pH between 1 and 9.[78] This is equivalent to the concentration range of Si in the modified extraction solutions (< 200 ppm). Small amounts of polyvalent metallic cations drastically reduce the solubility of SiO_x.[78] The solubility of SiO_x is therefore expected to be very low during extraction where Fe^{3+} and Al^{3+} (alloy element) form. Thus, my approach was either to keep Si in solution by complexing Si or to prevent SiO_x precipitation by complexing metallic cations. Both approaches are known procedures for silica formation inhibition.[79, 80]

I added disodium ethylenediaminetetraacetate (disodium EDTA), tannic acid, and boric acid in different combinations to the protocols for particle etching (see section 2.2) and replaced H_2SO_4 by oxalic acid. Tannic acid and boric acid were added in order to form complexes with Si, while EDTA and oxalic acid were supposed to form stable complexes with iron and aluminum ions. Addition of tannic acid and boric acid and sample dissolution using oxalic acid did not have any positive effect on the extraction result and partially even aggravated silica precipitation. EDTA did not reduce the formation of silica either, but it changed the morphology of the silica.

The additives tested here help to inhibit silica formation in cooling water circles, but the conditions there are significantly less harsh than in the extraction solution. The extraction solution is very acidic ($pH < 0$), and the amount of polyvalent metalic cations is enormous. I conclude that these conditions make a successful application of the additives not possible.

2.3.3 Strategies for silica-free particle suspensions

The formation of silica networks depended on the dissolution rate and the concentration of silicon in the etchant solution. Higher temperatures and higher acid concentrations led to faster dissolution and a reduced amount of silica in the extraction residue. A larger volume of the etching solution led to less Si in solution, which also limited the formation of silica network. Thus, protocols with the highest possible dissolution rates and large etchants volumes are favourable.

Dissolution of the silica matrix with HF led to losses of both Nb and Ti carbonitrides particles. Dissolution with NaOH only attacked Nb based precipitates; Ti carbonitrides were protected, but complete removal of the dissolved iron is required to prevent precipitation of $Fe(OH)_3$. This would significantly increase the time required for sample preparation.

2.4 Prevention of particle agglomeration

Colloidal particle analysis requires an extraction protocol that provides unagglomerated particles. Particle agglomeration is commonly induced by the high ionic strength due to the high Fe concentration and the low pH. Addition of a dispersant to stabilize the individual particles proved to be a noble solution.

Polyethylene glycol (M = 1 kDa)(PEG-1000), polyethylene glycol (M = 20 kDa)(PEG-20000), polystyrene sulfonate (PSS), and the commercial available dispersants *Disperbyk-2012* and *Disperbyk-2015* from BYK additives and instruments are all surfactants tested for particle extraction. Both TEM and ICP-OES indicated that Disperbyk-2012 provided well distributed particles and reduced SiO_x formation. Figure 2.8 shows TEM micrographs of particles extracted with 0.5 mol/L H_2SO_4 with 0.1 vol.% Disperbyk-2012. The addition of Disperbyk-2012 suppressed SiO_x formation almost completely. The surfactant caused shadows in the TEM micrograph (Figure 2.8 a) and coated the particles (Figure 2.8 b). The other tested surfactants did not have a positive effect on agglomeration or SiO_x suppression.

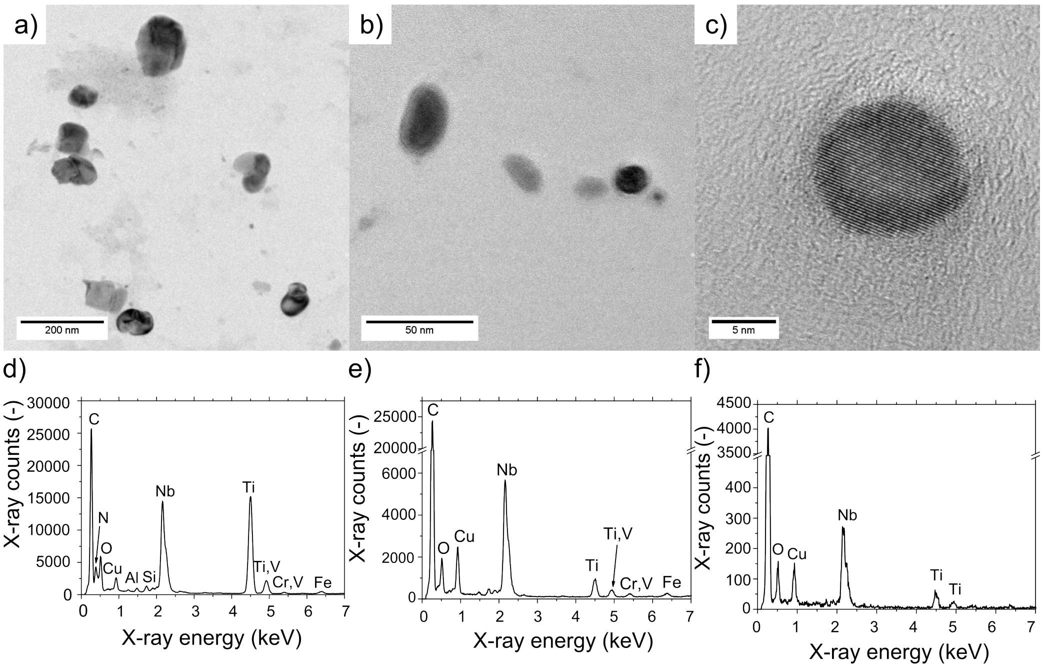

Figure 2.8: Transmission electron microscopy of particles extracted with 0.5 mol/L H_2SO_4 and 0.1 vol.% Disperbyk-2012: a) Overview. b) Detailed view of smaller particles. Particles are coated with the surfactant. c) High resolution micrograph of a small particle. d) EDX spectrum of particles in a). e) EDX spectrum of particles in b). f) EDX spectrum of the particle in c). Small particles mainly consists of Nb with small amounts of Ti.

Surfactant addition not only affected SiO_x network formation, but also particle etching and the extraction yield. The supernatants after the first centrifugation run and the residue after 8 centrifugation cycles were analyzed with regard to their Nb, Ti, and Si content referred to the total alloyed content of Nb, Ti, and Si (Figure 2.9).

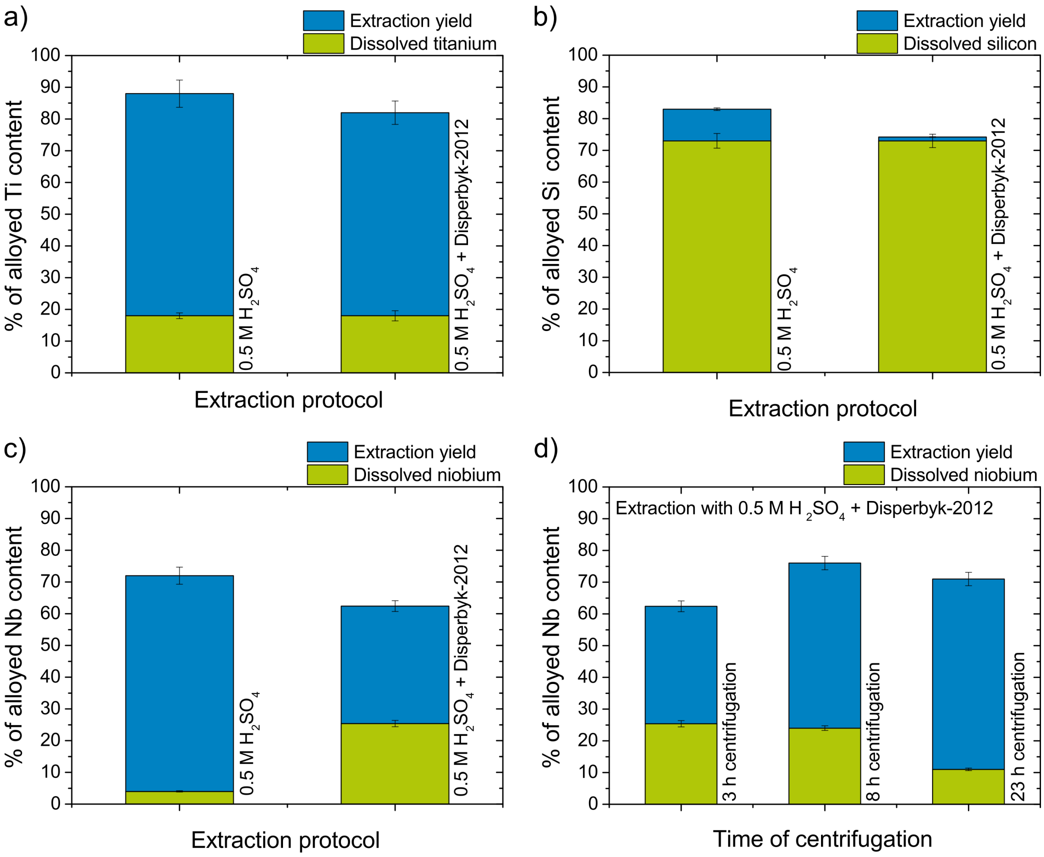

Figure 2.9: Amount of a) titanium, b) silicon, and c) niobium in the supernatant (green) and the residue (blue) after particle extraction with 0.5 mol/L H_2SO_4 and 0.5 mol/L H_2SO_4 with 0.1 vol.% Disperbyk-2012. d) Influence of different centrifugation times on the niobium content in the supernatant and extraction residue after particle extraction with 0.5 mol/L H_2SO_4 with 0.1 vol.% Disperbyk-2012.

The dissolution rate of Ti based particles was not affected by the surfactant addition and the amount of Ti found in the supernatant and residue remained unchanged. The quantity of Nb found in the supernatant was increased to 25 wt.% and the extraction yield decreased to 37 wt.%. As expected from TEM, the extraction yield of Si decreased to 1 wt.% (Figure 2.9 b).

Longer centrifugation times affected the amount of Nb and Si in the supernatant and residue, but not Ti. Increasing the centrifugation time from 3 to 8 h marginally decreased the dissolved Nb, but the Nb in the residue increased to 53 wt.%. Further increase of the centrifugation time to 23 h decreased the amount of Nb in the supernatant to 11 wt.% and increased the extraction yield to 60 wt.%. The quantity of silicon in the supernatant remained unchanged by increasing the centrifugation time to 8 h, but decreased to 30 wt.% when increasing the centrifugation time to 23 h. The extraction yield for Si slightly increased for longer centrifugation times.

Due to the increased amount of Nb in the supernatant after introduction of the supernatant, I investigated the influence of the dispersant on particle etching more closely and conducted dissolution experiments with reference particles in analogy to previous experiments on reference particles. The etching solution was 0.5 mol/L H_2SO_4 with 0.1 vol.% Disperbyk-2012. Figure 2.10 illustrates the quantity of dissolved Nb and Ti in the supernatant. Adding a dispersant helped to reduce etching of both Nb and Ti carbonitride particles, particularly in the first hours of the dissolution experiment. The amount of dissolved particles converged towards long experiment times (24 h).

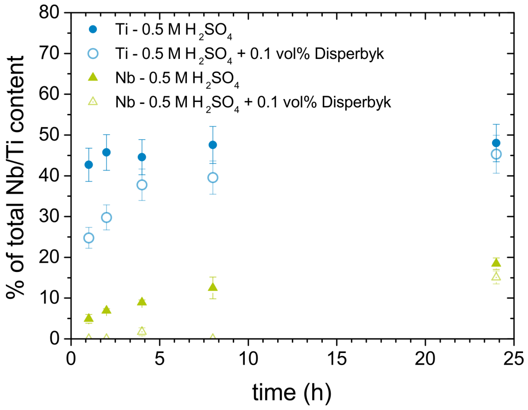

Figure 2.10: Dissolved NbCN and TiCN reference particles in the supernatant after treatment with 0.5 mol/L H_2SO_4 with (empty symbols) and without 0.1 vol.% Disperbyk-2012 (filled symbols).

I am not aware of any reported protocols for particle extraction with surfactants and performed extensive tests that led to markedly improved extraction results, with reduced agglomeration and silicon oxide network formation compared to the surfactant-free etchants. Experiments with reference particles indicated some protection of the particles from etching. The commercial dispersant used during the experiments is based on block copolymers with groups designed to bind to the particle surfaces, thus forming a polymer shell that protects individual particles and stabilizes dispersion. The shell increased the hydrodynamic diameter, which needs to be considered for colloidal analysis, but it is readily penetrated by electrons and aids electron microscopy by spacing particles.

The reduction in SiO_x network formation is probably due to the stabilization of the SiO_x sol that does not gel when stabilized by the dispersant. It is conceivable that the surfactant also slows down growth and leads to smaller SiO_x particles that are easily removed with the supernatant because of their small size and low density.

A surprising result is the increased content of Nb in the supernatant when introducing a surfactant. Part of this increase is most likely due to very small particles (with diameters in the single-nanometer range) that are stabilized by the surfactant, remain in the supernatant, and do not sediment during centrifugation. Such small particles have rarely been addressed in extraction so far. Prolonging the centrifugation time increased recovery, but the amount of Nb in the supernatant after particle extraction without dispersant was still not reached. Dissolved Nb may enter the SiO_x network that is partially formed during extraction without dispersant. This could lower the amount of Nb found in the supernatant.

Titanium concentrations in the supernatant were much less affected by the dispersant. Most particles containing Ti particles are large ($> 50\,\mathrm{nm}$) and easily sediment during centrifugation.

2.5 Optimized extraction protocol

There exist trade-offs between particle loss by unwanted etching, the rate of dissolution of the steel sample, and the degree of SiO_x network formation. Higher temperatures and higher acid concentrations sped up extraction and lowered SiO_x formation, but increased particle etching. Even the best protocols caused a considerable loss from particles. This can cause a reduction of the true particle diameter[4] on the order of 5% that should be reported when using such methods.

The best extraction protocol was 0.5 mol/L H_2SO_4 with 0.1 vol.% Disperbyk-2012 at an extraction temperature of 70 °C. It reduced particle etching to 11 wt.% for Nb and 18 wt.% for Ti. Long centrifugation times above 20 h are recommended (at the given rcf) to remove most of the smallest particles from the suspension.

The surfactant Disperbyk-2012 improved extraction by stabilizing the particles and suppressing SiO_x formation without decreasing the extraction yield. There are indications that the surfactant stabilizes even particles with diameters below 10 nm making them accessible to characterization techniques beyond electron microscopy. Other tested additives did not have a positive

---

[4] $V \sim r^3$: a reduction of 15% in volume/mass goes along with a reduction of approx. 5% in radius.

influence either on SiO_x network formation or on particle stabilization.

The developed extraction protocol provides a particle suspension that contains unagglomerated particles suitable for analysis by means of colloidal methods or electron microscopy. In the next chapter, colloidal analysis methods are investigated that are suitable to analyze such broad multimodally distributed particle systems.

Chapter 3

Colloidal particle analysis

A *colloidal system* or *colloidal dispersion* is a heterogeneous solid, liquid, or gas consisting of particles (dispersed phase) in a continuous medium (dispersion medium). The physical and chemical properties of such systems are subjects of colloidal chemistry.[81, 82] Here, we concentrate on solid particles with diameters between 1 and 1000 nm, the size range of microalloy carbonitride particles in microalloyed steels.

Small solid particles may not be directly visible to the human eye. Conventional light microscopy is only able to resolve particles with sizes of approximately 200 nm; high-resolution electron microscopy can visualize much smaller particles. However, TEM is expensive, time-consuming, and it allows only a small number of particles to be analyzed.[83] Some applications require the rapid determination of the size of a large number of particles.[81, 83] Here, I consider colloidal characterization techniques that provide information on the size and composition of colloidal particles in their native state and studied how they can be applied to better characterize microalloy carbonitride particles.

3.1 Statistical description of the particle size distribution

The diameters of individual particles are rarely identical. Their distribution is described by the particle size distribution (PSD). The cumulative distribution $Q(x)$

$$Q(x) = \frac{\text{amount of particles in } x_{min}...x}{\text{total amount of particles } x_{min}...x_{max}} \tag{3.1}$$

describes the amount of particles with a diameter below or equal to the particle diameter x. For particles with diameters $x < x_{min}$, $Q = 0$; for particles with sizes $x \geq x_{max}$, $Q = 1$.

The cumulative distribution can be converted into the density distribution $q(x)$ ("frequency distribution function") by dividing the size of fraction i by an interval width Δx_i:

$$q(x_i) = \frac{Q(x_i) - Q(x_{i-1})}{\Delta x_i} = \frac{\Delta Q_i}{\Delta x_i} \tag{3.2}$$

This quantity describes the relative amount of the particle size fraction i. If the cumulative distribution is continuously differentiable, $q(x)$ is the first derivative of the cumulative distribution. It is therefore also called differential distribution:

$$q(x) = \frac{dQ}{dx} \tag{3.3}$$

Important properties of the PSD include [84] the

- *arithmetic mean*, equal to the expectation value of the size distribution:

$$x_{\text{mean}} = \int_{-\infty}^{\infty} x q(x) dx \tag{3.4}$$

- *standard deviation*, a measure for the scattering of the particle sizes around the mean value, i.e. the width of the particle size distribution:

$$\sigma = \sqrt{\int_{-\infty}^{\infty} (x - x_{\text{mean}})^2 q(x) dx} \tag{3.5}$$

- *modal value(s)*, maxima of a density distribution: (locally) most frequent particle size(s). A *monomodal* size distribution has only one "global" maximum. The modal value represents the most frequent particle size of the entire particle size distribution. If the size distribution has more than one local maximum, it is called *multimodal.*

- *median*, the center of a distribution. It separates the particles into two equally sized parts:

$$\int_{-\infty}^{x_{\text{median}}} q(x) dx = 0.5 \text{ or } \int_{x_{\text{median}}}^{\infty} q(x) dx = 0.5 \tag{3.6}$$

- *percentile*, size below which a certain percentage of particles is found. The percentile x_{10} describes the particle size below which 10% of the particles are found in the particle size distribution. Thus, 90% of the particles have larger sizes than the x_{10} value. Most common are the x_{10}, x_{50} (x_{median}), and x_{90}.

Figure 3.1 illustrates a cumulative distribution and the corresponding density distribution. The cumulative curve direclty shows median (x_{50}), x_{10} and x_{90}. The differential representation often emphasizes multimodal distributions or shoulders, and it makes the modal (most common) particle size immediately visible.[85]

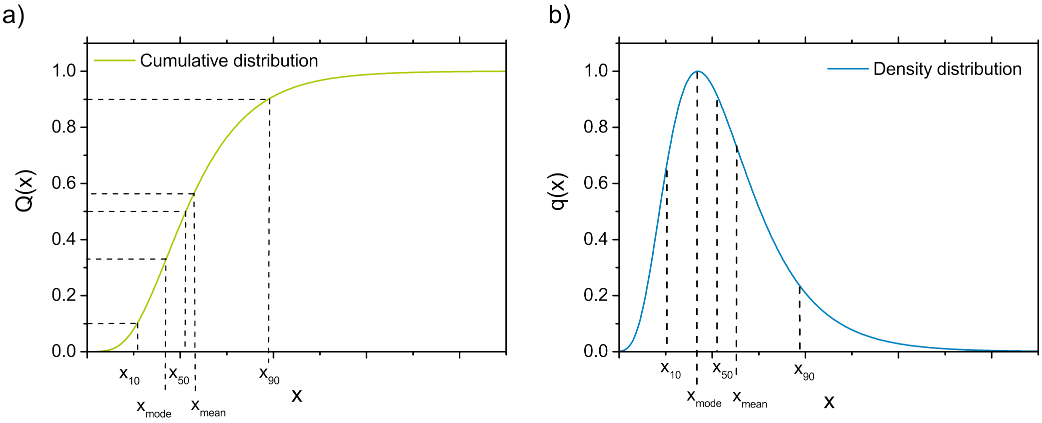

Figure 3.1: Sizes of colloidal particles expressed by their a) cumulative distribution function $Q(x)$ and b) density distribution function $q(x)$.

Colloidal sizing techniques often measure the distribution of a secondary particle property $q(\xi)$ that is related to the particle size x by a function $x = f(\xi)$ and convert it into $q(x)$. If the particle property ξ is transformed into the particle size x, the frequency distribution of the measured particle property $q(\xi)$ must be transformed into the size frequency distribution $q(x)$:

$$q(x) = q(\xi)\frac{d\xi}{dx} \tag{3.7}$$

All sizing methods provide a particle size that is derived from a physical property. The size is usually stated as the equivalent sphere diameter (ESD); the diameter of a sphere that has the same property as the analyzed particle.[85] The particle size distribution is weighted according to the measured quantity (e.g. number, volume, scattering intensity etc.) that is the basis of the measuring method. Counting analysis of TEM micrographs, for example, provides number-weighted distributions (q_0). Analytic methods that are based on the particle volume, for example laser diffraction, provide volume-weighted distributions (q_3). The abundance of a particle with the diameter

x then scales with x^3 ($V \sim x^3$), so that larger particles are more heavily weighted then in the corresponding number-weighted distribution.[83, 85] Thus, knowledge of the weighting is essential. Particle size distributions with different weightings can only be compared after transformation.[85] If there is a simple relation between the measured quantity and the particle diameter (like in the sample above), the PSD weighted with x^r is converted into a PSD weighted with x^s [81] by

$$q_s(x) = \frac{x^{s-r} q_r(x)}{\int_{x_{min}}^{x_{max}} x^{s-r} q_r(x) dx} \tag{3.8}$$

However, there are properties such as optical extinction, where the particle diameter contributes in several powers (absorption contribution $\sim x^3$ and scattering contribution $\sim x^6$) to the relation. Particle size distributions weighted with such properties cannot be transformed using equation (3.8) and require individual formula.

Uncertainties in the PSD, for example caused by low signals from small particles or noise, can be strongly amplified during transformation. The transformation of a volume-weighted distribution into a number-weighted distribution strongly magnifies smaller particle fractions, and it is important to note that the error will increase alongside and may render the representation misleading.[85]

3.2 Particle characterization techniques

Sizing methods can be grouped into counting methods, fractionating methods, and ensemble methods. Counting methods measure the size of each individual particle. Fractionating methods separate the particles in different size fractions and measure the mean size of the particles in each fraction. Ensemble techniques determine the particle size distribution by analyzing all particles simultaneously.[83, 86]

3.2.1 Dynamic light scattering

Dynamic light scattering (DLS), also known as photon correlation spectroscopy (PCS), is a widely used sizing technique that relies on the Brownian motion of the particles.

Theory

The sample is illuminated with monochromatic light. Light scattered under a certain angle (often 90°) is electronically detected. Brownian motion of the particles causes fluctuations in the scattered light intensity. The autocorrelation of the time-dependent intensity $I(t)$ leads to [87]

$$g^{(2)}(\tau) = \frac{\Big\langle I(t) \cdot I(t+\tau) \Big\rangle}{\Big\langle I(t) \Big\rangle^2} \tag{3.9}$$

with the delay time τ. The intensity correlation function $g^{(2)}(\tau)$ (second-order correlation function) is related to the correlation function of the electric field (first-order correlation function) $g^{(1)}(\tau)$ by the Siegert-relation[1] [88]

$$g^{(1)}(\tau) = \sqrt{\beta \cdot g^{(2)}(\tau) - B} \tag{3.10}$$

with the baseline $B \approx 1$ and the coherence factor β that depends on detector area, optical alignment, and scattering properties of the sample.[87]

An ideal monomodal particle suspension in DLS causes an autocorrelation with an exponential decay [89]:

$$g^{(1)}(\tau) = A \cdot e^{-\Gamma\tau} + B \tag{3.11}$$

with the amplitude of the correlation function A, the baseline B, and the decay rate Γ. The decay rate Γ is related to the diffusion coefficient D:

$$\Gamma = Dq^2 \tag{3.12}$$

with the wave vector q defined as

$$q = \frac{4\pi n}{\lambda} \sin\left(\frac{\theta}{2}\right) \tag{3.13}$$

and the refractive index of the medium n, the optical wavelength λ, and the scattering angle θ.[89]

The diffusion coefficient is linked to the diameter of non-interacting spherical particles by the Einstein-Smoluchowski (or Stokes-Einstein) equation:

$$D = \frac{k_\mathrm{B} T}{3\pi\eta_\mathrm{s} x_\mathrm{h}} \tag{3.14}$$

with Boltzmann's constant k_B, the temperature T, the shear viscosity of the solvent η_s, and the hydrodynamic diameter x_h.[89]

---

[1] The Siegert-relation is only valid for homodyne DLS (self-beating mode), that was exclusively used in this thesis.

Particles are rarely perfectly monomodal and usually have a finite size distribution. The scattering signal of such systems deviates and can be described as the sum of exponential decays weighted by their amplitudes:

$$g^1(\tau) = \sum_{i=1}^{n} G_i(\Gamma_i) e^{-\Gamma_i \tau} + B = \int G(\Gamma) e^{-\Gamma\tau} d\Gamma + B \tag{3.15}$$

The distribution G(Γ) is the distribution of decay rates Γ weighted with their relative scattering intensity. It depends on the size and the volume fraction of the particles.

Different data analysis methods are available to extract the diffusion coefficient distribution and hence the particle size distribution of the sample. In the following, I will discuss the two most common methods, the cumulant and the non-negatively constrained least-squares analysis [89]:

Methods of cumulants

The method of cumulants is recommended by the international standard ISO 13321 and is applicable solely to narrow monomodal distributions. Expansion of equation (3.15) by the mean the decay rate $\bar{\Gamma}$ leads to

$$g^1(\tau) = \int G(\Gamma) e^{-\bar{\Gamma}\tau} e^{-(\Gamma-\bar{\Gamma})\tau} d\Gamma + B \tag{3.16}$$

with

$$\bar{\Gamma} = \int \Gamma G(\Gamma) d\Gamma \tag{3.17}$$

Writing the second exponential term in equation 3.16 in a series of expansions and neglecting higher term orders leads to

$$g^1(\tau) = e^{-\bar{\Gamma}\tau}\Big(1 + \frac{\mu_2 \tau^2}{2}\Big) + B \tag{3.18}$$

with μ_2 the variance of the distribution $G(\Gamma)$. Equation (3.18) can be simplified for $\mu_2\tau^2 \ll 1$:

$$g^1(\tau) = e^{-\bar{\Gamma}\tau + \frac{\mu_2\tau^2}{2}} + B \tag{3.19}$$

Taking the natural logarithm of equation (3.19) leads to

$$\ln(g^1(\tau)) = \ln B - \bar{\Gamma}\tau + \frac{\mu_2\tau^2}{2}, \tag{3.20}$$

that yields the mean decay rate $\bar{\Gamma}$ and the variance μ_2. Polydispersity is often indicated using an index (PI):

$$\mathrm{PI} = \frac{\mu_2}{\bar{\Gamma}^2} \tag{3.21}$$

The cumulant analysis method is usually accurate enough in $\bar{\Gamma}$ for particle systems with PI values < 0.3.[90]

Methods of non-negatively constrained least-squares

The non-negatively constrained least-squares (NNLS) method is suitable for broad monomodal or multimodal distributions. Equation (3.13) is the Laplace transform of $G(\Gamma)$ with respect to Γ. Hence, in theory $G(\Gamma)$ can be obtained by an inverse Laplace transform of the measured autocorrelation function. However, this equation is ill-posed because of the experimental noise and the finite bandwith of real correlators.[90] In the NNLS method, a discrete number m of decay constants Γ_i is used to describe the decay of the autocorrelation function (equation (3.15)). The spacing between the decay constants may be chosen either linearly or logarithmically. The data is fitted to obtain a minimized residuum (equation (3.22))

$$\chi^2 = \sum_{j=1}^{n} \left[g^1(\tau_j) - \sum_{i=1}^{m} G_i e^{(-\Gamma_i \tau_j)} \right]^2 \tag{3.22}$$

with the number of data points n that are considered in the fit. In the fitting procedure, the decay constants G_i and Γ_i are constrained to ≥ 0. A common implementation of NNLS is the CONTIN algorithm developed by Steven Provencher that utilizes a regularized non-negative least-squares technique combined with eigenfunction analysis.[90–92]

Particle size and particle concentration can limit the applicability of DLS. There exists a trade-off for particle concentration: on the one hand, the concentration of the sample should be low enough to avoid multiple scattering, i.e. a scattered photon should not be scattered again before reaching the detector. High concentrations will increase the effect of attractive (van der Waals) or repulsive (electrostatic or steric) particle interaction, too, which will lead to incorrect particle sizes if not considered in analysis.[90]

On the other hand, the concentration has to be high enough to guarantee that there are always enough scatterers in the probed volume (≈ 1000) and the concentration in the scattering volume can be assumed as constant. For a lower number, significant scattering intensity fluctuations may arise, causing either a large baseline error or a smaller apparent diffusion coefficient.[90]

The range of particle sizes accessible to DLS is also limited by the requirement of a stable colloidal suspension: particles that sediment rapidly cannot be analyzed. Large particles strongly scatter and require very low concentrations to avoid multiple scattering, which limits statistics unless very long measurement times are used.[85, 90]

The scattering intensity of the particles has to be distinctly higher than the scattering intensity of the fluid molecules. Very small particles may only provide enough scattering at high concentrations, which can lead to particle-particle interactions (see above). Samples with broad size distributions or multiple size maxima have mixed scattering that may be dominated by only a part of the distribution. The scattering intensity is proportional to x^6; smaller particles are likely not to be detected in the presence of large particles if their concentrations are similar.[85, 90]

3.2.2 Analytical ultracentrifugation

The analytical ultracentrifuge (AUC) was invented in 1924 by the Swedish chemist Theodor Svedberg. He investigated the size distribution of gold colloids with mean diameters of 2 nm and won the Nobel Prize in Chemistry in 1926 for his work on disperse systems. Later, he used the AUC to determine molar masses of biopolymers such as proteins. In the 1970s, analytical ultracentrifugation lost some of its significance due to the emergence of light scattering and other alternatives. New instruments developed in the 1990s seem to have triggered a revival of AUC as a powerful characterization tool for polymers and colloids.

In a typical AUC measurement, dispersed particles sediment with a characteristic velocity during centrifugation that can be measured to determine the PSD. Sedimentation can be observed using optical detectors (e.g. UV-Vis absorption), which detect the change in concentration over time and position.[93, 94]

Theory

Particles in a centrifugal field are affected by

1. the gravitational force F_s induced by the acceleration $\omega^2 r$ of the spinning rotor:

$$F_\mathrm{s} = m_\mathrm{p}\omega^2 r \tag{3.23}$$

   with the mass m_p of the particle, the rotor spinning velocity ω, and the distance r from the rotation axis.[93]

2. the buoyant force F_{b} according to Archimedes' law

$$F_{\mathrm{b}} = -m_{\mathrm{s}}\omega^2 r = -m_{\mathrm{p}}\bar{\nu}\rho_{\mathrm{s}}\omega^2 r \tag{3.24}$$

   with the mass of the displaced solvent m_{s} and the partial specific volume of the particle $\bar{\nu}= (\rho_{\mathrm{p}})^{-1}$.[93]

3. the frictional force F_{f}:

$$F_{\mathrm{f}} = -fu \tag{3.25}$$

   with the frictional coefficient f and the sedimentation velocity u of the particle.[93]

These three forces balance rapidly,

$$F_{\mathrm{s}} + F_{\mathrm{b}} + F_{\mathrm{f}} = m_{\mathrm{p}}\omega^2 r - m_{\mathrm{p}}\bar{\nu}\rho_{\mathrm{s}}\omega^2 r - fu = 0, \tag{3.26}$$

or, upon rearranging,

$$\frac{m_{\mathrm{p}}(1-\bar{\nu}\rho_{\mathrm{s}})}{f} = \frac{u}{\omega^2 r} \equiv s \tag{3.27}$$

Equation (3.27) defines the sedimentation coefficient s that describes the constant ratio between the sedimentation velocity u and the gravitational force $\omega^2 r$. The unit of the sedimentation coefficient is the *Svedberg* [S], defined as $10^{-13}s = 1\mathrm{S}$.[93]

Using Stokes' definition of the frictional coefficient f of a sphere with the diameter x

$$f = 3\pi\eta_{\mathrm{s}}x \tag{3.28}$$

with the viscosity of the solvent η_{s}, the basis for particle size calculation in analytical ultracentrifugation is

$$x = \sqrt{\frac{18\eta_{\mathrm{s}}s}{(\rho_{\mathrm{p}}-\rho_{\mathrm{s}})}} \tag{3.29}$$

that describes the sedimentation equivalent diameter.[93] The sedimentation equivalent diameter of non-solvated, hard spheres with uniform densities is equal to the hydrodynamic diameter. For solvated spheres or non-spherical particles, the sedimentation-equivalent diameter is only a rough measure for the particle system.[94]

The simple mechanical equilibrium of equation (3.29) is often sufficient to describe the sedimentation of particles. A more precise, thermodynamic approach to describe the motion of nanoparticles in a high centrifugal field is the Lamm equation that considers sedimentation and diffusion of the particles. The diffusion term is particularly important for small particles and macromolecules with small sedimentation coefficients and can often be neglected for larger particles. Analysis methods which involve the Lamm equation are only applicable to small, rather narrowly distributed particle systems.[94] In this thesis, particles with broad size distributions were analyzed and thus only analysis methods neglecting diffusion could be used.

Particles in AUC sediment according to their size, density, and shape. A fractionation of the mixture components occurs and a step-like or broadly distributed radial concentration profile $c(r,t)$ (sedimentation profile) with a lower (low particle concentration) and an upper plateau (high particle concentration) can be observed in the sample cell. The concentration gradient between the two plateaus is the so-called sedimentation boundary. Figure 3.2 shows the radial concentration profiles along the sample cell at different times during the experiment.

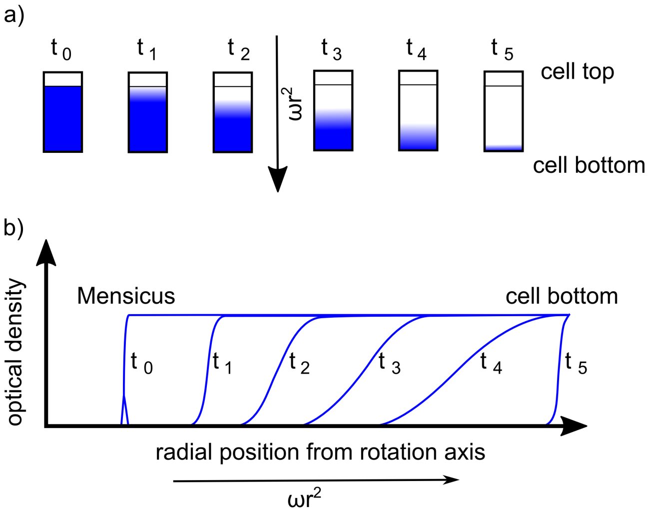

Figure 3.2: Sedimentation of the particles during a sedimentation velocity run induced by the rotational acceleration ωr^2: a) Sedimentation of particles in the cell. Particles sediment with progressing experiment duration towards the cell bottom. b) Time-dependent change in the radial concentration profile $c(r,t)$ inside the cell measured by optical extinction.

At the beginning of the experiment, the particles are equally distributed in the sample cell. As soon as the rotor starts to rotate, air, which is in the sample cell, is instantaneously pressed to the cell top (towards rotation axis) and an air/liquid interface is formed. The interface is called meniscus, whose radial position r_{m} from the rotation axis remains constant throughout the entire experiment. The particles start to sediment (from rotation axis away) towards the cell bottom with the radial position r_{b}. The radial concentration starts to change and a sedimentation boundary is formed. The radial position of the sedimentation boundary is denoted as r_{bnd}.

The velocity of the sedimentation boundary is related to the sedimentation coefficient according to

$$u = \frac{dr_{\mathrm{bnd}}}{dt} \tag{3.30}$$

that can be integrated as

$$\ln \frac{r_{\mathrm{bnd}}}{r_{\mathrm{m}}} = s \int_0^t \omega^2 dt, \tag{3.31}$$

with the running time integral $\int_0^t \omega^2 dt$. The running time integral is a measure for the centrifugal force to which the particle was exposed until time t. Plotting the ratio $\ln(r_{\mathrm{bnd}}/r_{\mathrm{m}})$ over the running time integral leads to a line with the slope s, the mean sedimentation coefficient of the particles.

The mean sedimentation coefficient is a good measure for narrowly distributed monomodal particles. To describe broad or multimodal particle systems, a sedimentation coefficient distribution $g(s)$ can be obtained by

$$g(s) = \frac{d(c(s)/c_0)}{ds} \left(\frac{r}{r_m} \right)^2 \tag{3.32}$$

The distribution function $g(s)$ describes the fraction of particles with a concentration dc/c_0 that have a sedimentation coefficient between s and $s + ds$.

Data analysis

Common analysis of sedimentation curves is performed with the time-derivative method dc/dt [95], the van Holde-Weischet analysis [96], or direct boundary modelling [97–100]. In this thesis the *ls* $g^*(s)$ algorithm implemented in the program *sedfit* developed by Peter Schuck [100], was used. It determines the apparent sedimentation coefficient distribution $g^*(s)$ by direct least-squares boundary modelling and it is suitable to analyze polydisperse systems where the sedimentation coefficients span over orders of magnitude.[101] The program assumes ideal, non-diffusing particles that do not broaden the sedimentation boundary; a good approximation for particles larger than approximately 30 nm.[93, 101] Smaller particles diffuse too fast and high resolution analysis has to consider diffusion by the Lamm equation. The *ls* $g^*(s)$ algorithm only provides a lower resolution analysis of these particles, however, analysis methods based on the Lamm equation fail in analyzing particles with broad size distribution such as the particles extracted from steel.[94]

Sedimentation coefficients were converted into the corresponding particle size using equation (3.29). The density of the particles was taken to be the bulk density of the material. However, for small particles and/or large ligands, the organic ligand can contribute a large fraction of the particle volume and thus, markedly influence the density [102]:

$$\rho_\mathrm{p} = \rho_\mathrm{shell} + \Big(\frac{(x_\mathrm{h} - t_\mathrm{ligand})^3}{x_\mathrm{h}}\Big)(\rho_\mathrm{core} - \rho_\mathrm{shell}) \tag{3.33}$$

with the corrected particle density ρ_p, the density of the organic ligand ρ_shell, the bulk density of the inorganic particle core ρ_core, the thickness of the organic ligand t_ligand, and the hydrodynamic diameter x_h.

Note that the conversion represents an axis transformation and equation (3.7) must be used. The particle size distribution $g(x)$ was obtained from the sedimentation coefficient distribution $g(s)$ by

$$g(x) = g(s)\frac{ds}{dx} = g(s)\frac{x(\rho_p - \rho_s)}{9\eta_s} \tag{3.34}$$

Interactions between sedimenting particles at non-negligible concentrations distort the sedimentation coefficient distribution. For proteins, concentration-dependent hydrodynamic interactions become relevant at concentrations of ~ 0.067 vol.%.[103] I worked with diluted systems with concentrations below $\sim 0.75 \times 10^{-3}$ vol.% and thus neglected particle-particle interactions.

3.2.3 Field-flow fractionation

The term field-flow fractionation (FFF) comprises several techniques that separate particles in a laminar flow which is superimposed by an external field. The field can be a hyrodynamic flow field ("cross-flow"), an electric or magnetic field, or a temperature gradient. It is applied perpendicular to the elution flow that transports the particles through the so-called separation channel. Separation by FFF is possible for nanoparticles, polymers, and proteins.

Theory

The fundamental FFF theory was established by Calvin Giddings in the 1970s.[104] The sequence used for FFF analysis can be divided into three phases: sample injection, relaxation, and elution. During sample injection, the sample is injected into the separation channel and the external field causes the particles to accumulate at the "accumulation wall" of the separation channel. During relaxation, the equilibrium between "opposing forces" (that may be simply Brownian motion, see below) leads them to their equilibrium positions inside the channel. During "elution", the particles are transported towards the channel exit while the external field remains constant or is continuously or stepwise reduced. The elution flow is laminar and thus faster in the channel center than towards the wall. Fractionation of the retained particles, i.e. particles that properly interacted with the external field, is caused by the size-dependant positions of the particles.

The opposing force acting on the particles in "normal" or "Brownian mode" is the diffusion of the particles. The diffusion coefficient of smaller particles is greater and leads to equilibrium position towards the channel center, where the flow has its maximal velocity. The Brownian mode is applicable to particles with diameters below 1 µm and far most common in FFF.[104]

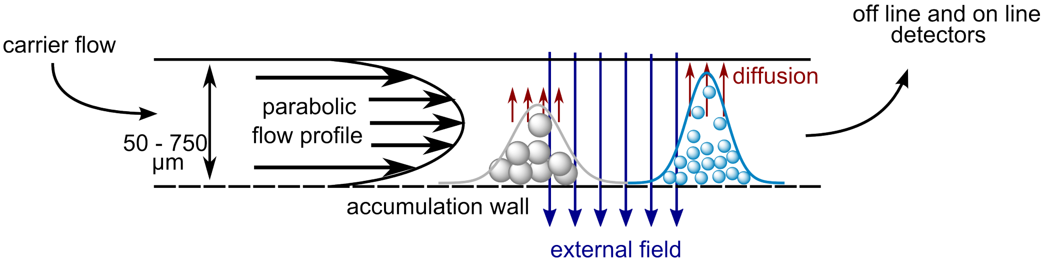

Figure 3.3: Principle of field-flow fractionation in Brownian mode. Adopted from [105].

Flow field-flow fractionation

In this thesis, asymmetrical flow field-flow fractionation (AF4) and hollow-fiber flow field-flow fractionation (HF5) were used. Both methods belong to the family of flow field-flow fractionation (FlFFF) that use a liquid cross-flow as an external field. The cross-flow pushes the particles against the accumulation wall membrane, which is permeable for the solvent but not for the solute.

After sample injection, the sample is focused into a narrow sample zone by two opposing flows (focus flow) that concentrate the sample in a sharp defined zone. After some relaxation time, elution mode ensues. The opposing flows are turned off and the parabolic flow profile transports the particles towards the channel outlet, where the particle concentration is continuously monitored by different detectors. Figure 3.4 shows a typical fractogram of gold nanoparticles.

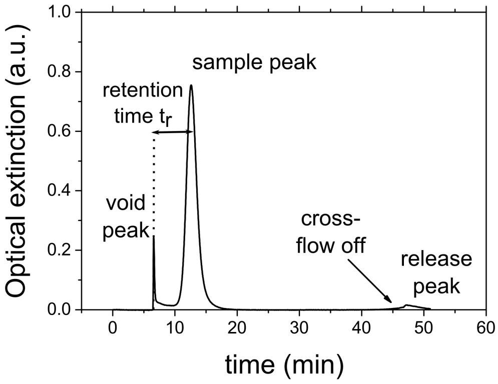

Figure 3.4: AF4 fractogram of gold nanoparticles. The void peak is due to unretained particles and the release peak are overretained particles. The sample peak contains properly retained particles.

The fractogram shows a main sample peak that is accompanied by a "void peak" and a "release peak". The void peak is caused by unretained particles that were not properly relaxed in the focusing step. It mainly contains particles that immediately elute after switching to elution mode and is therefore a good reference for calculating the net retention time. The release peak is caused by particles that were over-retained due to strong interactions with the membrane. These particles only elute after the cross-flow is turned off and they are not further pushed against the accumulation wall.

The elution time of the particles strongly depends on the particle size. The retention ratio R is the ratio between the average fluid velocity and the velocity of the eluting sample. It can be determined from the ratio of the retention time of the void peak t_0 to the retention time of the sample t_r and is often expressed as dimensionless retention parameter [106]

$$\lambda = \frac{V^0 D}{V_\mathrm{c} t_\mathrm{eff}^2} = \frac{1}{6} R \tag{3.35}$$

with the void volume V^0, which can be equated to the experimental retention volume of a component that is not affected by the external field [107], the diffusion coefficient of the analyte D, the volumetric rate of cross-flow V_c, and the effective channel thickness t_{eff}. If t_{eff} is known, the retention time can be directly converted into a diffusion coefficient that is related to the hydrodynamic diameter by the Stokes-Einstein relation. The effective channel thickness is usually obtained by calibration measurements with well-defined reference particles.[106]

It is important to reduce particle-membrane attractions that change retention times. Furthermore, the analyte particles should have properties that lead to similar retention times as the reference particles. It has been shown that the surface chemistry affect particle-membrane interactions and the retention time.[108–111]

In practice, calibration of the FFF is often performed by determining the retention time of reference particles with a series of diameters. Particles, which have an ideal behavior in the separation channel and do not interact with the membrane, show linearly increasing retention times in dependency of the particle size (Figure 3.5 a). In this case, the retention time can be easily converted into a particle size distribution using a linear fit.[112] Complex flow profiles of the cross-flow or particle-membrane interactions can introduce exponential dependencies of retention times on the particle sizes (Figure 3.5 b).[113, 114]

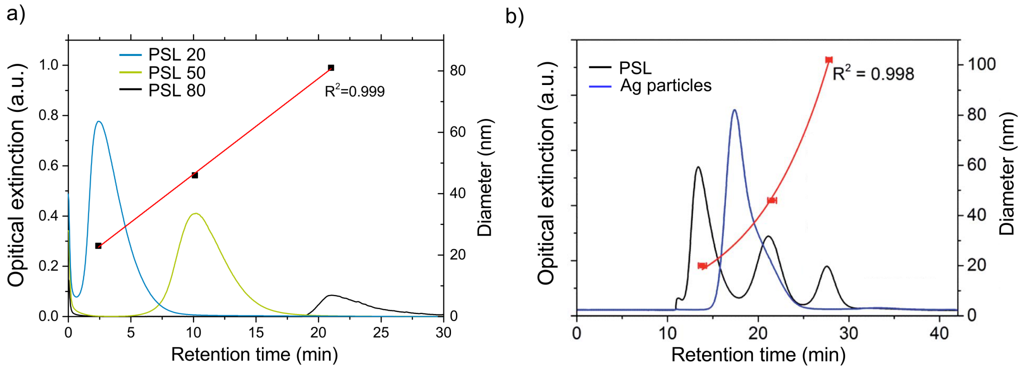

Figure 3.5: Calibration of FFF using retention time: a) ideal linear behavior of PSL particles with nominal diameters of 20, 50, and 80 nm. b) non-ideal behavior of PSL particles with diameters of 20, 46, and 102 nm. The retention time depended exponentially on particle size.[113] Differences in the eluation behavior are caused by different eluants and cross-flow profiles.

It is possible to couple the FFF with dynamic light scattering, static light scattering, UV-Vis, refractive index, and fluorescence detection. This allows a comprehensive analysis of the different fractions of the sample.

3.2.4 Single particle inductively coupled plasma mass spectrometry

Single particle inductively coupled plasma mass spectrometry (SP-ICP-MS) was developed by Degueldre et al. [115] in 2003. It is based on the well-establihed inductively coupled plasma mass spectrometry (ICP-MS) that is widely used for the analysis of liquid samples with ionic analytes and detects many elements down to the ppt regime. The technique is a common standard for trace element analysis in geology and environmental chemistry, but also in steel analysis, e.g. for the determination of trace elements Sb, Bi, Pb, Sn, and P.[116–118]

In SP-ICP-MS, particles are not digested but analyzed individually. The method can thus provide information on the composition and the size for single particles. The origins of SP-ICP-MS were in atmospheric chemistry, but in recent studies it was predominantely used to investigate aqueous environmental samples and for instance the release of nanoparticles into the environment or their behaviour in biological systems was studied.[119]

Theory

An inductively coupled plasma mass spectrometer is composed of a sample introduction system, a plasma source, an interface region, ion focussing optics, and a mass analyzer.

Sample introduction system:
This unit generates small droplets and introduces them to the plasma source. It consists of a nebulizer to generate an aerosol and a spray chamber for droplet selection. In a typical setup, a peristaltic pump pumps the sample into the nebulizer, which forms a distribution of droplets in a carrier gas. Plasma discharge is inefficient with droplets >10 µm; these are removed in the spray chamber so that only droplets with diameters of approx. 5 to 10 µm enter the plasma. The amount of sample that enters the plasma may be as low as 1%. Recently, micro droplet generators were developed that provide uniform droplets with 100% efficiency to reach the plasma. This is particularly interesting for SP-ICP-MS.[119, 120]

Plasma source:
Droplets from the spray chamber are introduced into the plasma, where they

are subjected to high temperatures up to 8000 K, evaporated, atomized, and ionized. Mainly singly charged positive ions are formed.[121] The plasma source is usually an inductively coupled plasma in a plasma torch driven at radio frequency (RF) coil. The most common plasma gas is argon.[122]

Interface region:
Two cones with small round openings aid a pressure reduction from ambient pressure down to 10^{-6} mbar. The assembly transfers the ions from the plasma at ambient pressure into the high vacuum region, where the ion optics and the mass analyzer are located.[123]

Ion optics:
The ion optics focus the ions after passing the interface region to ensure that they reach the mass separator. They remove undesirable matrix- or solvent-based ions, particles, neutral species, and photons.[124]

Mass separator:
The mass analyzer or separator is the key component of the ICP-MS instrument. It separates the ions according to their mass-to-charge ratio (m/z). The quadrupole mass filter is by far the most used in ICP-MS technology. The time-of-flight (TOF) mass analyzer used here is described below.[125]

Detector:
The selected ions are detected as electrical pulses by a detector. Available are channel electron multipliers, Faraday cups, or discrete dynode electron multipliers, which are the most common detector today.[126]

Time-of-flight mass analyzer

The ICP-MS instrument used in this thesis was equipped with a TOF mass analyzer that enables multi-element analysis of fast transient signals and simultaneously detects all analyte ions at once.

A TOF mass analyzer exploits the fact that the kinetic energy E_{kin} of an ion is proportional to its mass m and velocity v:

$$E_{\text{kin}} = \frac{1}{2}mv^2 \tag{3.36}$$

Ions of different mass-to-charge ratios are separated by accelerating them with a voltage U in the first part of the mass analyzer. Since all ions are accelerated with the same voltage, they reach the same kinetic energy. Singly charged ions of individual elements have different masses and therefore reach different velocities in the mass analyzer (equation 3.36). After a fixed distance d, the ions are detected and the time t_d required to reach the detector depends on the mass-to-charge ratio:

$$\frac{m}{z} = \frac{2Ut_\mathrm{d}^2}{d^2} \tag{3.37}$$

Figure 3.6 illustrates the functional scheme of the TOF mass analyzer.

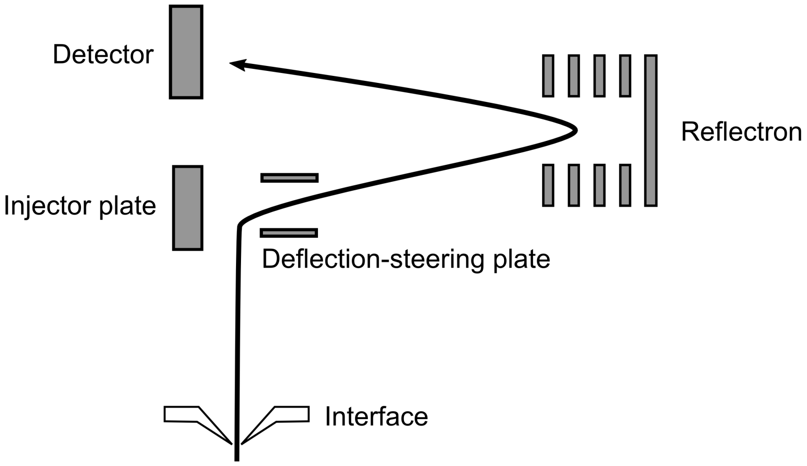

Figure 3.6: Schematic view of a time of flight mass separator. Modified from [125].

Single-particle mode

Mass spectrometry of single particles combines the throughput of an ensemble technique with the specificity of a single counting method. It can be applied to individual nanoparticles to provide rapid information on their size, composition, and concentration.[119] It can detect particles with diameters down to $< 10\,\mathrm{nm}$ and a particle concentration in the range of ng/L, but both limits depend on the analayte element and can be significantly higher.[127]

Solid particles are introduced at low concentration into the plasma without prior digestion and ionized in the ICP to form ion bursts that enter the mass analyzer. All ions in the burst reach the detector simultaneously and cause an electrical pulse with a height that is proportional to the number of ions and thus to the mass of the particle. The particle mass is proportional to the particle size for a constant density.[115, 119, 128]

Size analysis requires prior separation of the signal caused by the particles (pulses) from the background. An iterative method is usually applied to identify all data points with a minimum intensity of 3 (sometimes 5) times the standard deviation of the average signal. The identified peaks are removed from the signal and the process is repeated until no peaks are detected.[119]

The determination of particle number concentrations and particle sizes requires calibration of the ICP-MS. Degueldre et al. [115] used reference nanoparticles with well-known sizes and the same chemical composition as the analyte particles to measure a calibration curve which relates the signal intensity of a particle to its size. However, reference particles of the same material are not always available. Pace et al. [128] assumed that ions from a solution behave like those from nanoparticles after the plasma and developed a calibration method with common metal standards. Their protocol relates the concentration of the dissolved analyte c to the total analyte mass W that enters the plasma during the dwell time t_{dt},

$$W = \eta_{\mathrm{n}} Q_{\mathrm{liq}} t_{\mathrm{dt}} c \tag{3.38}$$

with the transport efficiency η_{n} and the sample flow rate Q_{liq}. The calibration curve relates the signal intensity of a single particle I_{NP} to the particle mass m_{p}, which is obtained by

$$m_{\mathrm{p}} = \frac{1}{w_{\mathrm{a}}} \frac{((I_{\mathrm{NP}} - I_{\mathrm{BKGD}})\eta_{\mathrm{i}}) - b}{m} \tag{3.39}$$

with the mass fraction of the analyzed element in the particle w_{a}, the ionization efficiency η_{i}, the background intensity I_{BKGD}, and the slope m and y-interception b from equation (3.38). The particle mass m_{p} can be transformed into a particle size if the shape and density is known. For a spherical particle,

$$x = \sqrt[3]{\frac{m_{\mathrm{p}} 6}{\rho \pi}} \tag{3.40}$$

The exact determination of the transport efficiency is a prerequisite for the calibration of the SP-ICP-MS using solute metal standards. While the total mass of sample reaching the plasma from a single particle only depends on the particle size, the mass that reaches the plasma during a certain dwell time t_{dt} from a dissolved metal solution depends on the concentration and the volume of the solution (see spray chamber 3.2.4).[128] Different methods based on reference nanoparticles of known size and concentration are available to determine the transport efficiency. The material does not have to be the same as the analyte particles and e.g. gold nanoparticles can be used to determine the transport efficiency. This allows the analysis of nanoparticle systems for which there are no well-defined reference particles but dissolved metal standards.[119, 128]

3.3 Particle detection through optical transmission spectroscopy

Particle sizing techniques such as AUC or FFF fractionate the particle system into different components and detect the individual particle populations and their relative concentrations in the UV-Vis range. Due to detection by light extinction, the size distributions are weighted by the optical extinction of the particles. A comparison of these distributions to TEM data requires transformation into number-weighted distributions (see section 3.1) that requires a relation between particle size and light extinction. In the following, I will briefly discuss the relation between light extinction and particle size and particle concentration.

The concentration-dependent attenuation E_λ of light at a wavelength λ by a solution was first described by Lambert and Beer

$$E_\lambda = \ln\frac{I_0}{I} = -\ln T_\lambda = \epsilon_\lambda c l \tag{3.41}$$

with the transmittance T_λ, the incident light intensity I_0, the transmitted intensity I, the extinction coefficient ϵ_λ, the concentration c of the absorbing species, and the optical path length l. Turbidity $\tau_\lambda$is often defined as

$$\tau_\lambda = \frac{E_\lambda}{l} = \epsilon_\lambda c \tag{3.42}$$

to describe the optical properties of a solution independent of the optical path length.

Lambert-Beer's law holds for molecular solutions when the light extinction is equal to the light absorption. It can be extended to diluted colloidal suspensions if contributions of light scattering are considered, for example using Mie's theory of light scattering. The extinction-weighted distributions can then be transformed into mass-weighted and number-weighted size distributions.[129]

Mie theory of light scattering

Gustav Mie modeled the absorption and scattering of light by a spherical particle.[130] He divided the electromagnetic wave into three partial waves: the incident wave, the wave within the particle, and the scattered wave. The solutions of the Maxwell equations of all three partial waves must be continuous at the phase boundary of the particle and the surrounding medium. Mie provided the solutions for spherical particles.

A detailed treatment of the interaction of light with spherical and non-spherical particles is given by Bohren and Huffman [131], which also provides a computer code for calculating the Mie solutions. I used this code and code from Mätzler [132] to develop a Python code that transforms extinction-weighted particle size distributions into mass-weighted data.

The extinction cross section, a measure for the effective area of the particle that interacts with light, is the sum of the absorbance cross section C_{abs} and the scattering cross section C_{sca} [94]:

$$C_{\mathrm{ext}} = C_{\mathrm{abs}} + C_{\mathrm{sca}} \tag{3.43}$$

that depend on the Mie coefficients a_{i} and b_{i}

$$C_{\mathrm{abs}} = \frac{2\pi}{k^2} \sum_{i=1}^{\infty} (2i+1) \Re(a_{\mathrm{i}} + b_{\mathrm{i}}) \tag{3.44}$$

and

$$C_{\mathrm{sca}} = \frac{2\pi}{k^2} \sum_{i=1}^{\infty} (|a_{\mathrm{i}}|^2 + |b_{\mathrm{i}}|^2) \tag{3.45}$$

where k is the wave number in the surrounding medium and $\Re(a_{\mathrm{i}} + b_{\mathrm{i}})$ is the real part of the complex Mie coefficients. The Mie coeffcients are functions of the complex refractive index of the particles.

The extinction cross section is defined for a single particle. The turbidity for a given number density N_{p} of particles is

$$\tau = N_{\mathrm{p}} C_{\mathrm{ext}} \tag{3.46}$$

Replacing the number density with the volume fraction ϕ of all particles and the individual particle volume V_{p} yields

$$\tau = \frac{\phi}{V_{\mathrm{p}}} C_{\mathrm{ext}} \tag{3.47}$$

The extinction cross section can be normalized to the particle cross section to obtain the extinction efficiency

$$Q_{\mathrm{ext}} = \frac{C_{\mathrm{ext}}}{A_{\mathrm{p}}} = \frac{4C_{\mathrm{ext}}}{\pi x^2} \tag{3.48}$$

so that

$$\tau = \frac{3\phi Q_{\text{ext}}}{2x} \tag{3.49}$$

The volume fraction of particles in diluted systems can be correlated to the mass/volume concentration:

$$\phi = \frac{V_{\text{p,total}}}{V_{\text{total}}} = \frac{V_{\text{p,total}}}{V_{\text{s}} + V_{\text{p,total}}} \approx \frac{V_{\text{p,total}}}{V_{\text{s,total}}} = \frac{m_{\text{p,total}}}{\rho_{\text{p}} V_{\text{s,total}}} = \frac{c}{\rho_{\text{p}}} \tag{3.50}$$

with the volume of the solvent V_{s}, the volume of all particles $V_{\text{p,total}}$, the mass of the particles m_{p}, and the particle density ρ_{p}. If the particle volume is negligible compared to the volume of the solvent, the turbidity and the extinction coefficient can be written as

$$\tau_\lambda = \frac{3cQ_{\text{ext},\lambda}}{2x\rho_{\text{p}}} \tag{3.51}$$

and

$$\epsilon_\lambda = \frac{3Q_{\text{ext},\lambda}}{2x\rho_{\text{p}}} \tag{3.52}$$

Equation (3.52) enables the calculation of the extinction coefficient of particles with a diameter x and a density ρ_{p}. With equation (3.41), the measured attenuation can be converted into the particle mass concentration

$$c = \frac{E_\lambda}{d\epsilon_\lambda} = \frac{E_\lambda}{d}\left(\frac{3Q_{\text{ext},\lambda}}{2x\rho_{\text{p}}}\right)^{-1} \tag{3.53}$$

3.4 Reconstruction of multimodal particle size distributions

The precipitates in microalloyed steel have diameters between a few and several hundred nanometers. Their size distributions are multimodal and related to the mechanical properties of the steel. Particles smaller than 10 nm are important for precipitation hardening; particles on the order of 10 to 100 nm lead to grain refinement due to retardation of recrystallization and pinning of grain boundaries.[15] This thesis reports on colloidal methods to reconstruct the size distributions based on the analysis of large particle numbers.

The ideal analytical technique for extracted particles would provide sufficient resolution from the smallest to the largest particles to resolve all maxima of the distribtion. Literature contains reports on the suitability of different colloidal analytic techniques for broad, multimodally distributed particle mixtures. Anderson et al. [133] and Bell et al [134] analyzed multimodal particle mixtures with diameters between 100 and 500 nm; Cascio et al. [135] investigated metallic silver nanoparticles with diameters between 20 and 100 nm. All authors found that fractionating methods, such as differential centrifugation or field-flow fractionation, are able to successfully measure the PSD of multimodally distributed particles and resolve the individual particle fractions, while ensemble methods such as DLS do not generally provide correct size distribution of particle mixtures.

I tested and compared colloidal techniques on particles extracted from steel (section 4.1) and on multimodal model particle mixtures with well-known size distributions with particles diameters between 5 and 80 nm. The results for model particles are discussed in this section.

3.4.1 Model particle systems

Silica, polystyrene latex, and gold model particles with narrow, monomodal size distributions and different mean diameters were mixed to obtain multimodal models. I studied whether a given colloidal technique could differentiate the different particle fractions and how well the mean, width, median, and modal value measured on the particle fractions in the mixture coincided with the sizes measured on the monomodal reference particle dispersions. I used different base materials (ceramic, polymer, and metal) to study the influence of different types of materials and associated properties such as density or surfaces properties on the measurement settings.

The different methods that were tested use different detectors: AUC and FFF use light extinction, DLS uses light scattering. This causes different sensitivities for different particle sizes such that certain methods better detect small particles with low concentrations. In order to use one particle mixture for all methods, it was necessary to select the concentrations of the particles in such a way that they could be analyzed with all methods. Therefore, the reference particle dispersions were prepared such that every particle population had at least an optical density of 0.1 to 0.3 OD and that the maximum optical density of the particle mixture was below 1 OD at a cuvette length of 12 mm.

- Silica reference particles with nominal diameters of 20, 50, and 80 nm were synthesized according to Hartlen et al. [136] and mixed to obtain multimodal particle model systems. The mean diameters and the standard deviations (stddev) of the individual particles measured with

TEM are given in Table 3.1; the density of such particles was reported to be between 1.85 to 2 g/cm^3.[137, 138] Here, I assumed a density of 1.9 g/cm^3 to calculate the size in analytical ultracentrifugation. A single particle batch of 20 nm was split and used for DLS and AUC; a different batch of 20 nm particles was used for FFF investigations. The final concentration of the particles in the sample solutions for DLS and AUC was 1262 mg/L for the 20 nm particles, 278 mg/L for the 50 nm particles, and 70.4 mg/L for the 80 nm particles. The samples analyzed with FFF had final concentrations of 181 mg/L for the 20 nm particles, 278 mg/L for the 50 nm particles, and 70.4 mg/L for the 80 nm particles.

- Polystyrene latex (PSL) reference particles were bought from Thermo Scientific (Fremont, USA). The nominal diameters of the particles were 20, 50, and 80 nm. The mean diameters and standard deviations measured with TEM (provided by manufacturer) are given in Table 3.1. The particle stock solutions were diluted for analysis. The final concentrations in the individual particle suspensions and the particle mixture was 6.7 mg/L for the 20 nm particles, 4 mg/L for the 50 nm particles, and 1.25 mg/L for the 80 nm particles. The density of the particles given by the manufacturer was 1.05 g/cm^3.

- Citrate stabilized gold nanoparticles were bought from Nanocomposix (San Diego, USA). The nominal diameters of the particles were 5, 20, and 50 nm. The mean diameters and standard deviations measured with TEM (provided by manufacturer) are given in Table 3.1. For FFF analysis, the particles were modified with bis(p-sulfonatophenyl)phenylphosphine (BSP) to reduce losses and agglomeration.[105] The density of the particles was 19.3 g/cm^3. The final concentration of each particle fraction in the mixture was 17 mg/L.

	mean (nm)	stddev (nm)
SiO_2-20	20	1.9
SiO_2-20*	23	3.4
SiO_2-50	46	2
SiO_2-80	72	2.3
PSL-20	23	-
PSL-50	46	7.3
PSL-80	81	9.5
Au-5	4.5	0.4
Au-20	20.0	2.5
Au-50	48.2	6.6

*Particles measured with FFF

Table 3.1: Mean and standard deviation of the individual particle populations used for the formation of the multimodal particle mixtures. The data for PSL and Au nanoparticles were provided by the manufacturer; silica particles were analyzed with TEM in combination with manual image analysis.

3.4.2 Characterization of model particle mixtures

Monomodal and multimodal reference particle dispersions were subjected to dynamic light scattering, analytical ultracentrifugation, and field-flow fraction and the results were compared. I used the mean, standard deviation, median, and mode of the monomodal reference particle dispersions to evaluate the resolution of the multimodal mixtures for different analysis methods. The study identified methods suitable for resolving multimodal distributions with several components in the range of 5 to 100 nm that were then considered for the analysis of extracted particles from steel.

Dynamic light scattering

Dynamic light scattering was done using a Zetasizer Nano ZSP (Malvern Instruments, Germany). The data was analyzed using the NNLS algorithm implemented in the Zetasizer software 7.11. Analysis provided an intensity-weighted size distribution; no further transformation was performed to avoid possible artefacts.

The distributions of the monomodal reference particle dispersions (dashed lines) and the multimodal particle mixture (solid line) for silica, polystyrene, and gold particles as measured by DLS are illustrated in Figure 3.7. The corresponding mean, standard deviation, median, and mode values of the intensity-weighted size distributions for the monomodal reference particle dispersions are given in Table 3.2, 3.3, and 3.4. The multimodal particle mixture could not be resolved for any of the three model particle mixtures due to lack of resolving power.

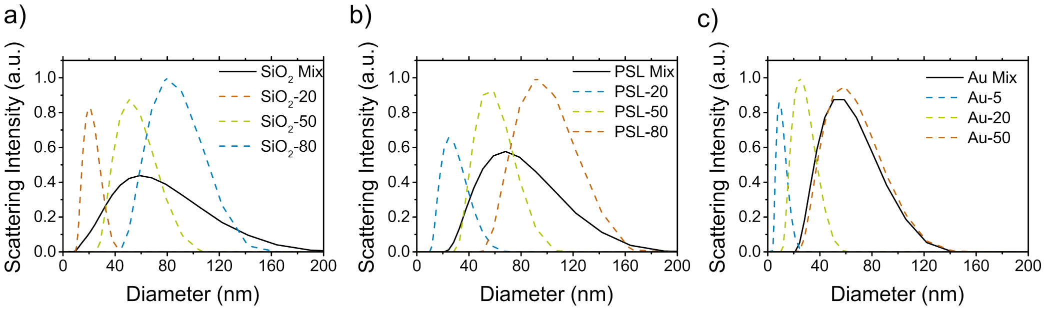

Figure 3.7: PSD of the monomodal reference particle dispersions (dashed lines) and the particle mixture (solid lines) measured by means of DLS.

	mean (nm)	stddev (nm)	median (nm)	mode (nm)
SiO_2-20 single	23.6	7.6	22.4	20.7
SiO_2-20 mix	-	-	-	-
SiO_2-50 single	59.5	18.5	57.0	51.8
SiO_2-50 mix	-	-	-	-
SiO_2-80 single	90.6	24.2	88.0	81.1
SiO_2-80 mix	-	-	-	-

Table 3.2: Statistical characteristics of the PSD of monomodal silica reference particle dispersions and the particle mixture measured with DLS.

	mean (nm)	stddev (nm)	median (nm)	mode (nm)
PSL-20 single	32.3	13.4	31.1	25.9
PSL-20 mix	-	-	-	-
PSL-50 single	62.6	17.4	60.4	55.2
PSL-50 mix	-	-	-	-
PSL-80 single	103.1	26.7	100.1	93.2
PSL-80 mix	-	-	-	-

Table 3.3: Statistical characteristics of the PSD of monomodal PSL reference particle dispersions and the particle mixture measured with DLS.

	mean (nm)	stddev (nm)	median (nm)	mode (nm)
Au-5 single	12.2	5.4	12.1	8.6
Au-5 mix	-	-	-	-
Au-20 single	30.2	11.0	29.4	24.2
Au-20 mix	-	-	-	-
Au-50 single	71.2	27.5	67.3	57.0
Au-50 mix	-	-	-	-

Table 3.4: Statistical characteristics of the PSD of monomodal Au reference particle dispersions and the particle mixture measured with DLS.

The monomodal reference particle dispersions all have DLS results indicating wide distributions with large standard deviations (Figure 3.7) compared to the standard deviations of the distributions measured with TEM (see Table 3.1). This is due to the intensity-weighted size distribution, giving a few large particles a large contribution to the relative frequency, causing the distribution to appear broader.

The particle mixtures were indicated to have broad, monomodal distributions. The polystyrene latex and silica particle mixture had distributions with maxima between the medium and large sized particle population. The gold particle mixture had a distribution that was almost identical with the distribution of the largest particle fraction.

Dynamic light scattering is an ensemble technique and many particles simultaneously contribute to the measurement signal. The resolution of the technique is limited and only particles can be distinguished which differ by a factor of 2 (ideal conditions) [90, 139], in reality rather factor 3 [135], or more in diffusion coefficient or diameter, respectively. The optical scattering cross-section is proportional to the 6^{th} power of the particle diameter (see section 3.2.1) so that DLS is more sensitive to larger particles. Wide particle size distributions are known to be shifted towards larger particle sizes.[140] In the gold particle mixture the scattering signal is dominated by the largest particle population and the measured distribution of the mixture is almost equal to the distribution of the largest particle fraction. In the PSL and silica particle mixture the concentration of the small and medium sized particles is high enough to contribute a sufficient part to the scattering signal. The peak maximum of the measured distribution is in between the large and medium sized particle population.

Analytical ultracentrifugation

A preparative centrifuge (Optima XL-80K, Beckman-Coulter, USA) modified with a multiwavelength detector (MWL-AUC) [141, 142] with two-sector titanium centerpieces (Nanolytics, Germany) was used for all experiments. All samples were centrifuged at a temperature of 20 °C, silica and gold particles at 5000 rpm, polystyrene latex particles at 20 000 rpm. Sedimentation velocity experiments were performed and all sedimentation profiles were observed through optical transmission at a wavelength of 261 nm. Data analysis was performed using the $ls\ g^{*}(s)$ method implemented in Sedfit.[100] The sedimentation distribution was transformed into extinction-weighted particle size distribution without further corrections.

Figure 3.8 illustrates the distributions of the monomodal reference particle dispersions (dashed lines) and the multimodal particle mixture (solid line) as measured by AUC. For silica and PSL particle mixtures, the three particle populations were clearly resolved. For the gold particle mixture, the large particle population was not found, but the other populations showed very good agreement with the distributions of the monomodal reference particle dispersions. The mean, standard deviation, median, and mode of the individual peaks measured in the particle mixture and the corresponding single component are given in Table 3.5, 3.6, and 3.7.

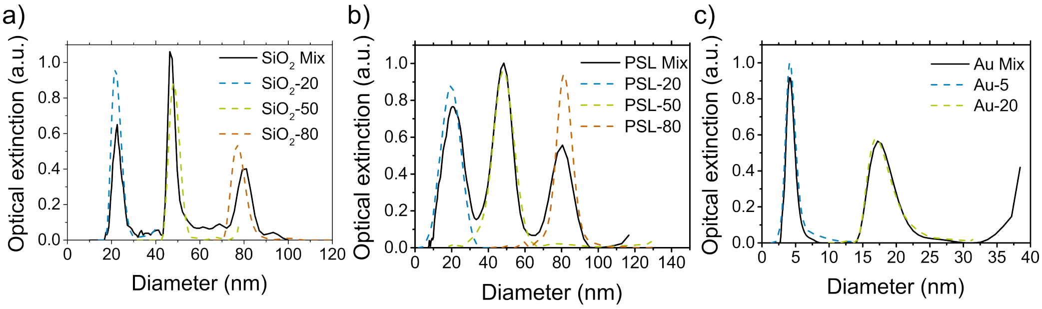

Figure 3.8: PSD of the monomodal reference particle dispersions (dashed lines) and the particle mixture (solid lines) measured by means of AUC.

	mean (nm)	stddev (nm)	median (nm)	mode (nm)
SiO_2-20 single	22.5	2.4	22.3	21.7
SiO_2-20 mix	22.8	2.2	22.7	22.3
SiO_2-50 single	48.7	2.5	48.5	48.1
SiO_2-50 mix	47.7	2.1	47.5	46.8
SiO_2-80 single	77.9	3.4	77.6	76.9
SiO_2-80 mix	76.4	7.2	78.3	81.1

Table 3.5: Statistical characteristics of the PSD of monomodal silica reference particle dispersions and the particle mixture measured by AUC.

	mean (nm)	stddev (nm)	median (nm)	mode (nm)
PSL-20 single	19.5	5.5	19.6	19.6
PSL-20 mix	21.1	6.1	21.1	20.8
PSL-50 single	48.3	5.8	48.3	48.3
PSL-50 mix	47.4	5.4	47.8	48.3
PSL-80 single	81.6	4.3	81.6	81.4
PSL-80 mix	79.2	6.1	79.7	80.5

Table 3.6: Statistical characteristics of the PSD of monomodal PSL reference particle dispersions and the particle mixture measured by AUC.

	mean (nm)	stddev (nm)	median (nm)	mode (nm)
Au-5 single	4.4	0.8	4.3	4.2
Au-5 mix	4.4	0.8	4.3	4.2
Au-20 single	18.4	2.4	17.9	17.0
Au-20 mix	18.3	2.1	18.0	17.4
Au-50 single	-	-	-	-
Au-50 mix	-	-	-	-

Table 3.7: Statistical characteristics of monomodal Au reference particle dispersions and the particle mixture measured by AUC.

The standard deviations of the monomodal reference particle dispersions were in the same range as the standard deviations measured with TEM.

For the gold particle mixture, only the 5 nm and the 20 nm particle populations were found, while the 50 nm fraction was not detected. The large density of the gold particles resulted in large differences in the sedimentation coefficients and the rotational speed was chosen too fast to detect the 50 nm particle fraction. Lower rotational speeds would enable their analysis, but impede the analysis of the smallest particle fraction. A concurrent analysis of all particle fractions at constant speed is not possible; a possible future remedy are modern protocols that involve a speed ramp.[143]

Differences in the area under the peaks of the distributions indicate a difference in particle concentration, which may be caused by partial agglomeration of particles.

Flow field-flow fractionation

Asymmetric flow field-flow fractionation was performed on a Wyatt Eclipse DUALTEC flow field-flow fractionation system (Wyatt Technology Europe, Germany) using a quaternary pump with an integrated degassing system and an autosampler (Agilent Technologies 1260 infinity series, Agilent, Germany). A short channel equipped with a polyethersulfone (PES) membrane with a mean cut-off of 10 kDa (Microdyn-Nadir, Germany) was used as separation channel. The channel was connected to a variable wavelength UV-Vis detector (Agilent Technologies 1260 infinity series) that measured extinction at 280 nm.

The eluent was composed of 0.05 wt.% sodium dodecyl sulfate (SDS) and 0.2 mM $NaNO_3$ for the silica particles and 0.005 wt.% SDS for the PSL and gold particles. The eluent and the flow parameters (focus flow, detector flow, and cross flow rates) were optimized for maximal particle recovery and particle separation (data not shown here). The membrane was conditioned for 2 h with the corresponding eluent. Blank runs were performed between each measurement to ensure complete particle elution and membrane desorption of adsorbed species.

Particle size distribution analysis was performed using the retention times of reference particles in combination with UV-Vis particle detection. Calibration was performed using the monomodal reference particle dispersions, which were also used to produce the model particle mixture. Hydrodynamic diameters of the calibration particles were determined with DLS using cumulant analysis. The retention time distribution $g(t)$ was transformed into the particle size distribution $g(x)$ using equation (3.7).

Particles were detected using UV-Vis transmission measurements that were more sensitive to small particles than light scattering detection. In situ dynamic light scattering was performed as reference measurement (see appendix A.1). The sizes obtained with in situ DLS were in good agreement with the sizes obtained with retention time determination.

The distributions of the multimodal particle mixtures (solid line) and the monomodal reference particle dispersions (dashed lines) are given in

Figure 3.9. The means, standard deviations, medians, and modes of the extinction-weighted size distributions measured with field-flow fractionation for the monomodal reference particle dispersions and the particle mixture are given in Table 3.8, 3.9, and 3.10. The particles were well-separated and the particle distributions were almost identical.

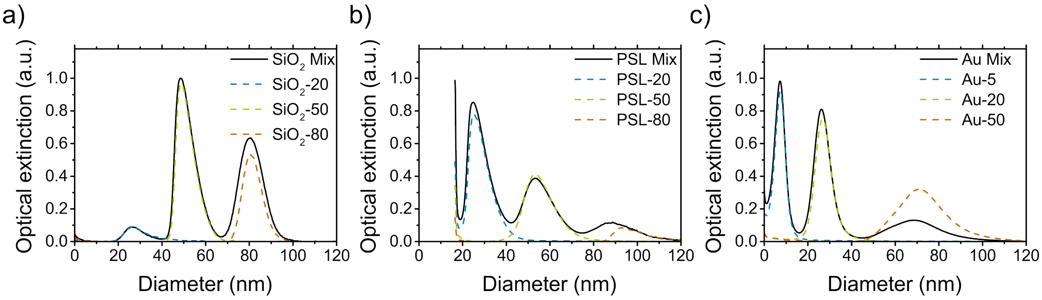

Figure 3.9: PSD of the monomodal reference particle dispersions (dashed lines) and the particle mixture (solid lines) measured by means of FFF.

	mean (nm)	stddev (nm)	median (nm)	mode (nm)
SiO_2-20 single	30.7	7.4	29.1	26.4
SiO_2-20 mix	28.1	4.8	27.5	26.4
SiO_2-50 single	52.9	6.2	51.4	49.0
SiO_2-50 mix	53.1	4.8	51.4	48.6
SiO_2-80 single	81.9	4.6	81.5	80.7
SiO_2-80 mix	81.6	5.6	81.2	80.3

Table 3.8: Statistical characteristics of the PSD of monomodal silica reference particle dispersions and the particle mixture measured by FFF.

	mean (nm)	stddev (nm)	median (nm)	mode (nm)
PSL-20 single	29.8	6.9	28.2	25.6
PSL-20 mix	29.8	7.4	28.0	25.1
PSL-50 single	56.5	7.5	55.4	53.4
PSL-50 mix	57.7	8.6	56.1	53.3
PSL-80 single	101.4	10.9	98.4	93.0
PSL-80 mix	100.1	15.0	97.1	88.6

Table 3.9: Statistical characteristics of the PSD of monomodal PSL reference particle dispersions and the fractions in the particle mixture measured by FFF.

	mean (nm)	stddev (nm)	median (nm)	mode (nm)
Au-5 single	6.8	2.5	7.0	7.5
Au-5 mix	6.5	2.6	6.9	7.4
Au-20 single	27.5	3.8	27.3	26.7
Au-20 mix	26.9	3.9	26.7	26.2
Au-50 single	72.4	11.0	71.9	70.8
Au-50 mix	68.4	12.5	68.4	68.4

Table 3.10: Statistical characteristics of the PSD of monomodal Au reference particle dispersions and the corresponding fractions in the particle mixture measured with FFF.

The individual particle populations appeared to be slightly broader than in TEM measurements (Table 3.1).

The differences in the particle concentration found for the 80 nm silica particles and the 50 nm gold nanoparticles particles are probably caused by agglomeration of the particles or partial adsorption of particles at the separation membrane. Particles are in close vicinity of the membrane during separation and particle may adsorb (see appendix A.1).

3.5 Methods suitable to characterize broad multimodal particle mixtures

In summary, the sizing methods tested in this thesis performed very differently in resolving the reference particle mixtures. Fractionating of the particles before (FFF) or during (AUC) analysis increased resolution; optical extinction of the fractionated sample resolved the monomodal reference particle dispersions of the mixtures and correctly described them. Direct dynamic light scattering of the unfractionated mixture was unable to distinguish between particle fractions in the size range of 1 to 100 nm and is not suitable for the analysis of the extracted particles.

Analytical ultracentrifugation is a relatively simple measurement. Only the rotation speed, the concentration, and the ionic strength of the dispersion have to be adjusted. Separation takes place in a relatively large volume with a small surface-area involved and particle losses are small. The separation of the particles, however, depends both on particle size and density. It is challenging or impossible to characterize all sizes in a broad mixture at a fixed rotational speed.

Field-flow fractionation provides separation according to hydrodynamic diameters independent of the density even with very wide size distributions.

The method requires the optimization of a large number of parameters such as particle separation, particle recovery, and experiment duration for each sample type, which may be time-consuming and needs many test runs. The separation channel of FFF is smaller than centrifugation tubes and the particles accumulate close to its walls, which can lead to significant particle losses through adsorption.

Chapter 4

Colloidal analysis of particles extracted from steel

Advanced steel development requires accurate information on the size and composition of particles that form during the thermomechanical controlled rolling process to optimize processing conditions and alloy design. Thus, the analysis of precipitates in microalloyed steels is of great importance for the steel plants. Common today is electron microscopy of thin steel foils or carbon extraction replicas. However, electron microscopy is time-consuming and does not allow for the routine analysis of large numbers of particles (see section 1.4.1). An alternative that provides statistically meaningful data is the matrix dissolution technique in combination with colloidal characterization.

The particle extraction protocol established in chapter 2 provides large numbers of particles that are suitable for colloidal analysis. In the previous chapter, analytical ultracentrifugation and flow field-flow fraction were identified as suitable for the analysis of broad multimodal particle distributions. Both can analyze particle numbers on the order of 10^9 in less than half a day. In the first part of this chapter, I report on PSDs of particles extracted from microalloyed steel using AUC and FFF and compare the results to data obtained from electron microscopy.

In the second part of this chapter, I report on single particle inductively coupled plasma mass spectrometry on such particles that provides information on the particle size and composition and compare them to results from electron microscopy.

4.1 Size analysis by analytical ultracentrifugation and field-flow fractionation

Analytical ultracentrifugation and field-flow fractionation can analyze broad multimodal model particle mixtures, as reported in section 3.4. They accurately determined the individual populations in the mixture with only small deviations. Both methods were applied to particles extracted from three different steel samples with different alloy concepts and the results were compared to data obtained by electron microscopy.

Two steels with only one microalloy element and one steel with two microalloy elements were investigated by AUC and FFF. One steel contained only titanium (steel A), the second steel contained almost only niobium (steel B), and the third steel contained both niobium and titanium (steel C).

The surfactant introduced during particle extraction affects both AUC and FFF. Both methods measure the hydrodynamic diameter including the ligand shell. Steel industry is only interested in the core size; the size of the ligand needs to be subtracted. The surfactant also influences the particle density that amounts for a large proportion of the volume for small particles. Ligand shell thickness and density are required to calculate a corrected particle density in order to calculate the particle size (see section 3.2.2). I used well-defined gold reference particles coated with the surfactant to determine its size and density. These coated reference particles were also used for FFF, where reference particles for retention time calibration are required that have surface properties similar to the analyte particles.

4.1.1 Experimental procedures

Extraction

Three different steel samples with different alloying concepts were provided by the AG der Dillinger Hüttenwerke. An overview of the most important alloy components of the three steels is given in Table 4.1. The complete chemical composition of the steels can be found in appendix B.1.

Element (wt%)	C	Si	N	Al	Cr	**Nb**	**Ti**	CEV
Steel A	0.06	0.43	0.003	0.03	0.23	**0.001**	**0.008**	0.368
Steel B	0.05	0.28	0.004	0.03	0.05	**0.02**	**0.003**	0.378
Steel C	0.06	0.17	0.004	0.03	0.03	**0.04**	**0.02**	0.424

Table 4.1: Selection of the most important alloy components of the three investigated steels.

The samples were provided as chippings that were washed with isopropyl alcohol and acetone and subsequently dissolved according to the extraction protocol developed in chapter 2. The dissolution time strongly depended on the composition of the steel. Steel A required only 2 h for complete dissolution, steel B required 5 h, and steel C required 8 h. The particle suspensions obtained after dissolution were centrifuged using an ultracentrifuge (XL-I 70 K, Beckman-Coulter, Germany) at 504 000 rcf (Rotor Type 70-Ti, Beckman-Coulter) and 20 °C for 90 min.

A volume of 2 mL of the iron-free particle suspension was sonicated with an ultrasound sonotrode (UP200St ultrasound processor and S26d2 sonotrode, Hielscher, Germany) for 2 min. A TEM sample was prepared by drop-casting of 2.5 µL of the particle suspension on a copper grid coated with amorphous carbon. A volume of 5 µL of sodium hydroxide with a concentration of 1 mol/L was added to obtain a pH of approximately 10-11 and the mixture was sonicated again for 2 min. Subsequently, the sample solution was filtered using a PES filter with a pore size of 0.22 µm and then was ready for analysis with AUC and FFF.

Analysis

Electron microscopy

TEM measurements were performed using a *JEM-2100* transmission electron microscope from JEOL (Germany) with an acceleration voltage of 200 kV. EDX analysis was performed using a Noran System 7 X-ray Microanalysis System (Thermo Scientific). For sample preparation, 2.5 µL of the particle suspension was dried on a carbon coated copper grid. The particle size was evaluated with the FIJI software [144] by determining the diameter of a circle of the same area.

Dynamic light scattering and Zeta potential

DLS and Zeta potential measurements were conducted on a Zetasizer Nano ZSP (Malvern Instruments, Germany). Size analysis was done using the cumulant fit method implemented in the Zetasizer software 7.11. Zeta potential was determined by measuring the electrophoretic mobility and analysis using the Smoluchowski model.

Analytical ultracentrifugation

Sedimentation velocity experiments were performed using a preparative centrifuge (Optima XL-80K, Beckman-Coulter, USA) equipped with a multiwavelength detector [141, 142] in order to study the density and the size of the Disperbyk-ligand shell and the particle size distribution of the particles extracted from steel. Two-sector titanium centerpieces (Nanolytics, Germany) were used for all experiments. The samples were centrifuged at a temperature of 20 °C. Steel A was centrifuged at 10 000 rpm, steel B and C at 5000 rpm. 290 scans were recorded for steel A and B and 300 scans were recorded for steel C. The recorded spectrum ranged from 250 to 700 nm. Data analysis was performed using the $ls\ g^*(s)$ method implemented in Sedfit.[100] The obtained sedimentation distribution curves were transformed into size distribution curves using equation (3.34), (3.29), and (3.8).

Field-flow fractionation

Hollow-fiber flow field-flow fractionation was used to determine the PSD of the extracted particles. Characterization was performed on a Wyatt Eclipse DUALTEC flow field-flow fractionation system (Wyatt Technology Europe, Germany) using a quaternary pump with an integrated degassing system and an autosampler (Agilent Technologies 1260 infinity series, Agilent, Germany). A hollow-fiber made of a PES membrane with a inner diameter of 800 µm was used as separation channel (Wyatt Technology Europe, Germany). Reference particles were analyzed by AF4; however, the experiments (data not included in this thesis) showed a weak signal of the particles extracted from steel, probably caused by too high dilution. Therefore, I decided to use a hollow fiber, which has a smaller volume and reduces sample dilution. Also, the total membrane area is smaller which reduces potential membrane related sample loss.

The channel was connected to a variable wavelength UV-Vis detector (Agilent Technologies 1260 infinity series) that measured extinction at 280 nm.

The eluent was composed of 0.01 mM NaOH and 0.005 wt.% SDS. Eluent composition and the flow parameters (focus flow, detector flow, and cross flow) were optimized considering particle recovery and particle separation beforehand (data not shown here). The membrane was conditioned for 2 h with the corresponding eluent. Blank runs were performed between each measurement to ensure complete particle elution and membrane desorption of adsorbed species. The retention time was used to determine the PSD by development and application of suitable reference particles. The calibration procedure involved the analysis of the gold reference particles using the identical setup and parameters as for the analyte characterization (see appendix B.4).

4.1.2 Comparison of different analysis methods

The particle size distributions for the different steel samples measured with AUC, FFF, and TEM were compared to data obtained from STEM (SEM in STEM mode) analysis of carbon extraction replicas[1] with automatic image analysis [145] (Figure 4.1).

---

[1] Sample preparation and analysis were performed at AG der Dillinger Hüttenwerke in the frame of the master thesis of Thomas Roth [145].

The results of AUC, FFF, and TEM for the different steel samples are provided in appendix B.2, B.3, and B.4. It is necessary to remember that AUC and FFF provide extinction-weighted distributions, while electron microscopy provides number-weighted distributions. In order to quantitatively compare the results, a conversion of the extinction-weighted size distributions into mass and number-weighted distributions is required using Mie theory. However, I found (appendix B.5) that this transformation cannot be done because of the complex composition, shape, and morphology of the particles.

A qualitative comparison of particle fractions and their size shows a good agreement with the PSD of the particles on the extraction replicas measured with STEM and retrieved the same number and sizes of the particle fractions. The relative frequency of the individual fractions was significantly different as expected for the different weighting of the size distributions.

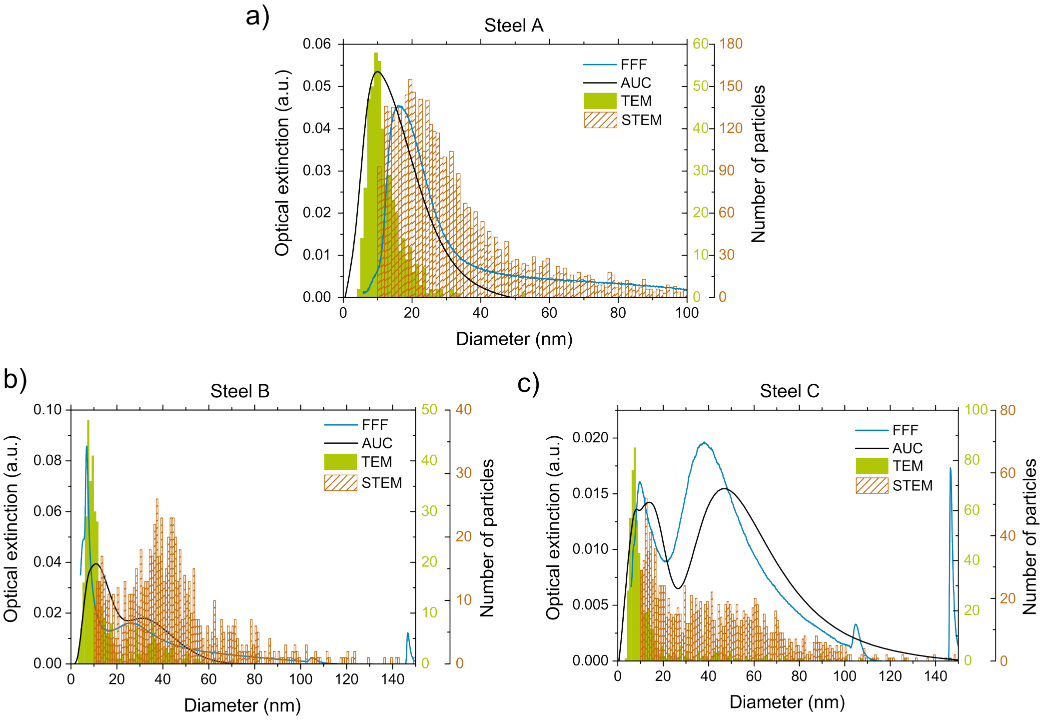

Figure 4.1: Particle size distributions of extracted particles from three different steels meausured with TEM, FFF, and AUC. The different PSDs were compared to data from STEM analysis on carbon extraction replicas [145]. a) Steel A, b) steel B, c) steel C.

For steel A, all analysis methods found a monomodal distribution with a diameter of approximately 10 to 15 nm. The particle sizes measured with

TEM and AUC were in very good agreement. FFF and STEM found slightly larger particle sizes.

For steel B, a bimodal distribution was found with a small fraction with diameters of around 10 nm and a larger fraction with diameters of approximately 40 nm. The smaller size fraction was very similar in TEM, AUC, FFF, and STEM. For the larger particle fraction, AUC and FFF found slightly smaller sizes than TEM and STEM.

Steel C had one smaller size fraction with diameters of approximately 10 nm and a larger size fraction with diameters of approximately 50 nm. The sizes of all fractions were in good agreement. FFF and AUC measured slightly smaller values than TEM and STEM.

Replicas of steel A and B were also analyzed in TEM using manual image analysis. For steel A, a similar particle size distribution as for TEM analysis of the extracted particles was found. However, the number of particles per area was drastically reduced. For steel B, only the large size fraction was found, the small particle fraction was not transferred to the replica.

TEM vs. STEM

The manual analysis of TEM images and the automatic image analysis with STEM led to similar size distributions. For larger particles ($> 20\,\text{nm}$) the distribution shapes were well matched. Differences in the distribution were observed for particles with a diameter range of 10 to 20 nm.

The resolution of the STEM was limited due to the low acceleration voltage of the SEM and the threshold of the minimum particle diameter was set to 10 nm to avoid uncertainties. Thus, the PSD was cut off at 10 nm. As can be seen in TEM, however, most particles are smaller than 10 nm. Differences in the PSD caused by particle etching (chapter 2) during extraction are negligible (see appendix B.6).

AUC vs. FFF

The two colloidal methods measured slightly deviating size distributions, possibly due to the different operating principles. While particle fractionation in FFF only depends on the hydrodynamic diameter, the particle density affects AUC. The composition of the particles is heterogeneous and there may be both uniform particles with different compositions and particles composed of several phases. Vacancies in the crystal lattice of the carbonitride precipitates affect their density, too.

The density and size of the ligand shell was only estimated. It has a larger influence on the total density of small particles than on large ones, so that errors in the estimation of the ligand properties have a more pronounced effect on the calculated size of smaller particles.

Further possible error sources in FFF are slightly different elution behaviors of the calibration particles and the deviation of particles from spherical shape. The shape has an influence on both the diffusion and the coefficient of friction.

Colloidal methods vs. electron microscopy

In this study, I analyzed ~ 500 particles for each steel by manual TEM image analysis and $\sim 1000 - 2000$ particles with the automatic image analysis in STEM [145]. This number is too low to obtain statistically meaningful data (section 1.4.1). In the manual image analysis of steel C, for example, a relatively small number of large particles is found and no exact statement about the mode or other characteristics can be made for this fraction, while in contrast colloidal methods analyze very large amounts of particles on the order of 10^9 for FFF and 10^{10} for AUC.

Analytical ultracentrifugation and field-flow fractionation are fractionating sizing methods: FFF first separates the particles into different size classes and then measures the size of the single particle fractions by ensemble measuring techniques such as UV-Vis; AUC measures time-dependent relative fractionation during the experiment. This allows the analysis of a markedly increased number of particles compared to electron microscopy; however, the gain in statistical significance is associated with a reduction of information on the particle morphology and composition.

The colloidal sizing methods are useful in determining relative differences in the PSD and thus are particularly suitable for monitoring or optimizing the thermomechanical rolling process of a steel. In combination with TEM, which provides information on the morphology and composition, the matrix dissolution technique with colloidal methods allows a comprehensive characterization of the extracted particles.

The following sections discuss specific challenges that occurred in the colloidal analysis of particles extracted from steels:

- The surfactant introduced during particle extraction influenced the size and density of the particles.
- The complex composition and morphology of the particles complicated the analysis.
- AUC and FFF provided extinction-weighted distributions, while electron microscopy provided number-weighted distributions.

4.1.3 Size and density of the ligand shell

The surfactant introduced during particle extraction adsorbs on the surface of the Nb and Ti carbonitride particles. It forms a polymer shell around the particles, which stabilizes the particles and prevents their agglomeration. The thickness and density of the ligand shell was estimated using gold reference particles. Particles with nominal diameters of 5, 15, 20, 30, 50, and 80 nm were coated with Disperbyk-2012. The coated and uncoated particles were characterized by batch DLS, AUC, and TEM that allowed the estimation of the ligand size and density.

Dynamic light scattering

Batch DLS measurements of the different particles with and without Disperbyk-2012 coating were performed. The mean hydrodynamic diameters of both coated and the uncoated particles (particle core size) were determined using cumulant analysis and plotted against each other (Figure 4.2 a).

The hydrodynamic diameter of the coated particles increased linearly with increasing hydrodynamic diameter of the uncoated particles. The ligand shell thickness was determined using a linear fit with a slope of 0.99 and a coefficient of determination of 0.998, which indicated constant shell thickness. The y-intercept was at 11.1 nm ± 0.9 nm, which corresponds to twice the thickness of the ligand shell. The uncoated particles were stabilized with a citrate shell with a size of approximately 0.4 to 0.7 nm [146] that I neglected.

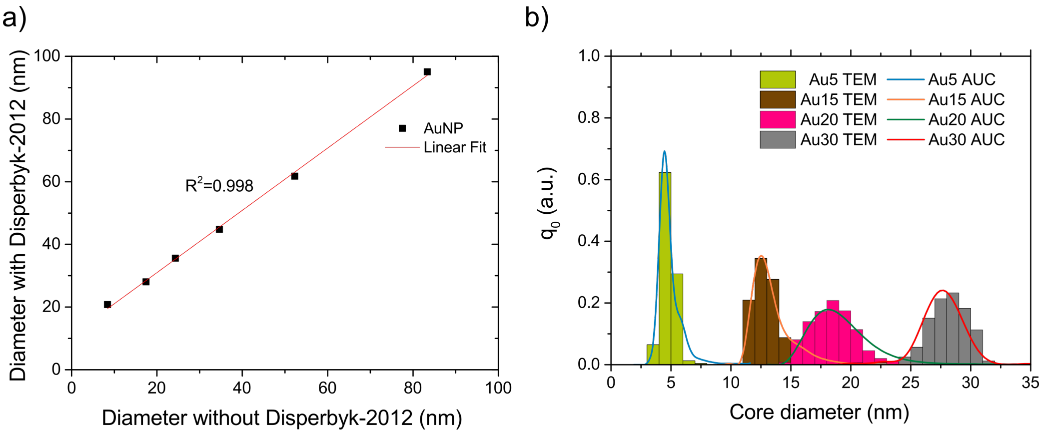

Figure 4.2: Determination of size and density of Disperbyk-2012 ligand shell: a) Hydrodynamic diameter of coated Au reference nanoparticles in dependency of the hydrodynamic diameter of the uncoated particles. The hydrodynamic diameter increases linearly with increasing diameter of the uncoated particles. b) Number-weighted PSD of gold nanoparticles with sizes of 5, 15, 20, and 30 nm measured with TEM and AUC. For the AUC measurement, the PSD was transformed from mass-weighted into number-weighted and the ligand shell thickness was subtracted.

Analytical ultracentrifugation

Gold reference particles with nominal core diameters of 5, 15, 20, and 30 nm and coated with Disperbyk-2012 were analyzed by means of AUC. Sedimentation velocity runs were performed to estimate the thickness and density of the Disperbyk ligand shell. The following procedure was performed using a Python code:

1. The sedimentation coefficient distributions were measured for all individual particle sizes.
2. The sedimentation coefficient distributions were converted into extinction-weighted size distributions assuming a thickness t_{ligand} and density ρ_{ligand} for the ligand.
3. Mie scattering was neglected (small particle size) and the extinction-weighted distributions were assumed to be equal to the mass-weighted distributions[2], which were further converted into number-weighted distributions.

---

[2] Mie calculation showed a maximum scattering contribution of 6 % for Au particles with a size of 30 nm at a wavelength of 280 nm.

4. The median of the number-weighted distribution was then compared with the median of the number-weighted distribution measured with TEM. To estimate t_{ligand} and ρ_{ligand}, these two parameters were varied in step two in order to minimize the difference between the median measured with AUC and TEM for all four particle sizes.

The best fit was achieved with the thickness $t_{\text{ligand}} = 5.74\,\text{nm} \pm 0.61\,\text{nm}$ and the density $\rho_{\text{ligand}} = 1.25\,\text{g/cm}^3 \pm 0.11\,\text{g/cm}^3$. The different statistical characteristics of the PSD measured with AUC and TEM are given in Table 4.2. Figure 4.2 b shows the core size distribution of the different Au-reference particles measured with TEM and AUC.

	method	mean	stddev	median	modal	x_{10}	x_{90}
Au5	TEM (nm)	4.78	0.50	4.77	4.71	4.19	5.32
	AUC (nm)	5.22	0.95	5.01	4.83	4.40	6.40
Au15	TEM (nm)	13.02	1.17	12.88	12.38	11.7	14.66
	AUC (nm)	13.69	1.77	13.4	12.79	12.02	16.16
Au20	TEM (nm)	18.65	2.16	18.46	18.78	16.09	21.10
	AUC (nm)	19.65	2.75	19.2	18.45	17.05	23.44
Au30	TEM (nm)	28.05	1.71	28.11	28.2	26.07	30.16
	AUC (nm)	28.02	2.49	27.98	27.98	25.85	30.29

Table 4.2: Statistical characteristics of the number-weigthed PSD of the reference gold nanoparticles measured with AUC and TEM.

Figure 4.2 b and Table 4.2 show that the size distributions measured with AUC and TEM were in very good agreement.

The ligand size estimated with AUC/TEM was consistent with the size of the ligand shell measured in batch DLS and both methods resulted in a thickness of the ligand layer of approximately 5.5 - 6 nm.

4.1.4 Particle composition and morphology

The particles extracted from the microalloyed steel samples had complex compositions and irregular shapes, which influenced the sedimentation and extinction properties of the particles. TEM analysis of the particles (Figure 4.3) revealed that steel A mainly contained particles with cubic shapes. The shapes of the particles from steel B and steel C were not uniform and included spherical and irregular angular shapes. A more detailed investigation is given in appendix B.2.

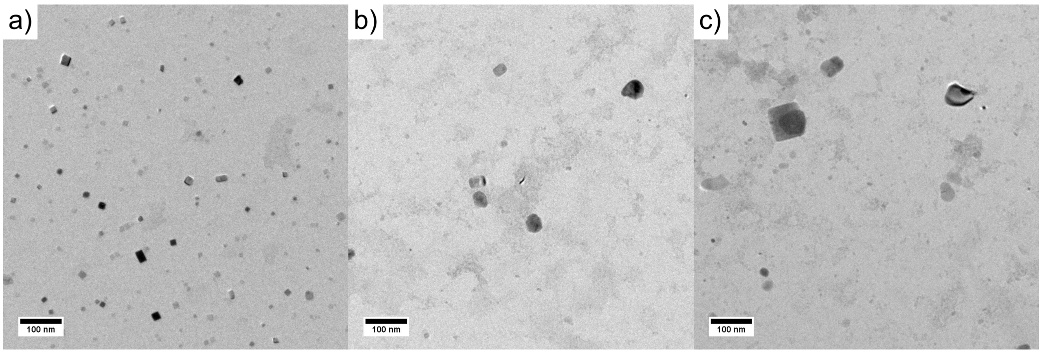

Figure 4.3: TEM overview of particles extracted from a) steel A, b) steel B, and c) steel C.

Influence on the PSD measured with AUC

In AUC analysis, the sedimentation coefficient distribution is converted into a PSD assuming a certain density (see section 3.2.2). The density directly determines the sedimentation velocity (see equation (3.29)) and thus the size distribution. Due to the mutual solubility of the microalloy carbonitrides, the composition of the particles may vary between NbC ($\rho_{\mathrm{NbC}} = 7.8\,\mathrm{g/cm^3}$), NbN ($\rho_{\mathrm{NbN}} = 7.3\,\mathrm{g/cm^3}$), TiC ($\rho_{\mathrm{TiC}} = 4.9\,\mathrm{g/cm^3}$) and TiN ($\rho_{\mathrm{TiN}} = 5.4\,\mathrm{g/cm^3}$)[72].

In order to evaluate the magnitude of the resulting uncertainty, the PSDs were determined assuming the densities of the phases that are likely to occur in the steel. The densities of the pure phases and the arithmetic mean of the pure phases were used. Figure 4.4 shows the PSDs calculated with the densities of the pure phases and the average densities evaluated at a wavelength of 400 nm. Different densities resulted in a shift of the PSD.

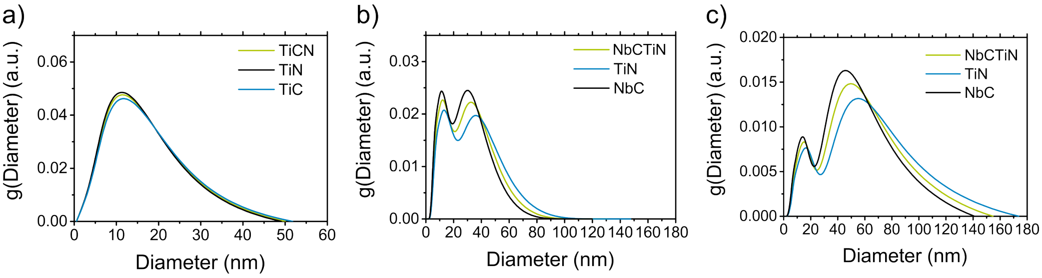

Figure 4.4: Influence of the particle core density on the calculated PSD. Particles extracted from: a) steel A with densities of TiC, TiN, and TiCN; b) steel B with densities of NbC, TiN, and NbTiCN; and c) steel C with densities of NbC, TiN, and NbTiCN.

For steel A, the PSD was calculated with the densities of the pure phases TiN, TiC, and the average density of TiCN. The densities of the pure phases only differ slightly from each other and thus the shift in the PSD was negligible.

In steels B and C, which both contained Nb and Ti, the size distributions were calculated for TiN, NbC, and NbTiCN (average of TiN and NbC). For small particles in the size range of 10 nm, the shift was only on the order of some nanometers and can be neglected. For larger particles, however, the shift was more pronounced and was approximately 10 nm for particles with diameters of 50 nm. But particles composed of only one pure phase rarely appear in these microalloyed steels, where most particles are mixed NbTi-carbonitrides. The densities of the pure phases represent extreme examples. Thus, using the average density of the pure phases reduces the maximum error in the determined size.

The apparent particle size distribution is also affected by the particle shape. AUC measures the sedimentation velocity of the particles and provides the diameter of a sphere with the given density. The sedimentation velocity and the derived sizes of the extracted particles tend to be shifted to smaller sizes due to enhanced frictional effects of the shape anisotropic particles.[85]

Influence on UV-Vis extinction

The extinction spectra of the particles depend on their composition and shape. The complex refractive indices vary significantly among the individual microalloy carbonitrides that can occur in the steel. The wavelength-depended complex refractive indices for the different phases are given in Table 4.3.

Wavelength	n_{TiN}	n_{NbC}	n_{TiCN}	n_{NbTiCN}
280 nm	$2.32 + 1.15i$	$2.40 + 1.71i$	$2.31 + 1.63i$	$2.36 + 1.43i$
350 nm	$2.14 + 0.96i$	$2.32 + 1.64i$	$2.34 + 1.63i$	$2.23 + 1.30i$
400 nm	$1.89 + 0.76i$	$2.31 + 1.71i$	$2.35 + 1.54i$	$2.10 + 1.24i$
450 nm	$1.37 + 0.85i$	$2.07 + 2.25i$	$2.18 + 1.59i$	$1.72 + 1.55i$
529 nm	$0.85 + 1.54i$	$2.16 + 2.06i$	$1.99 + 1.95i$	$1.50 + 1.80i$
629 nm	$0.68 + 2.28i$	$2.09 + 2.34i$	$1.97 + 2.37i$	$1.39 + 2.31i$

Table 4.3: Complex refractive indices of TiN, NbC, TiCN (arithmetic mean of TiN and TiC), and NbTiCN (arithmetic mean of TiN and NbC). The refractive indices for the individual wavelengths were obtained by linear interpolation.[147]

The wavelength-depended extinction of the individual phases directly depend on the refractive indices and thus differs for the individual phases. Figure 4.5 a shows the extinction efficiencies of NbC and TiN particles with diameters of 10 and 50 nm. Both phases show an increased extinction efficiency at short wavelength, but only TiN has an increased extinction efficiency at wavelengths at around 600 to 650 nm, while the extinction efficiency of NbC is low.

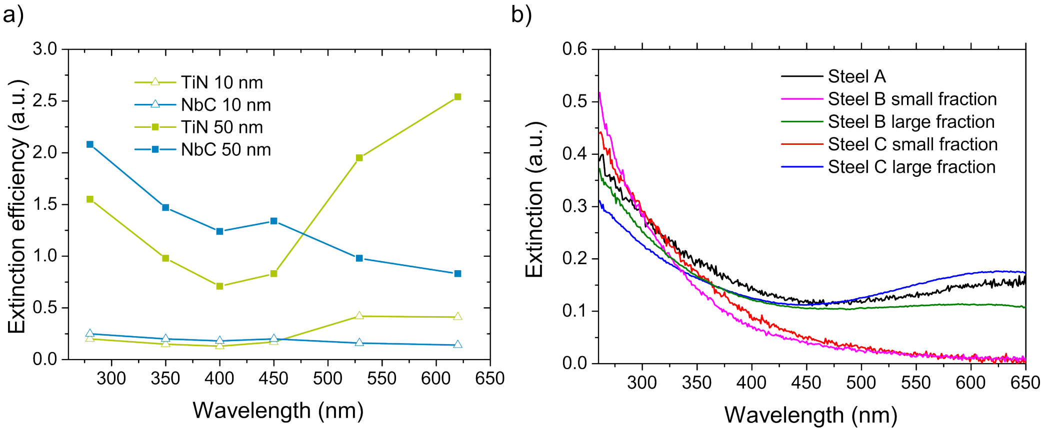

Figure 4.5: Particle fraction dependent extinction: a) Extinction efficiencies for TiN (gree) and NbC (blue) particles with sizes of 10 (hollow symbols) and 50 nm (filled symbols) calculated with the refractive indices from Table 4.3. b) Extinction spectra of the individual particle fractions from the different steel samples.

The MWL-AUC measures the sedimentation of the particles using all wavelengths between 250 and 700 nm. This allows the determination of the extinction spectrum for every single particle fraction (Figure 4.5 b) and gives insights into the chemical composition. All particles showed a more pronounced extinction at shorter wavelengths. To a certain amount, this is probably caused by the dispersing agent, which absorbs in the UV region. At longer wavelengths the extinction of the particles extracted from steel A increases again, as does the extinction of the large particle fraction extracted from steel B and C. They all contain TiN. The small particle fractions extracted from steel B and C are composed of NbC and do not show an increase in extinction. In contrary, their extinction is almost zero at large wavelengths. This coincides very well with the wavelength-depended extinction efficiencies ϵ_λ calculated for NbC and TiN particles (Figure 4.5 a).

4.1.5 Prospects and limits of colloidal particle sizing

Both AUC and FFF proved to be useful colloidal analysis methods that rapidly cover a statistically meaningful number of particles extracted from steel. Combining the matrix dissolution with colloidal sizing enables the characterization of particle numbers on the order of 10^9 compared to regular TEM analysis that usually analyzes $< 10^3$ particles.

The qualitative comparison of the PSDs from the extracted particles measured with AUC, FFF, and TEM showed good agreement with the PSDs of the particles on the extraction replica measured with STEM: all methods retrieved the same amount of particle fractions and indicated the same size ranges.

While TEM and STEM provide number-weighted PSDs, AUC and FFF provide extinction-weighted PSDs. A transformation into mass and number-weighted PSDs is not possible due to the lack of information for Mie correction. A quantitative comparison to electron microscopy data is therefore not possible. However, colloidal methods provide data from a large number of particles which can be used, for example, for process and product control or optimization to monitor changes in the PSD caused by changes in the steel processing.

4.2 Composition analysis by single particle inductively coupled plasma mass spectrometry[3]

The chemical composition of the particles is of interest for steel processing, too. It gives further insides into the time of formation during the TMCP and indicates whether the alloying elements precipitate as expected. The suitability and limits of single particle mass spectrometry to particles extracted from microalloyed steel was studied. The microalloyed steel analyzed here was alloyed with Nb and Ti. The chemical composition is given in Table 4.4. Note that only Nb and Ti containing precipitates were found, although V is a potential carbide and nitride former. Only traces of V were found. The processing conditions and the alloy design limited the formation of V containing precipitates to negligible amounts, orders of magnitude below that of Nb and Ti carbides, nitrides, and carbonitrides.

---

[3] Parts of this chapter were submitted for publication in a manuscript entitled "Single particle mass spectrometry of titanium and niobium carbonitride precipitates in steels" by Andreas Hegetschweiler, Olga Borovinskaya, Thorsten Staudt, and Tobias Kraus.

Element	C	Si	Mn	N	Cr	V	**Nb**	**Ti**	CEV
wt%	0.07	0.35	1.9	0.003	0.2	0.04	**0.05**	**0.02**	0.44

Table 4.4: Elemental composition of the examined steel. Cu, Ni, and Mo were not alloyed.

4.2.1 Experimental procedures

Extraction

Niobium and titanium carbonitride particles were extracted by dissolving 1 g of steel in 0.05 L of an etching solution containing 0.5 mol/L sulfuric acid and 0.1 vol% Disperbyk-2012. The solution was heated to 70 °C and stirred at 200 rpm. After dissolution was completed, all samples were sonicated for 1 min in an ultrasonic bath (Elma X-tra 50 H, 160 W, Germany). Subsequently, the particles were separated from the dissolved iron matrix by centrifugation (Beckman Coulter, XL-I 70K, Germany) at 113 000 rcf for 8 h. The supernatant was removed (20 mL), the particles were redispersed in an ultrasonic bath, and the removed supernatant was replaced with fresh UPW. A total of 8 centrifugation cycles completely removed the dissolved iron matrix. After the last centrifugation run, the supernatant was removed and no water was added in order to obtain samples with highest possible particle mass concentration (c(Nb)≈ 25 mg/L, c(Ti)≈ 13 mg/L, measured with ICP-OES, see chapter 2) to reach a high particle area density in electron microscopy.

Analysis

Electron microscopy

The particles were imaged using a *JEM-ARM200F* Scanning Transmission Electron Microscope (STEM) operating at 200 kV equipped with a *JED-2300 Analysis station* EDX system (JEOL, Germany). To prepare samples for STEM, a droplet (2.5 µL) of the particle suspension was dried on a TEM copper grid coated with an amorphous carbon film and the grid was introduced to the STEM without further preparation. Around 25 images were taken until a total of 174 particles had been imaged. The particle size was evaluated with the FIJI software [144] by determining the diameter of a circle of the same area. The average composition of a particle was examined by EDX point analysis, where the beam was placed in the center of the particle. The total measure time per particle was 30 s. To estimate the relative chemical composition of the particles, the X-ray counts at the Nb-L_α and the Ti-K_α peak were compared. Note that this is only a relative measurement.

There are no reference materials available with appropriate chemical composition and geometries to perform the necessary ZAF-correction of the X-ray intensities with respect to material dependent X-ray radiation intensity (Z), absorption by the sample itself (A), and the fluorescence induced by X-ray radiation (F).

ICP-TOF

An icpTOF mass spectrometer (Tofwerk, Switzerland) was used to analyze single particles at Tofwerk in Thun, Switzerland. The mass spectrometer comprises inductively coupled plasma source, ion optics components (Thermo Fischer Scientific, Germany), and an orthogonal-acceleration time-of-flight mass analyzer with a mass resolving power of 3000 m/Δm (Th/Th) (where Δm is defined as full width at half maximum of the peak with the mass m) and ion extraction frequency of 33 kHz (Tofwerk, Switzerland). Single particle data was collected at 500 spectra/s that corresponds to an integration time of 1.8 ms. A pneumatic nebulizer and a cyclonic spray chamber were utilized for the analysis.

The particle dispersions were diluted by a factor of 10^5 with ultrapure water (Merck Millipore, USA). Element masses in individual particles were quantified using the method described by Pace et al.[128] Transport efficiency determination method based on the known size of calibration particles was applied.[128] Calibration of the instrument element-specific sensitivity was performed with a multi-element standard solution containing Nb (Spex CertiPrep, USA) and Ti single element standard solution (TraceSelect Ultra, Merck, NJ, USA) in 1% HNO_3 in the concentration range of 0.05 to 100 µg/kg. Ideally, standard element solutions have to be prepared in the same media as the sample [119], but Nb was not stable in water and 1% HNO_3 was added for stability. The sensitivity of Ti was not different for UPW and 1% HNO_3 in UPW; the influence of acid matrix on the sensitivity of Nb could not be verified. Data post-processing was carried out using the Tofware program (version 2.5.10, www.tofwerk.com/tofware) running in the Igor Pro (Wave-metrics, OR, USA) environment and using Microsoft Excel. ^{48}Ti and ^{93}Nb isotopes were used to calculate the element masses. Particle signals were discriminated from the background noise using intensity threshold Θ defined as $\Theta = \mu + 5 \cdot \sigma$ with the mean value μ and the standard deviation σ. Mean and sigma were determined by fitting intensity distribution histogram of noise of every isotope with a Gaussian distribution.

Particles where only the number of Nb ions was above the threshold (2-3 ions) were treated as pure NbCN, while particles where the amounts of both Nb and Ti ions were above the threshold were treated as TiNbCN particles. Every particle signal was converted to element mass and the mass of the compound was calculated as $f \cdot (m(\mathrm{Ti}) + m(\mathrm{Nb}))$, where f is a factor to correct for the fraction of C and N which is not measured. Diameters were calculated assuming that particles are spherical. For the NbCN particles, the density required for size calculation was assumed to be $7.6\,\mathrm{g/cm^3}$ (the mean of the densities of pure NbC and NbN). The densities ρ of TiNbCN particles were calculated for every individual particle with the composition $\mathrm{Ti}_x\mathrm{Nb}_{(1-x)}\mathrm{CN}$ as $\rho = x \cdot \rho_{TiN} + (1-x) \cdot \rho_{NbCN}$. TiC was neglected as a component of these particles, as it is very unlikely to occur in this alloy design. The densities of the pure phases are $\rho_{NbC} = 7.8\,\mathrm{g/cm^3}$, $\rho_{NbN} = 7.3\,\mathrm{g/cm^3}$, and $\rho_{TiN} = 5.4\,\mathrm{g/cm^3}$.[72]

4.2.2 Composition and size analysis

Figure 4.6 shows a TEM micrograph of the well-dispersed particles after extraction and the EDX spectra of selected particles. The particles had a broad size distribution ranging from a few nanometers up to several hundred of nanometers. I found no predominant particle shape, but a mix of spherical and angular particles. Larger particles often had a heterogeneous structure (Figure 4.6 c) with a core of TiN and caps of TiNbCN.

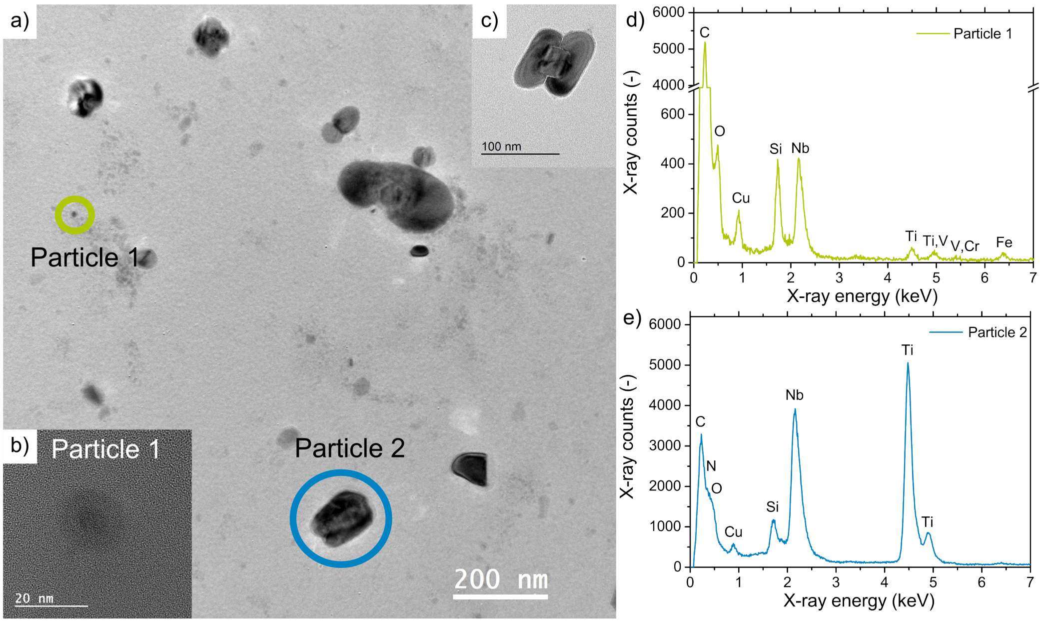

Figure 4.6: Transmission electron microscopy analysis of extracted particles: a) Overview image. b) High resolution image of particle 1. c) Complex particle with a TiN core and a NbCN shell. d) EDX signal of particle 1 (mainly containing Nb). e) EDX signal of particle 2 (containing both Nb and Ti).

Electron-dispersive X-ray analysis revealed two different populations: particles that mainly contained niobium (referred to as “Nb-particles” in the text) and particles that contained titanium and niobium (referred to as “TiNb-particles” in the text). The relative particle composition, determined as the ratio of the number of X-ray counts of the Nb-L_α peak to the Ti-K_α peak, is plotted against the particle size in Figure 4.7. Most particles with diameters below 49 nm had a peak ratio Nb-L_α/Ti-K_α > 3.5 (Nb-particles), while most particles with diameters above 49 nm had a peak ratio Nb-L_α/Ti-K_α < 3.5 (TiNb-particles). The threshold was chosen such that a maximum of particles (91 %) belonged to one of the two groups. Note that the peak ratio is not directly proportional to the composition ratio, but helps to classify the particles.

	Nb			TiNb		
	mean	stddev	median	mean	stddev	median
STEM	28 nm	20 nm	22 nm	86 nm	31 nm	80 nm
SP-ICP-MS	38 nm	11 nm	34 nm	91 nm	28 nm	84 nm

Table 4.5: Statistical values on the PSD measured with STEM and SP-ICP-MS.

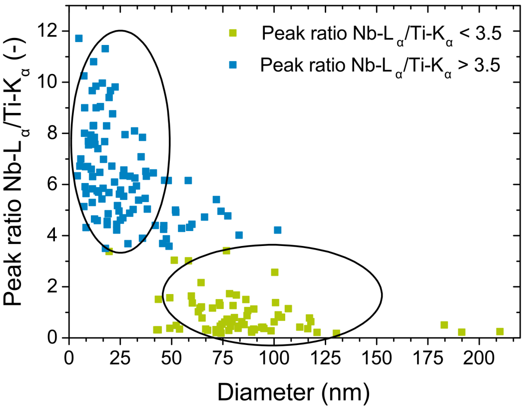

Figure 4.7: Peak ratio of peak ratio Nb-L_α/Ti-K_α > 3.5 depending on particle size. Note the populations of particles with Nb-L_α/Ti-K_α > 3.5 (“Nb-particles”) and particles with a peak ratio Nb-L_α/Ti-K_α < 3.5 (“TiNb-particles”).

Particle size distribution

Particle analysis in STEM was performed on a total of 174 particles, 108 of which were Nb-particles and 66 were TiNb-particles. Particle analysis with SP-ICP-MS was orders of magnitude faster than using STEM. 2098 particles were analyzed with SP-ICM-MS in 1 min (1595 were Nb-particles and 503 were TiNb-particles), while 174 particles were analyzed with STEM within 2 working days. The particle size distributions from STEM and SP-ICP-MS are illustrated in Figure 4.8. The statistical characteristics such as mean, standard deviation, and median of the two different particle classes are given in Tables 4.5. It would be very time consuming to produce a particle size distribution using STEM that reaches similar particle numbers as the one shown in Figure 4.8 f.

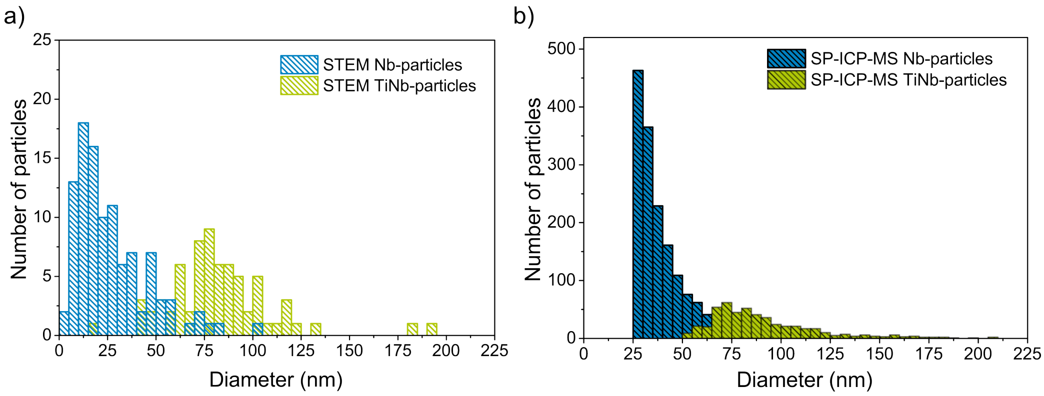

Figure 4.8: Particle size distributions of Nb-particles and TiNb-particles measured with a) STEM and b) SP-ICP-MS.

The mean and median diameters measured with STEM and SP-ICP-MS are in very good agreement. Both were slightly smaller for STEM because the limit of detection (LOD) for SP-ICP-MS is above that of STEM. In STEM, particles with diameters down to a few nanometers could be observed at the chosen magnification, while the LOD in SP-ICP-MS was 26.5 nm for Nb-particles and 46.6 nm for TiNb-particles. A significant fraction of the Nb-particles had sizes below the detection limit of SP-ICP-MS so that the PSD was cut off at 26.5 nm and the average diameter was biased towards greater values. All TiNb-particles were above the detection limit of SP-ICP-MS and their size distribution was not biased. Note, however, that there may be smaller TiNb-particles containing an amount of Ti below the SP-ICP-MS detection limit, which could be counted as Nb-particles rather than TiNb-particles.

The resolution of STEM at high magnifications is sufficient to see any particle down to the atomic cluster scale. In practice, however, small particles have insufficient contrast over the carbon film and tend to be undercounted.[49, 148] The contrast of particles depends on the crystallographic orientation and the thickness of the particles. If particles are oriented such that the electrons are not diffracted, the contrast is lower than for particles with an orientation that causes diffraction. Larger particles scatter electrons more strongly than small particles (mass-thickness contrast) and they may obscure very small particles in their vicinity. In practice, this effect is exacerbated by the automatic contrast function of the camera. Particles extracted from steel have a wide size distribution, which requires a compromise in the choice of magnification. This can further complicate the detection of the smallest particles unless image series with different magnifications are used. The size distributions shown in Figure 4.8 a and b indicate a lower ratio of

Nb-particles to TiNb-particles for STEM than for SP-ICP-MS. The reason is likely to be a lower probability of detection for smaller particles in STEM due to the reasons discussed above.

A second difference between the two sizing methods pertains to particle shapes. Electron micrographs show 2D projections of each particle. Particle sizes are calculated by determining the diameter of a circle with the same area as the projection (projection area-equivalent diameter). Diameters from mass spectrometry were calculated as the third root of the measured particle mass (mass-equivalent diameters), i.e. the diameter of a volume-equivalent sphere of the same density. Particle shapes that deviate from spheres will cause independent errors for both methods; since particles extracted from steel are rarely perfect spheres, this will lead to differences in the PSD measured with STEM and SP-ICP-MS.[85]

Chemical composition

I found 17 wt.% of the Nb and 18 wt.% of the Ti that were alloyed in the steel in the particles with SP-ICP-MS. It is known that there are losses of Nb and Ti particles associated to the extraction process (chapter 2). Inductively coupled optical emission spectroscopy indictated that after the centrifugation process the particle suspension only contained 52 wt.% of the initially alloyed Nb and 72 wt.% of the Ti. Of this amount, 25 to 30 wt.% were found by SP-ICP-MS, which means that 70 to 75 wt.% of the investigated particles were lost during SP-ICP-MS analysis. I believe that some particles are lost inside tubing and other surfaces (e.g. vials used for dilution) as reported in literature for SP-ICP-MS.[149, 150] The inter-laboratory comparison study showed that the particle number concentration of even well-defined standard particles can deviate from the true concentration by an order of magnitude depending on the laboratory hardware. Particle losses in the system are sample specific. To quantify these losses is a challenge because it requires a standard system equivalent to the sample, which is rarely available, especially for such complex particles as characterized in this study.[151] To obtain the absolute particle number concentration independent complementary methods are required. Here, I used ICP-OES analysis to measure the content of Nb and Ti in the specimen.

Another error source might be the LOD of the SP-ICP-MS, since small particles are likely not be detected and thus not considered in the size distribution. Finally, C and N could not be quantified in SP-ICP-MS and I assumed the stoichiometry of TiNb-particles to be TiNbCN, which may lead to errors in the calculated sizes if the true particle composition deviated.

Both STEM and SP-ICP-MS can provide the chemical composition of particles. Chemical analysis via EDX or EELS in the electron microscope record detailed information on chemical composition even for complex particles with heterogeneous structures. However, quantitative analysis requires calibration standards with geometries similar to the analyzed particles and defined compositions that may not be readily accessible. Particles with broad size and chemical composition distributions require multiple standards and cumbersome calibration. The effort involved typically allows for only a small number of particles to be analyzed and limits the statistical relevance.

In contrast, the advanced mass spectrometry used here can provide the absolute Nb and Ti contents of each individual particle. Figure 4.9 a shows that most TiNb-particles contained approximately 40-50% Nb and 50-60% Ti, with broad concentration distributions and no typical composition. The precision of the method is limited by counting statistics which defines the maximum precision achievable with a certain number of detected ions. The theoretical variation of the signal ratios expected from average number of counts detected for Ti and Nb was estimated to be 34%. The measured Ti/Nb precision in TiNbCN particles was 80%. Approximately 50% of this variation can be assigned to actual variations of the Ti/Nb composition ratio in different particles. Figure 4.9 b shows the PSD of TiNb-particles and their corresponding composition as determined by SP-ICP-MS. The Ti content was higher for smaller particles. The Ti and Nb contents of larger particles were broadly distributed, without any discernible maxima.

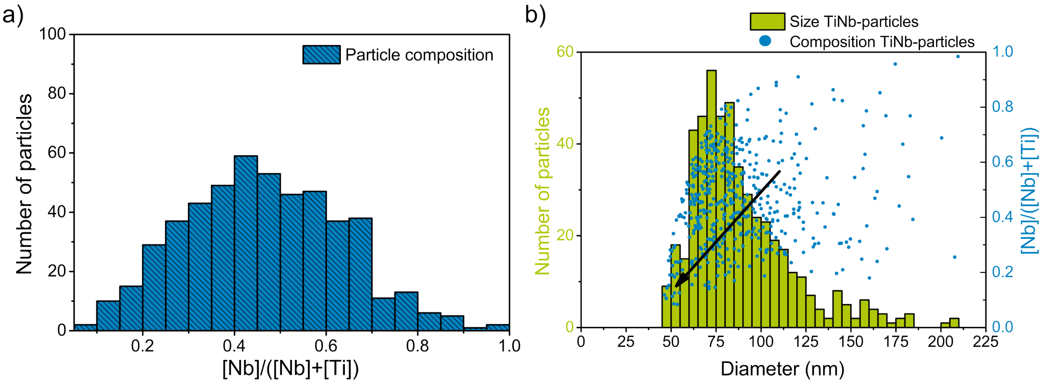

Figure 4.9: Chemical composition of particles from steel as measured by SP-ICP-MS. a) Relative Nb content in particles that contain both Nb and Ti. b) Size distributions (green) and Nb content (blue) of particles containing both Nb and Ti.

Both Nb and Ti are readily detected using SP-ICP-MS and electron microscopy, while the quantification of C and N is more challenging. The detection limits for C and N are currently insufficient for single particle detection with ICP-MS. Electron microscopy can indicate such elements using EDX or EELS analysis, but the resulting C and N contents are influenced by the dispersant introduced during the extraction procedure that contains carbon and nitrogen. Furthermore, the amorphous carbon film on the copper TEM grid contributes strongly to the detected C signal. Hence, neither SP-ICP-MS nor electron microscopy are currently suitable for a detailed analysis of the carbon and nitrogen content of the precipitates; new methods with higher resultion in MS or electron-transparent foils may resolve this limitation in the future.

Metallurgical considerations

Niobium carbonitride particles in the size range of $\sim 10^1$ nm contribute to grain refinement during rolling (strain induced precipitates) and at the $\gamma - \alpha$ transition (precipitation at $\gamma - \alpha$ phase boundary)[15]. Larger particles in the size range of $\sim 10^2$ nm that precipitate at the γ-grain boundaries are often composed of a TiN core and TiNbCN caps. According to Craven et al.[39], these particles do not greatly contribute to the mechanical strength of the steel. The caps increase the size of the TiN particles, diminishing their effectiveness for grain refinement during austenite conditioning, and the Nb in the caps is not available for later precipitation hardening. The SP-ICP-MS measurements found 12 wt.% of the alloyed Nb in such large particles, while only 5 wt.% of Nb was found in pure Nb-particles. Assuming a uniform particle loss during extraction independent of size and composition on the order of 50 wt.% for Nb (as discussed above), the quantity of Nb in "large" TiNb-particles can be estimated to be at least 23 wt.% of the total amount of alloyed Nb and is likely to be even higher, since losses during SP-ICP-MS are not corrected. This part of the alloyed Nb does not contribute to mechanical strengthening and indicates potential for improvement in the TMCP.

The SP-ICP-MS measurements indicated pure NbCN, but almost no pure TiCN particles. I believe that TiN particles are efficient nucleation sites for NbCN precipitation, which is consistent with literature.[39, 40] The high Ti content of rather smaller TiNb-particles (Figure 4.9 b) is probably due to small amounts of NbCN that nucleated on these TiN nuclei particles and only formed small caps. The TiN nuclei particles must have a size above 50 nm. It is unclear whether the TiNbCN particles that I found are homogeneous or have a TiN core and NbCN caps. Additional STEM analysis is necessary to provide this information.

4.2.3 Prospects and limits of single particle mass spectrometry

I extracted Nb and Ti carbonitride particles from microalloyed steel and analyzed their size and composition distribution by means of SP-ICP-MS and electron microscopy. Particles from microalloyed steel alloyed with Nb and Ti could be graded into two size populations: particles with diameters below 49 nm that were mainly composed of Nb and particles with diameters above 49 nm that were composed of $Ti_xNb_yC_qN_r$ with a wide composition range. The smallest particles that could be detected in SP-ICP-MS were 26.5 nm in diameter and contained only Nb; the smallest detected particles with both alloying elements were 46.6 nm in diameter.

The size distributions obtained with SP-ICP-MS and electron microscopy were similar with a bias towards larger Nb particles for SP-ICP-MS. Electron microscopy analysis of 174 analyzed particles required approximately two days, while the SP-ICP-MS analysis of 2098 particles was finished after 1 min. While the chemical analysis with (S)TEM requires particle calibration standards, SP-ICP-MS provided the Nb and Ti contents that could be used to understand which microalloy elements precipitate during which stage of the TMCP. I found that at least 23 wt.% of the alloyed Nb precipitated in TiNb-particles that do not have a positive effect on the steel properties.

SP-ICP-MS enables size and composition distribution analysis with high statistical relevance. However, SP-ICP-MS is still limited to relatively large particles and it cannot provide information on the shape and morphology of the particles. Combining SP-ICP-MS analysis with electron microscopy and preferable with other complementary methods as bulk OES analysis is required to provide a complete analytical picture of the particles.

Single particle mass spectroscopy can quantify other elements such as vanadium, molybdenum, aluminum, among many others [127] and is therefore relevant for small particles in other relevant alloys such as aluminum. Its application requires successful extraction of the particles by matrix dissolution; the particle size detection range of SP-ICP-MS has a lower limit of $\approx$ 5 to 100 nm that is element-dependent and an upper limit of $\approx$ 1 µm that is due to saturation of the detector of the instrument used in this study. For example, the LOD of Al-particles is reported to be 70 nm [127] and Al_2O_3-particles with a size of 150 nm were successfully analyzed [115]. The reported LOD for other relevant alloying elements is even lower: Vanadium has a LOD of about 40 nm, Molybdenum approximately 30 nm.[127, 151] The method therefore holds promise for many other engineering materials.

Chapter 5

Conclusions and outlook

5.1 Conclusions

In this thesis, I developed an analysis routine for the colloidal analysis of Nb and Ti carbonitride particles extracted from microalloyed steels. The thesis focused on two main topics: first, the development of an extraction protocol that provides particles in a state suitable for subsequent analysis; second, the colloidal analysis of the particles with regard to their size distribution and chemical composition. Different analytical methods were examined for their ability to characterize the particles extracted from microalloyed steels.

I found that the choice of extraction protocol is important to obtain reliable measurements. The etchants used for matrix dissolution can attack the targeted precipitates and (partially) dissolve them. Additionally, Si, which is alloyed to the steel, can form SiO_x during the extraction, form a gel, or a dense network that impedes the analysis of the particles. Existing particle extraction protocols were investigated for their suitability to extract the targeted Nb and Ti carbonitride precipitates. Based on the existing protocols, modified extraction protocols were developed providing better extraction results. The extraction protocols were analyzed regarding the loss of particles and the formation of silica network during the extraction. To this end, I analyzed the amount of Nb, Ti, and Si after extraction in the supernatant and in the residue. Additionally, Nb and Ti carbonitride reference particles were synthesized to verify the particle etching.

There are trade-offs with regard to particle etching, dissolution speed of the steel matrix, and silica network formation. Higher acid concentrations and higher temperatures sped up extraction and reduced the formation of SiO_x networks, but also increased particle etching. Even the best protocols lead to particle etching. This can cause a reduction of the true particle diameter on the order of 5% that should be reported when using such methods.

Adding the dispersant *Disperbyk-2012* to the extraction solution readily improved the extraction result by stabilizing the particles without decreasing the extraction yield. There are indications that the surfactant stabilizes even very small particles with diameters below 10 nm, making them accessible to characterization techniques beyond electron microscopy. I found an optimized extraction protocol using a 0.5 mol/L H_2SO_4 solution containing 0.1 vol.% Disperbyk-2012 and a dissolution temperature of 70 °C. It reduced particle etching to 11% for Nb and 18% for Ti. Long centrifugation times above 20 h (at 113 000 rcf) are recommended to remove most of the smallest particles from the extraction suspension.

The second part included the analyis of the extracted particles by means of colloidal analyis methods and electron microscopy. Colloidal methods rapidly analyze a large number of particles compared to TEM and provide statistically meaningful data in a short time. I analyzed the extracted particles with analytical ultracentrifugation (AUC), field-flow fractionation (FFF), and single particle mass spectrometry (SP-ICP-MS) and compared the results to data obtained by TEM.

First, I studied different colloidal methods for their suitability to analyze broad, multimodal particle systems regarding their size distribution. I prepared different model particle mixtures with well-known multimodal size distributions and analyzed them with AUC, FFF, and DLS. AUC and FFF showed great potential to analyze such broad, multimodal particle mixtures, while DLS was not suitable. The first two methods were then used to analyze the particle extracted from steels.

Large number of particles ($> 10^9$) extracted from steel were successfully analyzed using AUC and FFF. The number of particle fractions and corresponding sizes of the fractions were in very good agreement with data obtained from TEM analysis of the extracted particles and STEM analysis of carbon extraction replicas. However, AUC and FFF provided extinction-weighted size distributions and a conversion into number-weighted size distributions was not possible because of the complexity of the extracted particles with regard to their composition, morphology, and shape. Hence, no quantitative information on the particle number and the particle volume fraction can be provided, but FFF and AUC are particularly suitable to determine relative differences in the PSD caused by process changes or different alloy designs by analyzing a large number of particles.

For successful analysis, information on the Disperbyk-2012 ligand shell introduced during extraction process was necessary. Analysis of different sized gold reference particles coated with Disperbyk-2012 by AUC and DLS provided information on the size and the density of the Disperbyk-2012 ligand shell.

Second, I employed SP-ICP-MS for the analysis of the extracted particles. This method allows the concurrent determination of the particle size and particle composition. A time-of-flight detector allowed the analysis of several elements at a time. Thus, analysis of complex particles with compositions of NbTiCN was possible.

The particle size distribution was compared to size and composition data obtained by STEM. Both methods found two particle populations: one population with small sizes that consisted mainly of Nb-containing particles and one larger sized population that consisted of NbTi-containing particles. Compared to STEM, the size distribution obtained by SP-ICP-MS of the smaller particle fraction was biased towards larger particle sizes, because the limit of detection was above the smallest particle sizes occurring in the steel. The second particle fraction showed very good agreement with STEM data.

Both methods also allow the characterization of the particles regarding their composition. Quantitative analysis using EDX or EELS analysis in STEM requires calibration standards that are not presently accessible. Single particle mass spectrometry provides detailed information of the chemical composition of each individual particle. This information can be useful for steel development in order to achieve the desired precipitation of the microalloy elements during the thermomechanical rolling process. Furthermore, single particle mass spectrometry was much faster. While the analysis of only 174 particles lasted approx. 2 working days with STEM, SP-ICP-MS allowed the analysis of more than 2000 particles in one minute.

5.2 Outlook

The smallest particles occurring in steel with sizes below 10 nm are of great importance for strength improvement by precipitation hardening and consequently their detailed analysis is of great interest. However, their extraction and analysis have proven particular difficult. The extraction process is accompanied by losses due to particle etching and insufficient sedimentation during centrifugation. Particle etching is more likely to occur for these smallest particles due to their increased surface to volume ratio. Additionally, they are more likely to be lost during centrifugation in the frame of the extraction process due to their slow sedimentation velocity. The extraction process needs to be optimized in particular with regard to the extraction of these particles and their loss has to be minimized.

The analysis of these small particles has proved to be challenging for several reasons. In TEM, the contrast of small particles is reduced compared to larger ones and they can easily be missed. In colloidal methods that are based on optical extinction, extinction for small particles is reduced compared to larger particles and their concentration has to be high enough to be detected. Also, for small particles the ligand accounts a large amount of the particle volume. Since the used ligand absorbs light in the UV region of the light spectrum, the extinction of the particle is markedly increased and no relation to the particle concentration can be made. And finally, for SP-ICP-MS, smallest particles cannot be analyzed because their size is smaller than the limit of detection.

The extracted particles were successfully analyzed regarding their particle size distribution and chemical composition using colloidal analysis methods and electron microscopy. These data allow a better control and optimization of the TMCP. The changes in the particle size and frequency of the particles can be monitored using these methods. The changes can be related to changes of the processing parameters such as deformation degree during rolling or the alloy design. The parameters can thus be adjusted with regard to particle size distribution and mechanical properties of the steel.

The extraction procedure developed in this thesis provides free, unagglomerated particles mainly without SiO_x network engulfing the particles. I found Disperbyk-2012 working very well for particle stabilization and at the same time for suppressing silica network formation. The processes occurring during the extraction process are very complex, not completely understood, and show potential for improvement and optimization. Faster dissolution rates of the iron matrix at simultaneously lower extraction temperatures and low acid concentrations should be sought to further reduce particle etching. Further investigations regarding particle etching and the mechanism of silica network inhibition by the surfactant are required. The introduced polymer is very complex and little information about its composition and morphology are provided. A better understanding of the mechanisms for silica inhibition is required in order to make the extraction process more controllable and further improve the extraction process.

List of Symbols

C_{abs} Absorbance cross section

C_{sca} Scattering cross section

D Diffusion coefficient

E_{λ} Light attenuation

E_{kin} Kinetic energy

F_{b} Buoyant force

F_{f} Frictional force

F_{s} Gravitational force

G Shear modulus

I Transmitted light intensity

$I(t)$ Time-dependent intensity

I_0 Incident light intensity

I_{BKGD} Background intensity

I_{NP} Intensity of a single particle

L Particle spacing

N_{p} Number density of particles

$Q(x)$ Cumulative distribution

Q_{ext} Extinction efficiency

Q_{liq} Sample flow rate

R	Retention ratio
T	Temperature
T_λ	Light transmittance at wavelength λ
V^0	Void volume
V_c	Volumetric cross-flow rate
V_p	Particle volume
V_s	Solvent volume
W	Total mass of analyte entering the plasma during dwell time
$\Delta\tau_y$	Increase in yield shear stress
Γ	Decay rate
$\bar{\Gamma}$	Mean decay rate
$\bar{\nu}$	Partial specific volume of the particle
ϵ_λ	Extinction coefficient at wavelength λ
η_i	Ionization efficiency
η_n	Transport efficiency
η_s	Shear viscosity of the solvent
λ	Retention parameter
ω	Rotor spinning velocity
$\omega^2 r$	Gravitational field
ϕ	Volume fraction of particles
ρ_core	Bulk density of inorganic particle core
ρ_p	Density of the particle
ρ_shell	Density of organic ligand
τ	Decay time
τ_λ	Turbidity at wavelegth λ

θ Scattering angle

$a_{[\mathrm{MX}]}$ Activity of the constituent phase

$a_{[\mathrm{M}]}$ Activity of dissolved microalloy element

$a_{[\mathrm{X}]}$ Activity of dissolved interstitial element

b Burgers vector

c Analyte concentration

$c(r,t)$ Radial concentration profile

d Travel distance of ions to reach the detector

f Frictional coefficient

$g(s)$ Sedimentation coefficient distribution

$g^{*}(s)$ Apparent sedimentation coefficient distribution

$g^{(1)}(\tau)$ Electric field correlation function

$g^{(2)}(\tau)$ Intensity correlation function

k Wave number

k_{B} Boltzmann's constant

k_{s} Equilibrium constant

l Optical path length

m/z Mass-to-charge ratio

m_{p} Mass of particle

m_{s} Mass of displaced solvent

n Refractive index

q Wave vector

$q(x)$ Density distribution or frequency distribution

q_0 Number-weighted particle size distribution

q_3 Volume-weighted particle size distribution

r_{bnd} Radial position of sedimentation boundary

r_{b} Radial position of bottom

r_{m} Radial position of meniscus

s Sedimentation coefficient

t_0 Retention time of the void peak

t_{dt} Dwell time

t_{d} Travel time of ions to reach the detector in the distance d

t_{eff} Effective channel thickness

t_{ligand} Thickness of organic ligand

t_r Retention time of the sample

u Sedimentation velocity

w_{a} Mass fraction of the analyzed element in the particle

x Particle diameter

x_{h} Hydrodynamic diameter

σ_0 Starting stress for dislocation movement

σ_y Yield strength

d_{grain} Mean grain size

k_y Strengthening coefficient

r Distance to rotation axis

$\mathbf{G}(\Gamma)$ Distribution of decay rates

List of Abbreviations

(Fl)FFF (Flow) Field-flow fractionation

(S)TEM (Scanning) Transmission electron microscopy

(SP-)ICP-MS (Single particle) Inductively coupled plasma mass spectrometry

ADF Annular dark field

AF4 Asymmetrical flow field-flow fractionation

AFM Atomic force microscopy

APT Atom probe tomography

AUC Analytical ultracentrifuge

BF Bright field

BSE Backscattered electron

BSP Bis(p-sulfonatophenyl)phenylphosphine

CEV Carbon equivalent value

DF Dark field

disodium EDTA Disodium ethylenediaminetetraacetate

DLS Dynamic light scattering

e.g. for example

EDX Energy dispersive X-ray analysis

EELS Electron energy loss spectroscopy

EFTEM Energy filtering TEM

EM Electron microscopy

ESD Equivalent sphere diameter

fcc face-centred cubic

FIB Focused ion beam

HAADF High angle annular dark field

hcp hexagonal close-packed

HF5 Hollow-fiber flow field-flow fractionation

HSLA High strength low alloy

ICP-OES Optical emission spectroscopy with inductively coupled plasma

LM Light microscopy

LOD Limit of detection

MA Microalloyed

MWL-AUC Multiwavelength analytical ultracentrifuge

NNLS Non-negatively constrained least-squares

PCS Photon correlation spectroscopy

PEG-1000 Polyethylene glycol (M = 1 kDa)

PEG-20000 Polyethylene glycol (M = 20 kDa)

PES Polyethersulfone

PI Polydispersity index

PSD Particle size distribution

PSL Polystyrene latex

PSS Polystyrene sulfonate

RF Radio frequency

SAD Selective area diffraction

SDS Sodium dodecyl sulfate

SE Secondary electron

SEM Scanning electron microscopy

SIP Strain induced precipitation

stddev Standard deviation

TMCP Thermomechanical controlled rolling process

TOF Time-of-flight

UPW Ultrapure water

WDX Wavelength dispersive X-ray analysis

XRD X-ray diffraction

Bibliography

[1] Joseph R Davis. *Alloying: understanding the basics.* ASM international, 2001.

[2] F Brian Pickering. "High strength low alloy steels". In: *Materials Science and Technology* (2006).

[3] TN Baker. "Microalloyed steels". In: *Ironmaking & Steelmaking* 43.4 (2016), pp. 264–307.

[4] Terrence Gladman. *The physical metallurgy of microalloyed steels.* Vol. 615. Institute of Materials, 1997.

[5] EO Hall. "The deformation and ageing of mild steel: III discussion of results". In: *Proceedings of the Physical Society. Section B* 64.9 (1951), p. 747.

[6] NJ Petch. "The Cleavage Strengh of Polycrystals". In: *J. of the Iron and Steel Inst.* 174 (1953), pp. 25–28.

[7] David Llewellyn and Roger Hudd. *Steels: metallurgy and applications.* Butterworth-Heinemann, 1998.

[8] E Orowan. "Internal stress in metals and alloys". In: *The Institute of Metals, London* 451 (1948).

[9] T Gladman. "Precipitation hardening in metals". In: *Materials science and technology* 15.1 (1999), pp. 30–36.

[10] Günter Gottstein. *Physikalische grundlagen der materialkunde.* Springer-Verlag, 2007.

[11] AJ DeArdo. "Niobium in modern steels". In: *International Materials Reviews* 48.6 (2003), pp. 371–402.

[12] Imao Tamura, Hiroshi Sekine, and Tomo Tanaka. *Thermomechanical processing of high-strength low-alloy steels.* Butterworth-Heinemann, 2013.

[13] DH Jack and KH Jack. "Invited review: carbides and nitrides in steel". In: *Materials Science and Engineering* 11.1 (1973), pp. 1–27.

[14] Kiyoshi Nishioka and Kazutoshi Ichikawa. “Progress in thermomechanical control of steel plates and their commercialization”. In: *Science and Technology of Advanced Materials* 13.2 (2012), p. 023001.

[15] Lutz Meyer. In: *Thyssen Technische Berichte* 1 (1984), pp. 34–44.

[16] AM Elwazri et al. “Characterisation of precipitation of niobium carbide using carbon extraction replicas and thin foils by FESEM”. In: *Materials science and technology* 22.5 (2006), pp. 537–541.

[17] Daniel Acevedo-Reyes et al. “Characterization of precipitates size distribution: validation of low-voltage STEM”. In: *Journal of microscopy* 232.1 (2008), pp. 112–122.

[18] J Lu, DG Ivey, and H Henein. “A Review of Methods to Quantify Nanoscale Precipitates in Microalloyed Steels, Part 1”. In: *Iron & Steel Technology* 10.1 (2013), pp. 232–244.

[19] Andrew J Breen et al. “Resolving the morphology of niobium carbonitride nano-precipitates in steel using atom probe tomography”. In: *Microscopy and Microanalysis* 20.4 (2014), pp. 1100–1110.

[20] Mohamed Sennour and Claude Esnouf. “Contribution of advanced microscopy techniques to nano-precipitates characterization: case of AlN precipitation in low-carbon steel”. In: *Acta Materialia* 51.4 (2003), pp. 943–957.

[21] Eglantine Courtois, Thierry Epicier, and C Scott. “EELS study of niobium carbo-nitride nano-precipitates in ferrite”. In: *Micron* 37.5 (2006), pp. 492–502.

[22] David B Williams and C Barry Carter. *Transmission electron microscopy.* Springer, 1996.

[23] MF Ashby and R Ebeling. “On the determination of the number, size, spacing, and volume fraction of spherical second-phase particles from extraction replicas”. In: *AIME MET SOC TRANS* 236.10 (1966), pp. 1396–1404.

[24] ÖN Doğan, GM Michal, and HW Kwon. “True size distribution of simple polyhedral particles obtained from TEM images of extraction replicas”. In: *Materials characterization* 34.3 (1995), pp. 173–179.

[25] E Smith and J Nutting. “Direct carbon replicas from metal surfaces”. In: *British Journal of Applied Physics* 7.6 (1956), p. 214.

[26] DE Bradley. “Replica techniques in applied electron microscopy”. In: *Journal of Microscopy* 79.2 (1959), pp. 101–118.

[27] BC Buzek and CA Hoffman. "Use of surface replication, extraction replication, and thin-film electron microscopy in the study of dispersion-strengthened materials". In: (1968).

[28] George F Vander Voort. *Metallography, principles and practice.* ASM International, 1984.

[29] AR Marder. "Replication microscopy techniques for NDE". In: *ASM Handbook.* 17 (1989), pp. 52–56.

[30] T Mukherjee, WE Stumpf, and CM Sellars. "Quantitative assessment of extraction replicas for particle analysis". In: *Journal of Materials Science* 3.2 (1968), pp. 127–135.

[31] CP Scott et al. "Quantitative analysis of complex carbo-nitride precipitates in steels". In: *Scripta materialia* 47.12 (2002), pp. 845–849.

[32] P Gong, EJ Palmiere, and WM Rainforth. "Dissolution and precipitation behaviour in steels microalloyed with niobium during thermomechanical processing". In: *Acta Materialia* 97 (2015), pp. 392–403.

[33] CY Chen et al. "Precipitation hardening of high-strength low-alloy steels by nanometer-sized carbides". In: *Materials Science and Engineering: A* 499.1 (2009), pp. 162–166.

[34] ZJ Xie et al. "Nano-sized precipitation and properties of a low carbon niobium micro-alloyed bainitic steel". In: *Materials Science and Engineering: A* 641 (2015), pp. 37–44.

[35] Zhongyi Li et al. "Precipitates in Nb and Nb–V microalloyed X80 pipeline steel". In: *Microscopy and Microanalysis* 19.S5 (2013), pp. 62–65.

[36] GK Tirumalasetty et al. "Characterization of NbC and (Nb, Ti) N nanoprecipitates in TRIP assisted multiphase steels". In: *Acta Materialia* 59.19 (2011), pp. 7406–7415.

[37] Youryeol Lee and Bruno C De Cooman. "TiN/NbC Compound Particle Formation during Thin Slab Direct Rolling of HSLA Steel". In: *steel research international* 85.7 (2014), pp. 1158–1172.

[38] Erik J Pavlina, CJ Van Tyne, and JG Speer. "Effects of combined silicon and molybdenum alloying on the size and evolution of microalloy precipitates in HSLA steels containing niobium and titanium". In: *Materials Characterization* 102 (2015), pp. 35–46.

[39] AJ Craven et al. "Complex heterogeneous precipitation in titanium–niobium microalloyed Al-killed HSLA steels—I.(Ti, Nb)(C, N) particles". In: *Acta Materialia* 48.15 (2000), pp. 3857–3868.

[40] AJ Craven et al. "Complex heterogeneous precipitation in titanium–niobium microalloyed Al-killed HSLA steels—II. Non-titanium based particles". In: *Acta materialia* 48.15 (2000), pp. 3869–3878.

[41] Christian Klinkenberg, Klaus Hulka, and Wolfgang Bleck. "Niobium carbide precipitation in microalloyed steel". In: *steel research international* 75.11 (2004), pp. 744–752.

[42] Miloslav Béreš et al. "TEM investigations of fine niobium precipitates in HSLA steel". In: *steel research international* 75.11 (2004), pp. 753–758.

[43] Matthias Nöhrer, Sabine Zamberger, and Harald Leitner. "Strain-Induced Precipitation Behavior of a Nb–Ti–V Steel in the Austenite Phase Field". In: *steel research international* 84.9 (2013), pp. 827–836.

[44] YF Shen, Chong M Wang, and Xin Sun. "A micro-alloyed ferritic steel strengthened by nanoscale precipitates". In: *Materials Science and Engineering: A* 528.28 (2011), pp. 8150–8156.

[45] John E Bonevich and Wolfgang K Haller. *Measuring the size of nanoparticles using transmission electron microscopy (TEM).* Tech. rep. 2010.

[46] Stephen B Rice et al. "Particle size distributions by transmission electron microscopy: an interlaboratory comparison case study". In: *Metrologia* 50.6 (2013), p. 663.

[47] Hiroaki Masuda and Kuniaki Gotoh. "Study on the sample size required for the estimation of mean particle diameter". In: (1999).

[48] Josef Draxler and Matthäus Siebenhofer. "Partikelgrößen und Partikelgrößenverteilungen". In: *Verfahrenstechnik in Beispielen.* Springer, 2014, pp. 239–258.

[49] Alicia Weibel et al. "The big problem of small particles: a comparison of methods for determination of particle size in nanocrystalline anatase powders". In: *Chemistry of Materials* 17.9 (2005), pp. 2378–2385.

[50] Thos R Cunningham and RJ Price. "Determination of Nonmetallic Inclusions in Plain Carbon and Manganese Steels Iodine and Nitric Acid Extraction Methods". In: *Industrial & Engineering Chemistry Analytical Edition* 5.1 (1933), pp. 27–29.

[51] JG Thompson and JS Acken. "Determination of Alumina and Silica in Steel by the Hydrochloric Acid Residue Method". In: *Bureau of Standard Journal of Research* 9 (1932), pp. 615–623.

[52] J. E. Garside, T. E. Rooney, and J. J. J. Belli. “The alcoholic-iodine method for the extraction of inclusions from steel”. In: *Journal of The Iron and Steel Institue* 185.1 (1957), pp. 95–103.

[53] Ulrich Bohnstedt. “Brom-Methanol als Hilfsmittel bei der Oxidisolierung aus Stählen und verwandten Legierungen”. In: *Fresenius' Journal of Analytical Chemistry* 199.2 (1964), pp. 109–117.

[54] RG Smerko and DA Flinchbaugh. “Recent Progress in the Chemical Extraction of Nonmetallic Inclusions in Steel—Techniques and Applications”. In: *JOM* 20.7 (1968), pp. 43–51.

[55] Keith E Burke. “Chemical extraction of refractory inclusions from iron-and nickel-base alloys”. In: *Metallography* 8.6 (1975), pp. 473–488.

[56] Marcolino Fernandes, Noé Cheung, and Amauri Garcia. “Investigation of nonmetallic inclusions in continuously cast carbon steel by dissolution of the ferritic matrix”. In: *Materials characterization* 48.4 (2002), pp. 255–261.

[57] Ryo Inoue et al. “Extraction of nonmetallic inclusion particles containing MgO from steel”. In: *ISIJ international* 51.12 (2011), pp. 2050–2055.

[58] Junfang Lu, Douglas Ivey, and Hani Henein. “Quantification of nanosized precipitates in microalloyed steels by matrix dissolution”. In: *Proceedings of IPC2006, 6th International Pipeline Conference.* 2006.

[59] H Brucková and Š Nižnık. “Chemical isolation of precipitates in IF steels”. In: *Chemical Papers* 47.6 (1993), pp. 346–350.

[60] Hamid Doostmohammadi, Andrey Karasev, and Pär G Jönsson. “A Comparison of a Two-Dimensional and a Three-Dimensional Method for Inclusion Determinations in Tool Steel”. In: *Steel research international* 81.5 (2010), pp. 398–406.

[61] Ryo Inoue et al. “Applicability of Nonaqueous Electrolytes for Electrolytic Extraction of Inclusion Particles Containing Zr, Ti, and Ce”. In: *ISIJ international* 53.11 (2013), pp. 1906–1912.

[62] Elizabeth Garfias-García, Miriam Aguilar-Sánchez, and Mario A Romero-Romo. “Electrochemical extraction technique and SEM study of precipitated carbides at grain boundaries in austenitic stainless steel”. In: *ECS Transactions* 47.1 (2013), pp. 149–156.

[63] AL Rivas et al. “Electrochemical extraction of microalloy carbides in Nb-steel”. In: *Revista de metalurgia* 44.5 (2008), pp. 447–456.

[64] S Read, RK Gibbs, and BA Parker. “Extraction and characterization of precipitates formed in a niobium HSLA steel”. In: *Materials forum.* Vol. 14. 4. Institute of Metals and Materials Australasia. 1990, pp. 304–307.

[65] Lee M Rothleutner, Robert Cryderman, and Chester J Van Tyne. “Influence of Temperature and Holding Time on the Interaction of V, Al, and N in Microalloyed Forging Steels”. In: *Metallurgical and Materials Transactions A* 45.10 (2014), pp. 4594–4609.

[66] Diana Janis et al. “Application of different extraction methods for investigation of nonmetallic inclusions and clusters in steels and alloys”. In: *Advances in Materials Science and Engineering* 2014 (2014).

[67] Junfang Lu et al. “Matrix dissolution techniques applied to extract and quantify precipitates from a microalloyed steel”. In: *Metallurgical and Materials Transactions A* 42.7 (2011), pp. 1767–1784.

[68] J Barry Wiskel et al. “Characterization of precipitates in a microalloyed steel using quantitative X-ray diffraction”. In: *Metals* 6.4 (2016), p. 90.

[69] Kazumi Mizukami et al. “Method of analyzing particle size distribution of particles in metal material”. Patent US 8384897. Apr. 2008.

[70] Ishida Tomoharu, Kajima Yoshihisa, and Yoshi Naoshi. “Analysis method of particulate in steel”. Patent JP 2009008584 A. Jan. 2009.

[71] ASTM E194-10(2015). *Standard Test Method for Acid-Insoluble Content of Copper and Iron Powders.* Tech. rep. West Conshohocken, PA: ASTM International, 2015.

[72] Hugh O Pierson. *Handbook of Refractory Carbides & Nitrides: Properties, Characteristics, Processing and Apps.* William Andrew, 1996.

[73] Louis Toth. *Transition metal carbides and nitrides.* Elsevier, 2014.

[74] T Ya Kosolapova. *Carbides: properties, production, and applications.* Springer Science & Business Media, 2012.

[75] W Lengauer. “Transition metal carbides, nitrides, and carbonitrides”. In: *Handbook of ceramic hard materials* (2000), pp. 202–252.

[76] Cristina Giordano et al. “Metal nitride and metal carbide nanoparticles by a soft urea pathway”. In: *Chemistry of Materials* 21.21 (2009), pp. 5136–5144.

[77] Jinming Duan and John Gregory. “Coagulation by hydrolysing metal salts”. In: *Advances in colloid and interface science* 100 (2003), pp. 475–502.

[78] Ralph K Iler. *The chemistry of silica: solubility, polimerization, colloid and surface properties, and biochemistry.* Wiley Interscience, 1979.

[79] Leonard Dubin. "Silica inhibition: prevention of silica deposition by boric acid/orthorborate ion". Patent US 4,584,104. Apr. 1986.

[80] Enrique Antonio Reyes. "Acidic treatment fluids containing non-polymeric silica scale control additives and methods related thereto". Patent US 8,727,002. May 2014.

[81] Matthias Stieß. *Mechanische Verfahrenstechnik-Partikeltechnologie 1.* Springer-Verlag, 2008.

[82] Gerhard Lagaly, Oliver Schulz, and Ralf Zimehl. *Dispersionen und Emulsionen: eine Einführung in die Kolloidik feinverteilter Stoffe einschließlich der Tonminerale.* Springer-Verlag, 2013.

[83] Frank Babick. *Suspensions of colloidal particles and aggregates.* Vol. 20. Springer, 2016.

[84] Lothar Papula. *Mathematik für Ingenieure und Naturwissenschaftler. Vektoranalysis, Wahrscheinlichkeitsrechnung, Mathematische Statistik, Fehler- und Ausgleichsrechnung.* Vol. 7. Springer, 2016.

[85] Henk G Merkus. *Particle size measurements: fundamentals, practice, quality.* Vol. 17. Springer Science & Business Media, 2009.

[86] Scott C Brown et al. "Toward advancing nano-object count metrology: a best practice framework". In: *Environmental health perspectives* 121.11-12 (2013), p. 1282.

[87] Jörg Stetefeld, Sean A McKenna, and Trushar R Patel. "Dynamic light scattering: a practical guide and applications in biomedical sciences". In: *Biophysical reviews* 8.4 (2016), pp. 409–427.

[88] AJF Siegert. *On the fluctuations in signals returned by many independently moving scatterers.* Radiation Laboratory, Massachusetts Institute of Technology, 1943.

[89] Puthusserickal A Hassan, Suman Rana, and Gunjan Verma. "Making sense of brownian motion: colloid characterization by dynamic light scattering". In: *Langmuir* 31.1 (2014), pp. 3–12.

[90] Renliang Xu. *Particle characterization: light scattering methods.* Vol. 13. Springer Science & Business Media, 2001.

[91] Stephen W Provencher. "Inverse problems in polymer characterization: direct analysis of polydispersity with photon correlation spectroscopy". In: *Macromolecular Chemistry and Physics* 180.1 (1979), pp. 201–209.

[92] Stephen W Provencher. “A constrained regularization method for inverting data represented by linear algebraic or integral equations”. In: *Computer Physics Communications* 27.3 (1982), pp. 213–227.

[93] Walter Mächtle and Lars Börger. *Analytical ultracentrifugation of polymers and nanoparticles*. Springer Science & Business Media, 2006.

[94] Johannes Walter. PhD thesis. Friedrich-Alexander Univeristät Erlangen Nürnberg, 2017.

[95] Walter F Stafford. “Boundary analysis in sedimentation transport experiments: a procedure for obtaining sedimentation coefficient distributions using the time derivative of the concentration profile”. In: *Analytical biochemistry* 203.2 (1992), pp. 295–301.

[96] KE Van Holde and Wolfgang O Weischet. “Boundary analysis of sedimentation-velocity experiments with monodisperse and paucidisperse solutes”. In: *Biopolymers* 17.6 (1978), pp. 1387–1403.

[97] Leslie A Holladay. “Simultaneous rapid estimation of sedimentation coefficient and molecular weight”. In: *Biophysical chemistry* 11.2 (1980), pp. 303–308.

[98] Peter Schuck. “Size-distribution analysis of macromolecules by sedimentation velocity ultracentrifugation and lamm equation modeling”. In: *Biophysical journal* 78.3 (2000), pp. 1606–1619.

[99] Borries Demeler and Hashim Saber. “Determination of molecular parameters by fitting sedimentation data to finite-element solutions of the Lamm equation”. In: *Biophysical journal* 74.1 (1998), pp. 444–454.

[100] Peter Schuck and Peter Rossmanith. “Determination of the sedimentation coefficient distribution by least-squares boundary modeling”. In: *Biopolymers* 54.5 (2000), pp. 328–341.

[101] Vikas Mittal, Antje Völkel, and Helmut Cölfen. “Analytical ultracentrifugation of model nanoparticles: Comparison of different analysis methods”. In: *Macromolecular bioscience* 10.7 (2010), pp. 754–762.

[102] Jennifer A Jamison et al. “Size-dependent sedimentation properties of nanocrystals”. In: *Acs Nano* 2.2 (2008), pp. 311–319.

[103] Peter Schuck et al. *Basic principles of analytical ultracentrifugation*. CRC Press, 2016.

[104] J Calvin Giddings. “A new separation concept based on a coupling of concentration and flow nonuniformities”. In: *Separation Science* 1.1 (1966), pp. 123–125.

[105] Aljosha-Rakim Jochem. PhD thesis. Saarland University, 2017.

[106] John Calvin Giddings, Martin E Schimpf, and Karin Caldwell. *Field-flow fractionation handbook*. Wiley-interscience, 2000.

[107] J Calvin Giddings, P Stephen Williams, and Maria Anna Benincasa. "Rapid breakthrough measurement of void volume for field-flow fractionation channels". In: *Journal of Chromatography A* 627.1-2 (1992), pp. 23–35.

[108] Nina Bendixen et al. "Membrane–particle interactions in an asymmetric flow field flow fractionation channel studied with titanium dioxide nanoparticles". In: *Journal of Chromatography A* 1334 (2014), pp. 92–100.

[109] Thilak K Mudalige et al. "Simple functionalization strategies for enhancing nanoparticle separation and recovery with asymmetric flow field flow fractionation". In: *Analytical chemistry* 87.3 (2015), pp. 1764–1772.

[110] Aljosha-Rakim Jochem et al. "Colloidal mechanisms of gold nanoparticle loss in asymmetric flow field-flow fractionation". In: *Analytical chemistry* 88.20 (2016), pp. 10065–10073.

[111] Julien Gigault and Vincent A Hackley. "Observation of size-independent effects in nanoparticle retention behavior during asymmetric-flow field-flow fractionation". In: *Analytical and bioanalytical chemistry* 405.19 (2013), pp. 6251–6258.

[112] Seungho Lee et al. "Determination of mean diameter and particle size distribution of acrylate latex using flow field-flow fractionation, photon correlation spectroscopy, and electron microscopy". In: *Analytical chemistry* 68.9 (1996), pp. 1545–1549.

[113] Carina A Sötebier et al. "Sample loss in asymmetric flow field-flow fractionation coupled to inductively coupled plasma-mass spectrometry of silver nanoparticles". In: *Journal of Analytical Atomic Spectrometry* 30.10 (2015), pp. 2214–2222.

[114] Haiou Qu et al. "Importance of material matching in the calibration of asymmetric flow field-flow fractionation: material specificity and nanoparticle surface coating effects on retention time". In: *Journal of Nanoparticle Research* 18.10 (2016), p. 292.

[115] C Degueldre and P-Y Favarger. "Colloid analysis by single particle inductively coupled plasma-mass spectroscopy: a feasibility study". In: *Colloids and Surfaces A: Physicochemical and Engineering Aspects* 217.1-3 (2003), pp. 137–142.

[116] Kazuhiro Sakai. *Determination of trace elements in steel using the Agilent 7900 ICP-MS*. Application note. Agilent Technologies, 2015.

[117] Gen Okano et al. “Determination of trace amounts of bismuth in steel by ICP-MS through a cascade-preconcentration and separation method”. In: *ISIJ International* 55.1 (2015), pp. 332–334.

[118] Susanne Finkeldei and G Staats. “ICP-MS–A powerful analytical technique for the analysis of traces of Sb, Bi, Pb, Sn and P in steel”. In: *Fresenius' journal of analytical chemistry* 359.4-5 (1997), pp. 357–360.

[119] Manuel D Montaño et al. “Single particle ICP-MS: advances toward routine analysis of nanomaterials”. In: *Analytical and bioanalytical chemistry* 408.19 (2016), pp. 5053–5074.

[120] Robert Thomas. “Spectroscopy tutorial-A beginner's guide to ICP-MS-Part II: The sample-introduction system”. In: *Spectroscopy* 16.5 (2001), pp. 56–+.

[121] Akbar Montaser. *Inductively coupled plasma mass spectrometry*. John Wiley & Sons, 1998.

[122] Robert Thomas. “A beginner's guide to ICP-MS-Part III: The plasma source”. In: *Spectroscopy* 16.6 (2001), pp. 26–+.

[123] Robert Thomas. “A beginner's guide to ICP-MS-Part IV: The interface region”. In: *Spectroscopy* 16.7 (2001), pp. 26–+.

[124] Robert Thomas. “A beginner's guide to ICP-MS-Part V: The ion focusing system”. In: *Spectroscopy* 16.9 (2001), pp. 38–+.

[125] Robert Thomas. “A beginner's guide to ICP-MS-Part VIII: Mass analyzers: time-of-flight technology”. In: *Spectroscopy* 17.1 (2002), pp. 36–+.

[126] Robert Thomas. “Spectroscopy Tutorial-A Beginner's Guide to ICP-MS, Part X–Detectors”. In: *Spectroscopy-Eugene* 17.4 (2002), pp. 34–39.

[127] Sungyun Lee et al. “Nanoparticle size detection limits by single particle ICP-MS for 40 elements”. In: *Environmental science & technology* 48.17 (2014), pp. 10291–10300.

[128] Heather E Pace et al. “Determining transport efficiency for the purpose of counting and sizing nanoparticles via single particle inductively coupled plasma mass spectrometry”. In: *Analytical chemistry* 83.24 (2011), pp. 9361–9369.

[129] Manfred Dieter Lechner et al. "Sedimentation measurements with the analytical ultracentrifuge with absorption optics: influence of Mie scattering and absorption of the particles". In: *Colloid and Polymer Science* 289.10 (2011), pp. 1145–1155.

[130] Gustav Mie. "Beiträge zur Optik trüber Medien, speziell kolloidaler Metallösungen". In: *Annalen der physik* 330.3 (1908), pp. 377–445.

[131] Craig F Bohren and Donald R Huffman. *Absorption and scattering of light by small particles*. John Wiley & Sons, 2008.

[132] Christian Mätzler. *MATLAB Functions for Mie Scattering and Absorption*. Insitute of Applied Physics. Universtiy of Bern, 2002.

[133] Will Anderson et al. "A comparative study of submicron particle sizing platforms: accuracy, precision and resolution analysis of polydisperse particle size distributions". In: *Journal of colloid and interface science* 405 (2013), pp. 322–330.

[134] Nia C Bell et al. "Emerging techniques for submicrometer particle sizing applied to Stober silica". In: *Langmuir* 28.29 (2012), pp. 10860–10872.

[135] Claudia Cascio et al. "Critical experimental evaluation of key methods to detect, size and quantify nanoparticulate silver". In: *Analytical chemistry* 86.24 (2014), pp. 12143–12151.

[136] Kurtis D Hartlen, Aristidis PT Athanasopoulos, and Vladimir Kitaev. "Facile preparation of highly monodisperse small silica spheres (15 to¿ 200 nm) suitable for colloidal templating and formation of ordered arrays". In: *Langmuir* 24.5 (2008), pp. 1714–1720.

[137] A Ayral, J Phalippou, and T Woignier. "Skeletal density of silica aerogels determined by helium pycnometry". In: *Journal of materials science* 27.5 (1992), pp. 1166–1170.

[138] Shigeru Kimoto et al. "Effective Density of Silica Nanoparticle Size Standards". In: *2014 International Aerosol* (2014).

[139] Wolfgang Schärtl. *Light scattering from polymer solutions and nanoparticle dispersions*. Springer Science & Business Media, 2007.

[140] Dirk Mahl et al. "Possibilities and limitations of different analytical methods for the size determination of a bimodal dispersion of metallic nanoparticles". In: *Colloids and Surfaces A: Physicochemical and Engineering Aspects* 377.1-3 (2011), pp. 386–392.

[141] Helmut Cölfen et al. "The open AUC project". In: *European Biophysics Journal* 39.3 (2010), pp. 347–359.

[142] Johannes Walter et al. “Multidimensional analysis of nanoparticles with highly disperse properties using multiwavelength analytical ultracentrifugation”. In: *ACS nano* 8.9 (2014), pp. 8871–8886.

[143] Johannes Walter and Wolfgang Peukert. “Dynamic range multiwavelength particle characterization using analytical ultracentrifugation”. In: *Nanoscale* 8.14 (2016), pp. 7484–7495.

[144] Johannes Schindelin et al. “Fiji: an open-source platform for biological-image analysis”. In: *Nature methods* 9.7 (2012), pp. 676–682.

[145] Thomas Roth. “Charakterisierung des Ausscheidungsverhaltens mikrolegierter Stähle mittels Rasterelektronenmikroskopie und Simulation”. MA thesis. Universität des Saarlandes, 2016.

[146] Egon Matijević. *Fine particles in medicine and pharmacy.* Springer, 2012.

[147] Sadao Adachi. *The Handbook on Optical Constants of Metals: In Tables and Figures.* World Scientific, 2012.

[148] Randy P Carney et al. “Determination of nanoparticle size distribution together with density or molecular weight by 2D analytical ultracentrifugation”. In: *Nature communications* 2 (2011), p. 335.

[149] Ruud JB Peters et al. “Development and validation of single particle ICP-MS for sizing and quantitative determination of nano-silver in chicken meat”. In: *Analytical and bioanalytical chemistry* 406.16 (2014), pp. 3875–3885.

[150] Markus Witzler et al. “Validation of Gold and Silver Nanoparticle Analysis in Fruit Juices by Single-Particle ICP-MS without Sample Pretreatment”. In: *Journal of agricultural and food chemistry* 64.20 (2016), pp. 4165–4170.

[151] Steffi Naasz et al. “Multi-element analysis of single nanoparticles by ICP-MS using quadrupole and time-of-flight technologies”. In: *Journal of Analytical Atomic Spectrometry* 33.5 (2018), pp. 835–845.

Appendix A

Multimodal particle analysis

A.1 In situ dynamic light scattering

In addition to retention time analysis of monomodal reference particle dispersions and multimodal particle mixtures in section 3.4, particle suspensions were characterized by in situ DLS as verification measurement. The particle diameters measured using in situ DLS were in good agreement with the diameters determined using retention time calibration. Figure A.1, A.2, and A.3 show the relative scattering intensity (black) and the corresponding hydrodynamic diameter (blue) in dependency of the retention time for different monomodal reference particle dispersions and the multimodal mixtures.

The hydrodynamic diameters at the positions of the highest scattering intensities are given in Table A.1, A.2, and A.3.

The gold particles with a nominal diameter of 5 nm were difficult to analyze with in situ DLS. Only few proper measurements of the monomodal reference particle dispersion were obtained and diameters scattered around 9 nm. The small particle population in the particle mixture could not be measured at all. The large gold particles with nominal sizes of 50 nm showed partial agglomeration with increasing hydrodynamic diameter towards large retention times. This effect was more pronounced for particles in the model mixture than for the monomodal reference particle dispersions, which can explain concentration differences between the monomodal model particle dispersions and the model particle mixture.

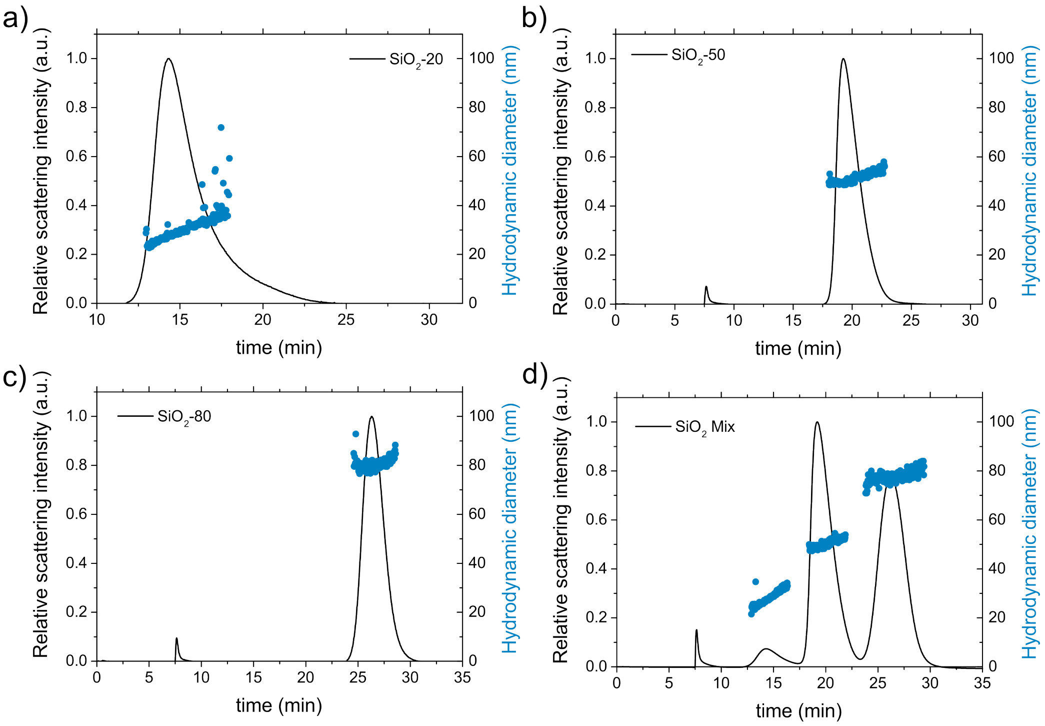

Figure A.1: In situ DLS of silica reference particles: a) 20 nm silica particles, b) 50 nm silica particles, c) 80 nm silica particles, and d) silica particle mixture.

	SiO$_2$-20	SiO$_2$-50	SiO$_2$-80
Monomodal reference particles (nm)	29	50	80
Multimodal particle mixture (nm)	27	49	79

Table A.1: Hydrodynamic diameter at maximal scattering intensity determined for monomodal silica reference particle dispersions and according multimodal particle mixture.

	PSL-20	PSL-50	PSL-80
Monomodal reference particles (nm)	28	58	103
Multimodal particle mixture (nm)	28	59	99

Table A.2: Hydrodynamic diameter at maximal scattering intensity determined for monomodal PSL reference particle dispersions and according multimodal particle mixture.

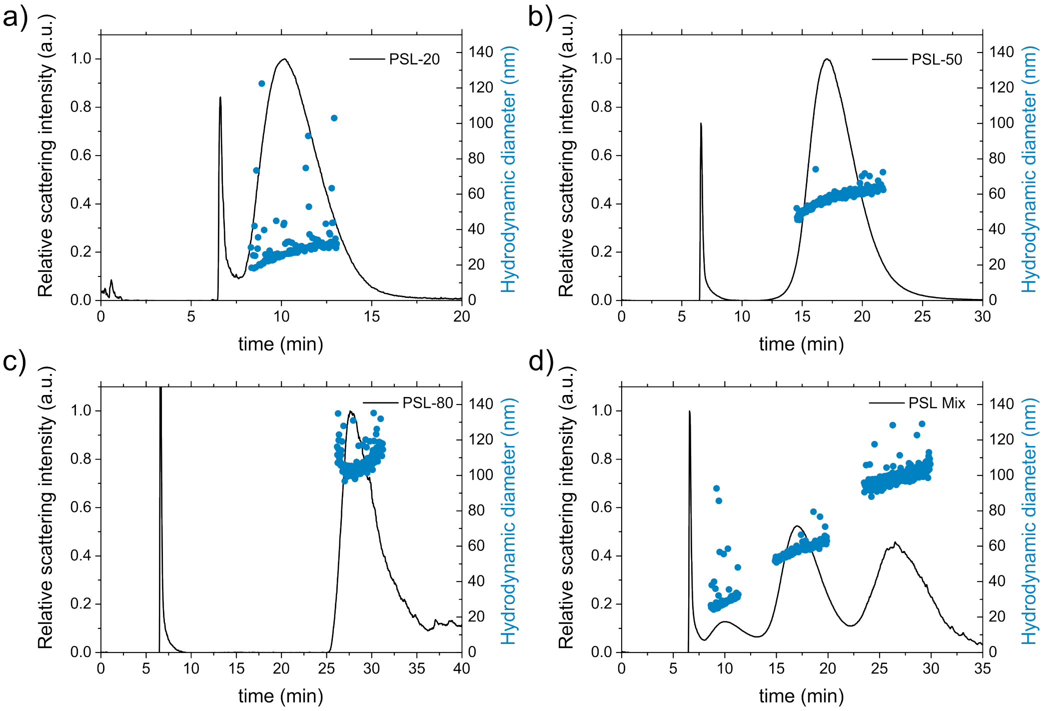

Figure A.2: In situ DLS of silica reference particles: a) 20 nm PSL particles, b) 50 nm PSL particles, c) 80 nm PSL particles, and d) PSL particle mixture.

	Au-5	Au-20	Au-50
Monomodal reference particles (nm)	9	27.5	71
Multimodal particle mixture (nm)	-	35	83

Table A.3: Hydrodynamic diameter at maximal scattering intensity determined for monomodal Au reference particle dispersions and according multimodal particle mixture.

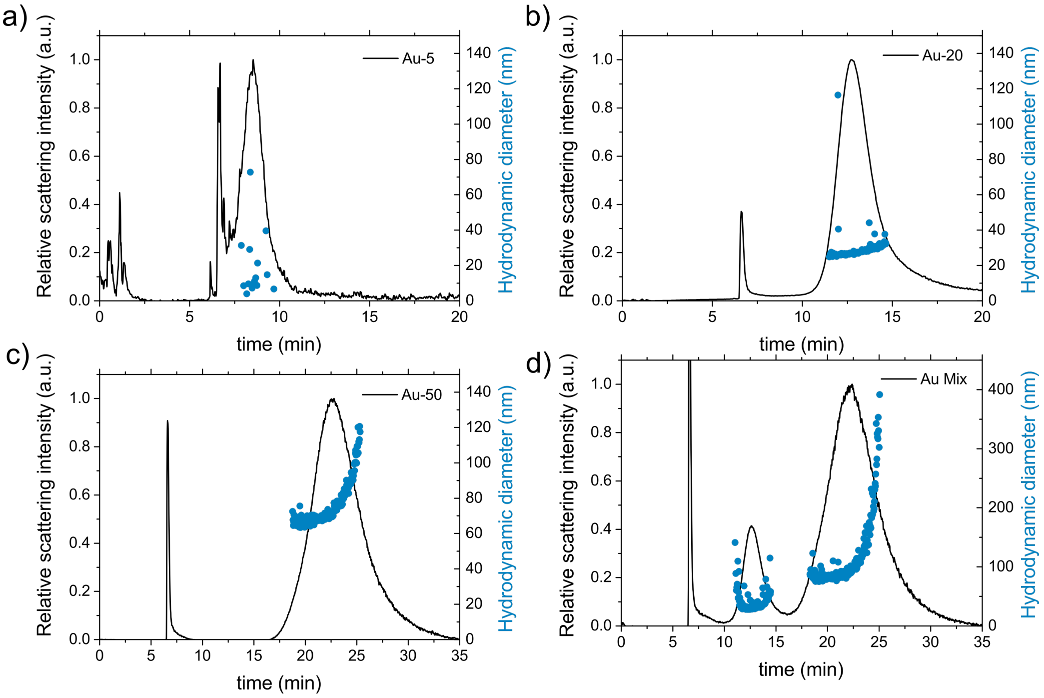

Figure A.3: In situ DLS of Au reference particles: a) 20 nm Au particles, b) 50 nm Au particles, c) 80 nm Au particles, and d) Au particle mixture.

Appendix B

Colloidal analysis

B.1 Chemical composition of the steels

The detailed compositions of the steels from section 4.1 are given in Table B.1.

Element (wt%)	**Steel A**	**Steel B**	**Steel C**
C	0.06	0.05	0.06
Si	0.43	0.28	0.17
Mn	1.6	1.59	1.65
N	0.003	0.004	0.004
Al	0.03	0.03	0.03
Cu	0.27	0.27	0.23
Mo	0.03	0.03	0.01
Ni	0.45	0.45	0.03
Cr	0.23	0.05	0.03
Nb	**0.001**	**0.02**	**0.04**
Ti	**0.008**	**0.003**	**0.02**
CEV*	0.368	0.378	0.424

Table B.1: Complete composition of the three investigated steels.

B.2 Transmission electron microscopy

The extracted particles from steel A, steel B, and steel C were characterized by TEM. Figure B.1 a-c shows an overview of the extracted particles for the three steels. The particles were well distributed, mainly without agglomeration, and small shadows were apparent caused by remaining dispersant and residues of Fe(OH)$_x$ and Si$_x$Al$_y$O$_z$, that were not completely removed during centrifugation. Steel A mainly contained particles with rectangular shapes.

The shapes of the particles from steel B and steel C were not well defined and adopted spherical and angular shapes. The corresponding EDX spectra of the particles shown in Figure B.1 a-c are shown in Figure B.1 d-f.

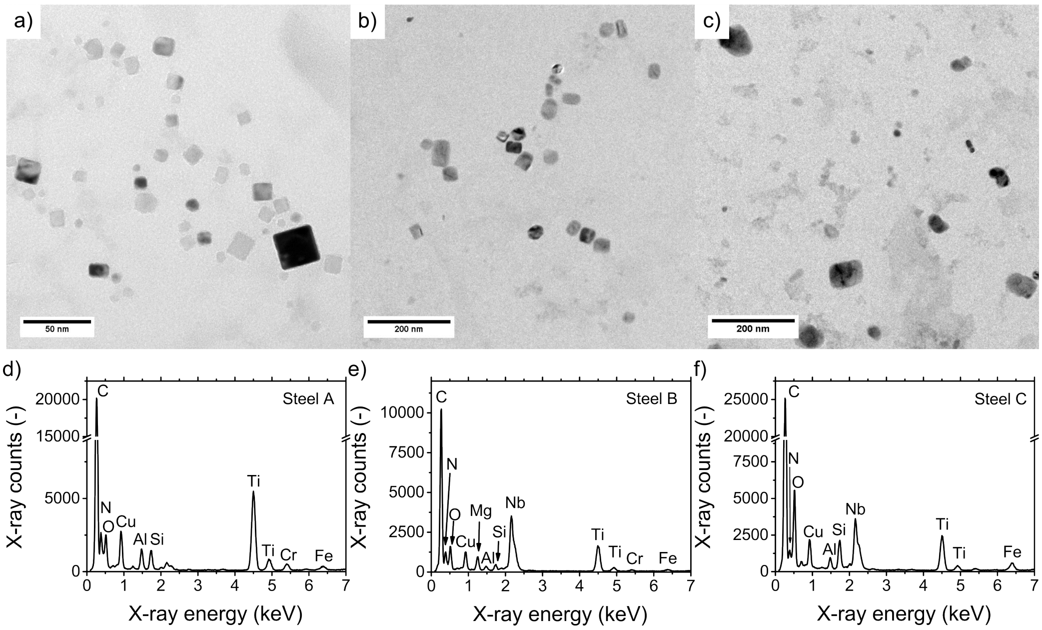

Figure B.1: TEM analysis of the steel A, B, C: a) TEM overview of steel A. b) TEM overview of steel B. c) TEM overview of steel C. d) EDX spectrum of sample section from steel A in a). e) EDX spectrum of sample section from steel B in b). EDX spectrum of sample section from steel C in c).

The EDX spectra show that the particles considered are Nb, Ti, and NbTi carbonitride particles. As expected, steel A mainly has TiCN. There are also traces of Al, Si, O, and Fe. Aluminum may also be present in some particles, but is mainly present in the residue together with Si and O. The particles of steel B also contained Ti, which is contrary to expectations (mainly alloyed with Nb, see Table B.1). Titanium precipitates as TiN at very high temperatures. These particles represent crystallisation nuclei for NbCN, which growths on these seed particles at lower temperatures forming “core-shell particles”. The “large” particles therefore often contain Ti. The EDX spectrum of steel C shows both Nb and Ti. Other elements present are Al, Si, and O, which are contained in the surrounding residue. The particle size distributions of the three steels are given in Figure B.2.

Steel A had a monomodal PSD with a maximum at approximately 9.5 nm. The number of analyzed particles was 475.

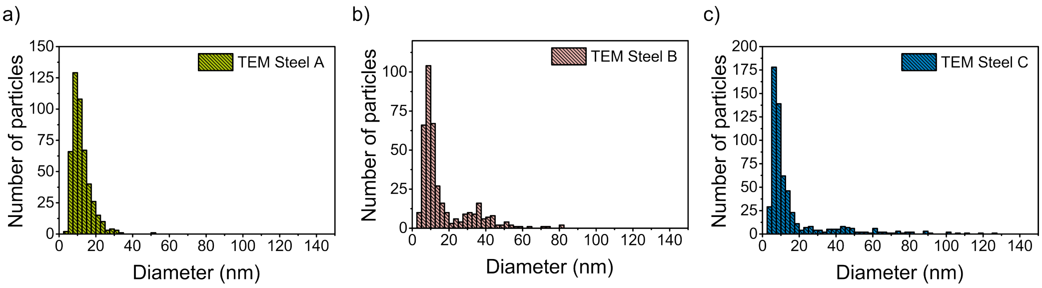

Figure B.2: Number-weighted size distributions of the extracted particles from steel A, B, and C measured with TEM by manual image analysis.

Steel B had a bimodal distribution with smaller particles in the size range of a few nanometer and larger sized particles with diameter around 30 to 50 nm. For the determination of the PSD, 395 individual particles were analyzed.

Steel C showed a broad (bimodal) distribution containing a large number of small particles in the size range of 5 to 10 nm with a peak maximum at approximately 6.5 nm and fewer larger particles with diameters ranging from approximately 20 to 80 nm. In total 590 particles were analyzed.

B.3 Analytical ultracentrifugation

Sedimentation velocity experiments were performed on the individual particle samples from the different steels. Figure B.3 a-c shows the sedimentation profiles of particles extracted from steel A, B, and C at wavelengths of 280, 350, 400, 450, 529, and 620 nm. Note the logarithmic scaling of the s-coefficient axis.

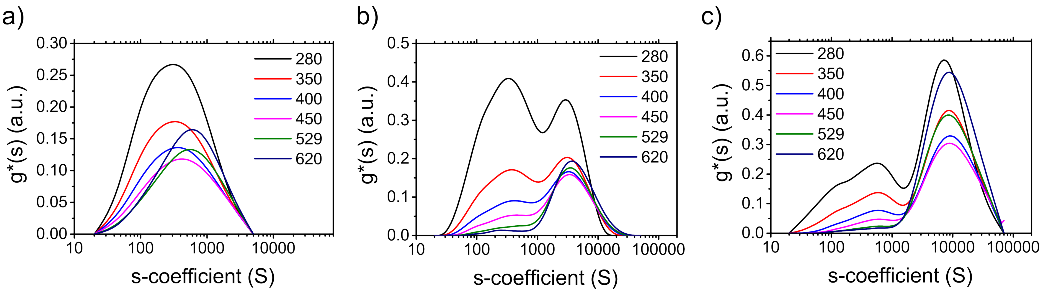

Figure B.3: Analysis of the particles extracted from the investigated steels by means of AUC: Sedimentation coefficient distributions for particles from a) steel A; b) steel B; c) steel C at evaluation wavelengths of 280, 350, 400, 450, 529, and 620 nm.

Particles extracted from steel A had sedimentation coefficients ranging from approx. 20 to 5000 S with a maximum at approx. 300 to 600 S, depending on the wavelength. Steel B had a very broad sedimentation coefficient distribution ranging from approx. 30 to 13 000 S. The distribution is bimodal with maxima at approx. 300 to 500 S and 3000 to 4000 S. The sedimentation coefficients of the particles extracted from steel C ranged from approx. 20 to 70 000 S. Steel C also had a bimodal distribution with maxima at approx. 600 S and 8000 S. It is obvious for all three steel samples that the measured distribution strongly depends on the evaluation wavelength.

The sedimentation distribution curve can be converted into a particle size distribution curve using equation (3.29) and (3.34). However, several assumptions are necessary here. The density of the particles is an important factor, since the density of the particles directly determines the sedimentation velocity (see equation (3.29) and section 4.1.3). First, the ligand introduced during the extraction process influences the density of the particles. Especially for small particles, the ligand accounts for a large proportion of the volume and thus has a decisive influence on the density (see section 3.2.2). I corrected the density for each individual particle size by determining an effective particle density that corrects the actual particle density including the ligand for each individual particle size. Each individual hydrodynamic diameter was calculated by solving equation (B.1) to x_h:

$$2x_\mathrm{h}^2 \cdot \frac{(x_\mathrm{h} - t_\mathrm{ligand})^3\rho_\mathrm{core} + (x_\mathrm{h}^3 - (x_\mathrm{h} - t_\mathrm{ligand})^3)\rho_\mathrm{ligand}}{x_\mathrm{h}} - s_{measured} = 0 \quad \text{(B.1)}$$

Based on the information about the ligand shell from the experiments with Disperbyk-2012 coated gold reference particles (section 4.1.3), the ligand shell was assumed to be 5.74 nm and the ligand density to be 1.25 g/cm^3. Second, there is no possibility to determine the exact density of the particles: due to the mutual solubility of the microalloy carbonitrides, the composition of the particles may vary between NbC ($\rho_{\mathrm{NbC}} = 7.8\,\mathrm{g/cm^3}$), NbN ($\rho_{\mathrm{NbN}} = 7.3\,\mathrm{g/cm^3}$), TiC ($\rho_{\mathrm{TiC}} = 4.9\,\mathrm{g/cm^3}$), and TiN ($\rho_{\mathrm{TiN}} = 5.4\,\mathrm{g/cm^3}$)[72] and have complicated compositions like NbTiCN (see section 4.1.3). To calculate the particle size distribution, the particles of steel A were assumed to be TiN, the particles from steel B and C were assumed to be NbTiCN.

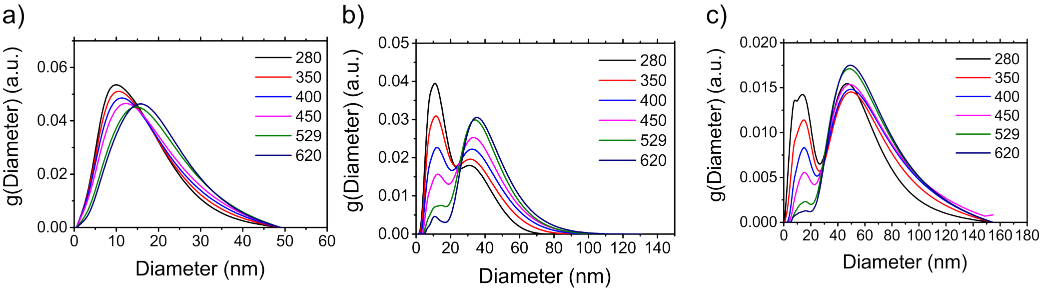

Figure B.4: Extinction-weighted PSD meausured with analytical ultracentrifugation. a) steel A; b) steel B; c) steel C.

The maximum of the PSD of steel A was at approximately 10 to 15 nm, depending on the wavelength of evaluation. The largest particles had diameters of less than 50 nm. The PSD of the particles extracted from steel B had a maximum at approx. 10 nm and at approx. 30 to 40 nm. The largest particles had diameters upto 100 nm. The maxima of the PSD for steel C were at approximately 15 nm and at 50 nm. The minimum between to two peaks was at approximately 25 nm. The large particle fraction had sizes up to 150 nm.

In analogy to the sedimentation coefficient distributions, the transformed size distributions showed a significant dependence on the evaluation wavelength. Due to the wavelength-dependent extinction, the distributions differ significantly. While smaller particles show an increased extinction at short wavelengths, larger particles have an increased extinction at higher wavelengths (see section 4.1.4).

B.4 Field-flow fractionation

Retention time calibration in field-flow fraction using reference particles

Gold nanoparticles coated with Disperbyk-2012 were used to calibrate the separation channel and determine the relation between particle size and retention time. I used gold nanoparticles as calibration standard for the retention time calibration as they were easy to modify and the modified particles showed similar surface charges (Zeta potential, see Table B.2) to the extracted particles. Hence, the interactions between particles and the surfaces in the FFF (membrane, tubings, etc.) are assumed to be similar. Particle density does not influence the separation and thus, the difference in density between gold nanoparticles and microalloy carbonitride particles does not affect the measurement. Even if this might not hold true in all cases [111], the density differences can be neglected in most cases. Figure B.5 shows the retention time dependency of the individual particle sizes.

	Au5	Au15	Au20	Au50	Au80	A	B	C
Zeta potential (mV)	-20	-21	-25	-23	-29	-32	-27	-26

Table B.2: Zeta potential of the gold reference particle coated with Disperbyk-2012 and extracted particles from steel A, B, and C at pH 11.

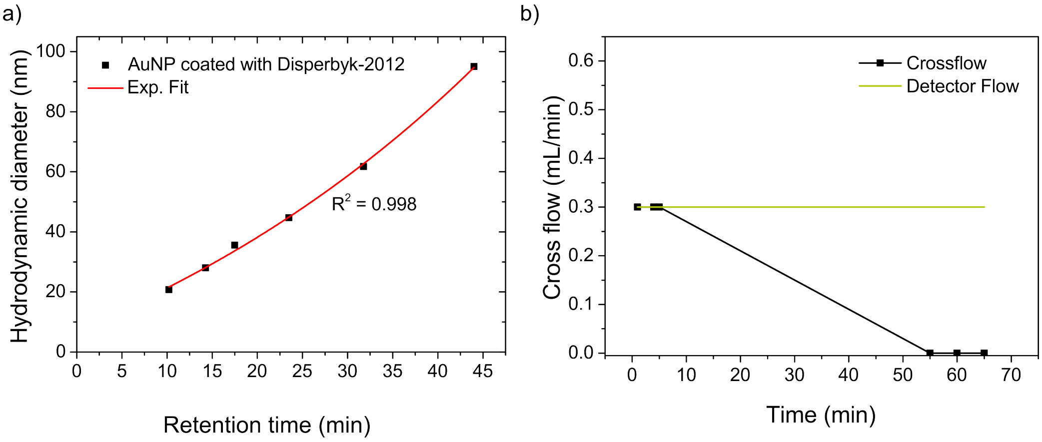

Figure B.5: Particle analysis using field-flow fractionation. a) Calibration of FFF-channel: dependency of the retention time on the hydrodynamic diameter of the Disperbyk-2102 coated gold reference particles. The data is fitted with an exponential fit. b) Applied cross flow and detector flow profile.

The crossflow in the separation channel for particle separation was not constant, but had a linearly decreasing profile (Figure B.5 b). As described in section 3.2.3, a deviation from the constant cross flow may lead to an altered dependency of the retention time to the diffusion coefficient and hence to the particle size. The hydrodynamic diameter of the Disperbyk-2012 coated Au-reference particles showed an exponential relation to the retention time according to equation (B.2):

$$x = C + A \cdot \exp(B \cdot t) \tag{B.2}$$

with the fit parameter $A = 65.39$, $B = 0.01971$, and $C = -58.799$. Due to the non-linear relation between retention time and particle diameter, the measured retention time distribution $g(t)$ had to be converted into the size distribution $g(x)$ according to equation (B.3):

$$g(x) = g(t)\frac{dt}{dx} = g(t)\frac{1}{B \cdot (x - C)} \tag{B.3}$$

Analysis of particles extracted from steel

The extracted particles from the three different steels were analyzed by HF5. The retention time was recorded using the UV-Vis detector at a wavelength of 280 nm. The small particle fractions could not be detected at higher wavelengths due to too low light extinction and by SLS and DLS due to too low scattering signal. Figure B.6 shows the fractograms of the three different steel samples.

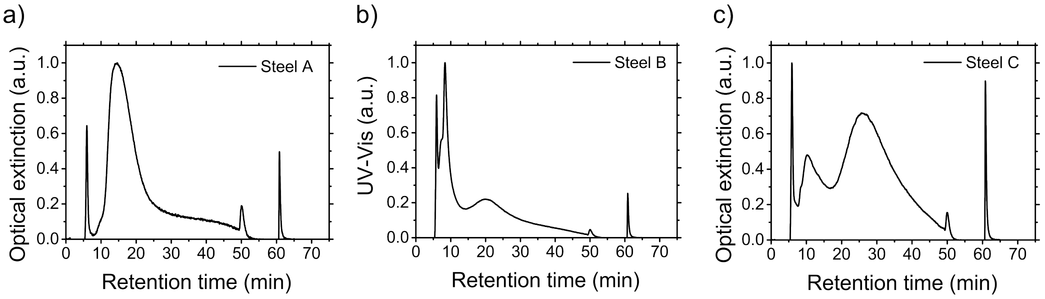

Figure B.6: FFF fractograms of the three different steel samples evalutated at a wavelength of 280 nm: a) steel A; b) steel B; c) steel C.

The fractograms of the particle samples analyzed by FFF showed a good separation of the particles in the separation channel and the individual particle fractions are clearly recognized. All fractograms show the following characteristics: the void peak at 5.92 min is clearly visible, which is used to determine the effective net retention time. Furthermore, the release peak can be seen at approx. 50 min, which indicates that the cross-flow has been switched off. All particles that still remained on the membrane are rinsed out here. Another peak is visible at approx. 62 min. This peak relates to the method. At the end of the method, a switch from "elution" mode to "elution+inject" mode occurs. Particles that were remaining in the injection loop are rinsed out in this step.

Steel A contained one particle fraction. The particle fraction was clearly separated from the void peak. The retention time for the particles was between 10 and 50 min, whereby the signal could be clearly separated into a peak (10 to 25 min) and a decreasing shoulder (25 to 50 min). The particles extracted from steel B had retention times between 8 and 50 min. The particles consisted of two fractions: one fraction with retention times from 8 to 13 min and one fraction with retention times ranging from approx. 13 to 25 min. The second particle fraction was followed by a slowly decreasing shoulder ending in a small release peak. The Nb and Ti carbonitrides extracted from steel C also had retention times between 8 and 50 min, similar to steel A and B. As with steel B, the particles extracted from steel C consisted of two particle fractions: a particle fraction with short retention times between 8 and 15 min and a particle fraction with longer retention times from 15 to 50 min with a maximum at 26 min.

The measured retention time distributions were transformed into particle size distributions using the calibration function determined with the different-sized gold reference particles coated with Disperbyk-2012. Retention times were transformed using equation B.2 and and the frequency signal $g(t)$ was transformed into $g(x)$ using equation B.3. The transformation reveals the hydrodynamic diameter of the extracted particles. The determination of the particle core diameter required to subtract the thickness of the ligand shell (11.48 nm) from the hydrodynamic diameter. Figure B.7 illustrates the extinction-weighted size distribution for steel A, B, and C. The signal in the very beginning of each distribution comes from the void peak and shall not be considered.

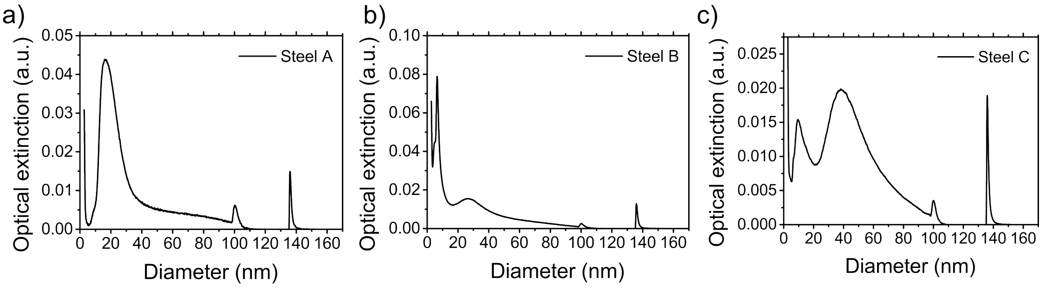

Figure B.7: Particle size distribution of the particles extracted from a) steel A; b) steel B; c) steel C measured with field-flow fractionation.

Steel A had a monomodal distribution with a peak maximum at 15 nm and a shoulder going up to particles with diameters of 100 nm. Steel B had a bimodal distribution with very small particles with sizes of only a few nanometer and a second particle fraction with diameters of approx. 20 to 40 nm followed by a slowly decreasing shoulder up to 100 nm. The particles extracted from steel C had a similar size distribution to steel B. The small particle fraction had diameters from 5 to 20 nm and the large particle fraction had diameters from 20 to 100 nm with a peak maximum at 40 nm.

The particle concentration during FFF analysis is lower than in AUC analysis. As a result, the small particle fractions of steel B and C could only be detected at very short wavelengths. At large wavelengths only Ti-containing particles were visible. Since our FFF device allows only the analysis of one specific wavelength at a time, I chose the wavelength of 280 nm due to the limited detectability of the small NbC particles, well aware that at this wavelength the ligand has a significant influence on extinction.

B.5 Mie theory

Comparison of the data obtained by AUC and FFF to TEM requires a transformation of the extinction-weighted data to number-weighted data. To obtain number-weighted data, the extinction-weighted data has to be transformed into mass-weighted data using Mie theory, which is further transformed into number-weighted data.

For Mie theory, information on the complex refractive index, particle shape, and morphology are required. However, the extracted particles have different compositions, shapes, and morphologies. Thus, for steel A that contained only Ti as microalloy element, the complex refractive indeces of

TiN, TiC, and the mean of the pure phases for TiCN were used. For steel B and steel C, the complex refractive indeces of TiN, NbC, and NbTiCN as the average refractive index of NbC and TiN were used. The particle shape was assumed to be spherical and the morphology was assumed to be homogeneous. No data on the refractive index of the ligand shell was available. Therefore, the ligand shell was not considered in the calculations. Figure B.8 shows the calculated mass-weighted size distribution of the AUC analysis.

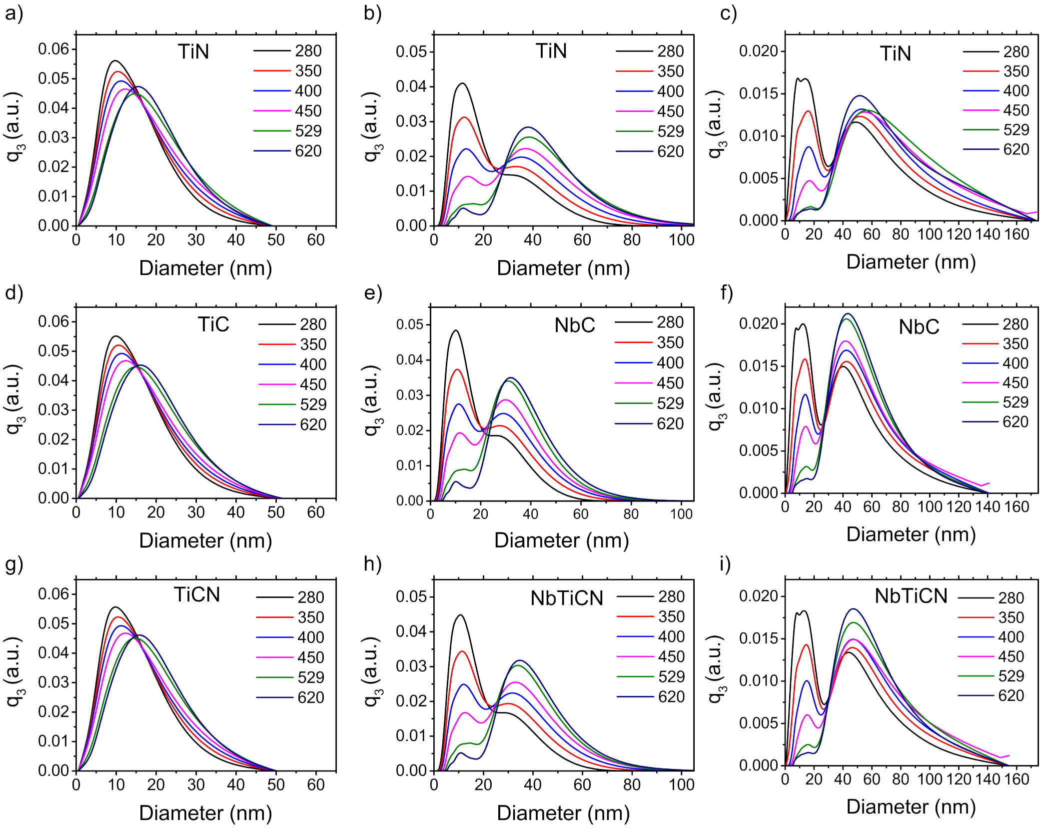

Figure B.8: Wavelength dependent mass-weighted size distributions measured with AUC for the particles extracted from steel. For Mie correction, different refractive indeces were used. For steel A, the refractive indices of a) TiN, d) TiC, and g) TiCN were used. For steel B, the refractive indices of b) TiN, e) NbC, and h) NbTiCN were used. For steel C, the refractive indices of c) TiN, f) NbC, and i) NbTiCN were used.

Mie theory is supposed to correct the wavelength dependent differences in extinction and result in one distribution for all wavelengths. However, as can be seen in Figure B.8, the PSDs measured at different wavelengths differ significantly regardless of the refractive index used.

The failure of the Mie correction could have several reasons. One factor is certainly not taking into account the dispersing agent. The absorption spectrum of the surfactant shows that light is strongly absorbed in the UV range. At wavelengths $< 260\,\mathrm{nm}$ the extinction is very high and decreases for higher wavelengths. At 280 nm the extinction is already only half of the extinction at 260 nm and at 350 to 400 nm extinction vanished. Since the ligand accounts for a large proportion of the volume, especially with small particles, the observed extinction of the small particles at short wavelengths is much higher than at longer wavelengths and their concentration is estimated to be too high. The Mie correction at these short wavelengths is therefore distorted.

Furthermore, the composition of the particles varies over a large range, especially for the particles extracted from steel B and C, and they have complex morphologies. Because of the mutual solubility of the different microalloy carbides and nitrides and the large differences of the refractive indices of the pure phases, a correction that only leads to small deviations is not possible with the implemented Mie correction.

Not only the composition varies and impedes a successful Mie correction, but also the morphology of the particles varies significantly. Particles may occur as homogeneous single phase particles, but also heterogeneous dual phase particles might be present. These kind of precipitates are likely to occur in steels with an alloy design containing two or more microalloy elements, such as steel B and C. Due to the low solubility of TiN, these precipitates form already at high temperatures and can act as nucleation sites for NbCN precipitation, which growths on the TiN seeds forming complex dual phase particles. Depending on the amount precipiated on the seed particle, the TiN seed may be only partially covered by NbCN (NbCN caps on TiN-particle) or completely covered (core-shell structure).

Considering all these points, it is obvious that the simple Mie correction fails with the extracted particles, as it is only designed for simple spherical particles with a homogeneous composition and well-defined optical properties. The discussion about the failure of Mie theory showed, however, how much information is contained in the measured extinction signal. More sophisticated algorithms are required that take into account the Mie theory for particles with non-spherical shapes and complex compositions. However, these would go beyond the scope of this work.

Due to the incorrect Mie correction caused by the lack on information on complex refractive indices and particle shapes, a quantitative comparison of the particle size distributions found with AUC, FFF, and TEM is currently not possible. However, Mie correction mainly corrects the relative ratios of different particle fractions, but is not absolutely necessary to determine the size of the individual particle fractions (the size is only slightly affected). Especially in monomodal particle systems with relatively small distribution widths (as in steel A), the extinction-weighted size distribution is assumed to be still in good approximation to the mass-weighted distribution. In the case of bimodal distribution or very broad PSD, the relative frequencies of the individual particle fractions in the colloidal size determination methods and TEM are significantly different due to the different weighting. A quantitative comparison is therefore not possible, but at least a qualitative comparison of the measured sizes of the particle fractions is supposed to be possible.

B.6 Carbon extraction replica - extracted particles

In order to investigate possible effects of the etchant on the particles during extraction (e.g. size reduction caused by particle etching), the size distribution of extracted particles and particles from a carbon extraction replica from the same steel were both determined with automatic image analysis[1] [145] and compared to each other. Figure B.9 illustrates the size distributions for the extracted particles (blue) and the carbon extraction replica (green).

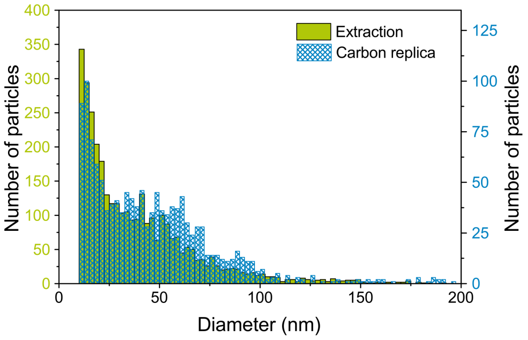

Figure B.9: Size distribution measured with automatic image analysis in STEM: extracted particles (blue) and carbon extraction replicas (green). Note the different scalings of the y-axes.

Figure B.9 shows very good agreement between the PSDs. It is important to be aware of the different scales of the y-axes. With identical measurement conditions, a total number of 3337 particles for the extracted particles were

---

[1] Particle analysis and carbon extraction replica production was done at the AG der Dillinger Hüttenwerke.

analyzed and only 1321 particles on the carbon extraction replica. This indicates the advantage of the increased particle area concentration of the extraction method compared to the carbon extraction replicas.